Magnetic Reconnection and Heavy Ions

Håkon Midthun Kolstø

Thesis for the degree of Philosophiae Doctor (PhD)
University of Bergen, Norway
2022

UNIVERSITY OF BERGEN

Magnetic Reconnection and Heavy Ions

Håkon Midthun Kolstø

Thesis for the degree of Philosophiae Doctor (PhD)
at the University of Bergen

Date of defense: 28.09.2022

Year: 2022
Title: Magnetic Reconnection and Heavy Ions

Name: Håkon Midthun Kolstø
Print: Skipnes Kommunikasjon / University of Bergen

Abstract

The vast majority of matter in the observable Universe exists in the form of plasma. The plasma is characterized by a collection of charged particles that exhibits certain electrodynamic properties in which the typical potential energy of a particle due to the Coulomb attraction of its nearest neighbor is much less than its random kinetic energy. A typical plasma is thus practically free from the direct influence of other charged particles which, in turn, enables the synergetic and complex interaction between the plasma and the electric and magnetic fields. A large part of plasma processes relies either on the exchange from stored electromagnetic energy in the fields to mechanical energy of the plasma particles or vice versa. One of the most important energy conversion processes occurring in plasma is that of *magnetic reconnection*. In the case of the Earth's magnetosphere, magnetic reconnection is the primary mechanism responsible for the transport of energy, mass, momentum, and magnetic flux into the Earth's magnetic cavity. Furthermore, magnetic reconnection is responsible for magnetic storms and high geomagnetic activity and may eventually lead to the optical aurora. The strength of this explosive energy release depends on a variety of conditions. One mechanism which can reduce the efficiency is the presence of heavy ions. We know from observations that heavy ions, such as ionized oxygen, are transported from our ionosphere, out along the magnetic field, to the magnetopause and the magnetotail where they can get captured by the reconnection process. While the most common plasma species in these regions are protons and electrons, heavier ion species, such as oxygen, can sometimes dominate during storm time conditions. Understanding how heavy ions alter the dynamics and efficiency of the reconnection process is therefore crucial for obtaining a complete picture of the workings of magnetic reconnection. This is the main objective of this thesis.

In the pursuit of this, two approaches are utilized: 1) Numerical 2.5D particle-in-cell (PIC) simulations, and 2) Spacecraft observations made by NASA's Magnetospheric Multiscale (MMS) mission. In this thesis, it is found that heavier ions introduce distinctive kinetic behavior and different spatial and temporal scales for the reconnection system. Due to its high inertia, O^+ will respond to any field variations at a rate that is 16 times slower than the protons and 30000 times slower than the electrons[1]. This fast response time for the lighter plasma species results in stronger field connectivity such that any motion of the plasma particles also will alter the motion of the magnetic field - and vice versa. Species subject to such conditions exhibit a magnetized behavior. Therefore, due to their higher mass, the oxygen ions are to a much larger degree subject to demagnetization. In this case, the O^+ dynamics are predominantly dictated by the electric field. Under certain conditions, this may eventuate as quasi-steady O^+

---

[1] This corresponds to the following mass ratio: $m_{O^+} : m_p : m_e \sim 1 : 16 : 30000$

density structures persisting over several ion inertial lengths and are referred to as *oxygen waves*. These structures have furthermore been observationally confirmed as a part of this thesis using data from the MMS mission.

Magnetized species may efficiently impart their momenta to the reconnection site due to their evident coupling to the magnetic field. Even though the O^+, under certain conditions, exhibit a demagnetized behavior, it is found that they are still able to alter the dynamics of the reconnection site. Here, the coupling of O^+ to the magnetic flux occurs instead indirectly through the electrons by an electrostatic coupling. Furthermore, it is shown in the thesis that the demagnetized oxygen ions may reduce the reconnection rate, but not to the extent predicted by conventional mass-loading effects. By utilizing 2.5D particle-in-cell (PIC) simulations, we show that the reconnection process proceeds nearly twice as fast as predicted by Alfvén scaling. A new scaling relation has been developed in this thesis showing that the reconnection rate is not dependent on the configuration of O^+. The rate reduction mechanism is realized by the fact that the oxygen ions extract energy from the fields that would otherwise have gone to the acceleration of the electrons and protons. The findings presented in this thesis have enhanced our understanding of the workings of magnetic reconnection in the near-Earth space environment and have contributed to a greater understanding of plasma physics in general.

Abstrakt

Majoriteten av materien i det observerbare universet eksisterer i form av en plasma. Plasmaet er karakteriseres av en samling ladede partikler som oppfyller visse elektrodynamiske egenskaper hvor den typiske potensielle energien til en partikkel på grunn av Coulomb-attraksjonen til dens nærmeste nabo er mindre enn dens tilfeldige kinetiske energi. Et typisk plasma er dermed praktisk talt fritt for direkte påvirkning av andre ladede partikler som igjen muliggjør den synergetiske og komplekse interaksjonen mellom plasmaet og de elektriske og magnetiske feltene. Nesten alle plasmaprosesser er avhengig av enten konvertering fra lagret elektromagnetisk energi i feltene til mekanisk energi av plasmapartiklene eller omvendt. En av de viktigste energiomdannelsesprosessene som skjer i en plasma er *magnetisk omkobling*. Når det gjelder jordens magnetosfære, er magnetisk omkobling den primære mekanismen som muliggjør transport av energi, masse, momentum og magnetisk fluks inn til jordens magnetiske miljø. Videre er magnetisk omkobling ansvarlig for magnetiske stormer og høy geomagnetisk aktivitet og kan til slutt føre til optisk nord- og sørlys. Styrken til denne eksplosive energifrigjøringen avhenger av en rekke forhold. En mekanisme som kan redusere effektiviteten er tilstedeværelsen av tunge ioner. Vi vet fra observasjoner at tunge ioner, som ionisert oksygen, transporteres fra ionosfæren vår, ut langs magnetfeltet, til magnetopausen og magnetohalen hvor de kan fanges opp av omkoblingssprosessen. Mens de vanligste plasmakomponentene i disse regionene er protoner og elektroner, kan tyngre ionearter, som oksygen, noen ganger dominere under stormtidsforhold. Å forstå hvordan tunge ioner endrer dynamikken og effektiviteten til omkoblingssprosessen er derfor avgjørende for å få et fullstendig bilde av hvordan magnetisk omkobling fungerer. Dette er hovedmålet i denne avhandlingen.

I jakten på dette benyttes to fremgangsmåter: 1) Numeriske 2.5D partikkel-i-celle (PIC) simuleringer, og 2) Romfartøyobservasjoner gjort av NASAs Magnetospheric Multiscale-oppdrag. I denne avhandlingen er det blitt funnet at tyngre ioner introduserer en distinkt kinetisk dynamikk og ekstra romlige og tidsmessige skalaer for omkoblingssprosessen. På grunn av sin inertielle treghet vil oksygenet reagere på feltvariasjoner med en rate som er 16 ganger langsommere enn protonene og 30000 ganger langsommere enn elektronene [2]. Denne raske responstiden for de lettere plasmapartiklene gir opphav til sterkere kobling til magnetfeltet, slik at enhver bevegelse av plasmapartiklene også vil endre bevegelsen til magnetfeltet - og omvendt. Plasmapartikler underlagt dette anses å ha en magnetisert atferd. Derfor, på grunn av sin høyere masse, er oksygenionene i mye større grad avmagnetisert under ellers samme omstendigheter. I dette tilfellet er O$^+$-dynamikken hovedsakelig diktert av det elektriske feltet. Under visse forhold kan det oppstå kvasi-stabile O$^+$ tetthetsstrukturer som vedvarer over flere

---

[2] Dette tilsvarer følgende masseforhold: $m_{O^+} : m_p : m_e \sim 1 : 16 : 30000$

ione-inertiallengder og blir referert til som *oksygenbølger*. Disse strukturene er blitt observasjonelt bekreftet som en del av denne avhandlingen.

Magnetiserte plasmapartikler kan effektivt overføre deres moment til omkoblingsregionen på grunn av deres tydelige kobling til magnetfeltet. Selv om O^+, under visse forhold, viser en avmagnetisert oppførsel, er det funnet at de fortsatt er i stand til å endre dynamikken til i omkoblingsregionen. For en avmagnetisert plasmapartikkel skjer koblingen av O^+ til den magnetiske fluksen i stedet indirekte gjennom elektronene ved en elektrostatisk kobling. Videre kan de avmagnetiserte oksygenionene redusere effektiviteten av magnetisk ombkobling, men ikke i den grad som er forutsagt av konvensjonelle massebelastningseffekter. Faktisk er effektiviteten av omkoblingssprosessen (omkoblingsraten) vist å være nesten dobbelt så høy som forutsagt av Alfvén-skalering. En ny skaleringsrelasjon er i denne avhandlingen blitt utviklet som viser at omkoblingsraten ikke er avhengig av konfigurasjonen til O^+, men heller dens totale mengde. Mekanismen som reduserer effektiviteten av magnetisk omkobling realiseres ved at oksygenionene trekker ut energi fra feltene som ellers ville ha gått til akselerasjonen av elektronene og protonene. Funnene presentert i denne oppgaven har forbedret vår forståelse av hvordan magnetisk omkobling fungerer i vår magnetosfære og har bidratt til en økt forståelse av plasmafysikk generelt.

Acknowledgements

This thesis concludes the work done over the course of 4 years as a PhD student. I am truly grateful to have had Cecilia Norgren and Michael Hesse as my supervisors. Cecilia, thank you for always being available to tackle whatever question I had, big or small. Your guidance and encouragement have made these last 4 years very enjoyable to me.

Michael, thank you for all you have taught me throughout the years, about science and more. Further thanks for all the great opportunities you have provided and for making my PhD studies a wonderful experience from day one.

I could not have hoped for a set of better supervisors.

Cecilia, Michael, and Paul thank you for creating and leading such a warm, inspiring and fun group to work in. It has been just great! I would further like to thank the rest of the SPPG family. Thanks to Paul, for all insights, fun times, and for not (yet) succeeding in convincing me to join you on your ultra runs. Susanne, thank you for all the fun conversations and the hundred cups of the world's finest coffee! Thank you Norah, Therese, and Judit for all the great contributions and fun discussions over the years.

Further thanks go to the MMS team and LASP group for making such amazing data accessible. Thanks to Li-Jen Chen at NASA Goddard Space Flight Center for sharing your experience and knowledge and introducing me to the beauty of observations.

Another thanks go out to the physics guys, who I am grateful to have shared many of these amazing 9 years at IFT with. Further thanks to all my great friends in Norway, the US, and around the globe who I am so lucky to have in my life.

Special thanks to my parents for always supporting and encouraging me, regardless of what I were to aspire to.

To Steinar and Synnøve, thank you for inspiring me to pursue this.

Håkon Midthun Kolstø
California, May 2022

Outline

This thesis including three published papers are submitted for the degree of philosophiae doctor (PhD) in physics at the Department of Physics and Technology, University of Bergen.

The thesis is divided into an introductory part and a part consisting of three papers published in international peer reviewed journals.

Paper I	H.M. Kolstø, M. Hesse, C. Norgren, P. Tenfjord, S.F. Spinnangr, N. Kwagala, *Collisionless Magnetic Reconnection in an Asymmetric Oxygen Density Configuration*, Geophysical Research Letters, Vol. 47, Issue 1 doi:10.1029/2019GL085359, 2020
Paper II	H.M. Kolstø, M. Hesse, C. Norgren, P. Tenfjord, S.F. Spinnangr, N. Kwagala, *On the Impact of a Streaming Oxygen Population on Collisionless Magnetic Reconnection*, Geophysical Research Letters, Vol. 47, Issue 22 doi:10.1029/2020GL089462, 2020
Paper III	H.M. Kolstø, C. Norgren, M. Hesse, L.J. Chen P. Tenfjord, S.F. Spinnangr, N. Kwagala, *Magnetospheric Multiscale Observations of an Expanding Oxygen Wave in Magnetic Reconnection*, Geophysical Research Letters, Vol. 48, Issue 19 doi:10.1029/2021GL095065, 2021

During my PhD studies, I have also contributed to the following papers.

A P. Tenfjord, M. Hesse, C. Norgren, S.F. Spinnangr, H.M. Kolstø, *The Impact of Oxygen on the Reconnection Rate*, Geophysical Research Letters, Vol. 46, Issue 12
doi:10.1029/2019GL082175, 2019

B N. Kwagala, M. Hesse, T. Moretto, P. Tenfjord, C. Norgren, G. Toth, T. Gombosi, H. M. Kolstø, *Validating the Space Weather Modeling Framework (SWMF) for applications in northern Europe - Ground magnetic perturbation validation,* Journal of Space Weather Space Climate, Vol. 10
doi:10.1051/swsc/2020034, 2020

C P. Tenfjord, M. Hesse, C. Norgren, S.F. Spinnangr, H.M. Kolstø, N. Kwagala, *Interaction of Cold Streaming Protons with the Reconnection Process*, Journal of Geophysical Research, Vol. 125, Issue 6
doi:10.1029/2019JA027619, 2020

D C. Norgren, P. Tenfjord, M. Hesse, S. T. Redondo, W.Y. Li, N. Kwagala, S.F. Spinnangr, H.M. Kolstø,T. Moretto, *On the Presence and Thermalization of Cold Ions in the Exhaust of Antiparallel Symmetric Reconnection*, Frontiers in Astronomy in Space Sciences
doi:10.3389/fspas.2021.730061, 2021

E M. Hesse, C. Norgren, P. Tenfjord, J.L. Burch, Y.H. Liu, L.J. Chen, S. Wang, H.M. Kolstø, S.F. Spinnangr, R. Ergun, T. Moretto, N. Kwagala, *A New Look at the Electron Diffusion Region in Asymmetric Magnetic Reconnection*, Journal of Geophysical Research, Vol. 126, Issue 2
doi:10.1029/2020GL090690, 2020

F S.F. Spinnangr, M. Hesse, P. Tenfjord, C. Norgren, H.M. Kolstø, N. Kwagala, T. Moretto, *The Micro-Macro Coupling of Mass-Loading in Symmetric Magnetic Reconnection With Cold Ions*, Geophysical Research Letters, Vol. 48, Issue 13
doi:10.1029/2020JA028456, 2020

G S.F. Spinnangr, M. Hesse, P. Tenfjord, C. Norgren, H.M. Kolstø, N. Kwagala, T. Moretto, J.P. Jimémenez, *Asymmetrically Varying Guide Field During Magnetic Reconnection: Particle-In-Cell Simulations*, Journal of Geophysical Research, Vol. 127, Issue 1
doi:10.1029/2021JA029955, 2021

H J.P. Jimémenez, P. Tenfjord, M. Hesse, C. Norgren, N. Kwagala, H.M. Kolstø, S.F. Spinnangr, *The Role of Resistivity on the Effi-*

ciency of Magnetic Reconnection in MHD, Journal of Geophysical Research, Vol. 127, Issue 6
doi:10.1029/2021JA030134, 2021

Contents

Acknowledgements **v**

Outline **vii**

1 Introduction **1**
- 1.1 Objectives 2
- 1.2 Outline 3

2 Plasma **5**
- 2.1 Defining a Plasma 5
- 2.2 The behavior of single particles 8
- 2.3 Kinetic Theory 8
- 2.4 Fluid description and Magnetohydrodynamics 11
- 2.5 Diffusion and Frozen Flux 14
- 2.6 The Concept of Magnetic Field Lines 15

3 Magnetic Reconnection **17**
- 3.1 Theoretical efforts to tackle Reconnection 21
  - 3.1.1 Magnetohydrodynamic models 21
  - 3.1.2 Fluid models of Magnetic Reconnection 23
  - 3.1.3 General Magnetic Reconnection 28
- 3.2 The Role of Ionospheric Ions in Magnetic Reconnection 29
  - 3.2.1 Origin of Ionospheric Ions 29
  - 3.2.2 Observations of Heavy Ions in the Magnetosphere 30
  - 3.2.3 The Impact of Heavy ions on the Reconnection Process 35
  - 3.2.4 Dayside O^+ Reconnection Study 40

4 Probing Reconnection **47**
- 4.1 Nature as a laboratory; MMS 48
  - 4.1.1 Instruments Overview 50
- 4.2 Particle-In-Cell and Plasma Simulations 52
  - 4.2.1 Simulating Interacting Particles 52
  - 4.2.2 Particle-In-Cell Approach 54

5 Introduction to Papers **65**

6 Conclusions and Future Prospect **69**
6.1 Conclusions 69
6.2 Future Prospects 70

Bibliography **72**

7 Scientific results **89**

Paper I: Collisionless Magnetic Reconnection in an Asymmetric Oxygen Density Configuration **91**

Paper II: On the Impact of a Streaming Oxygen Population on Collisionless Magnetic Reconnection **103**

Paper III: Magnetospheric Multiscale Observations of an Expanding Oxygen Wave in Magnetic Reconnection **113**

List of Abbreviations **125**

Appendix A **127**

Chapter 1

Introduction

Magnetic reconnection is a fundamental physical process that, enables the release and alteration of stored magnetic energy and facilitates the transport and acceleration of charged particles (e.g. *Antiochos et al.* (1998); *Cassak et al.* (2007); *Drake et al.* (2010); *Gonzalez and Parker* (2016); *Goodman and Uzdensky* (2008); *Paschmann et al.* (1979)). It is widely regarded to be one of the most important energy conversion processes in plasmas. Magnetic reconnection can be found to occur in space (e.g. *Oieroset et al.* (2001); *Paschmann et al.* (1979)), laboratory (e.g. *Yamada* (1999)), and astrophysical plasmas (e.g. *de Gouveia Dal Pino et al.* (2010)), powering such diverse phenomena as solar eruptions, breaking magnetic confinement in tokamaks, and relativistic jets from rapidly rotating pulsars.

Furthermore, magnetic reconnection is the engine ultimately behind the deleterious space environment effects commonly referred to as *space weather*. Every day, the Sun ejects a vast amount of charged particles accompanied by interplanetary magnetic fields which constitutes solar wind. Some of these fields and particles might just decide to visit us, doing so by traveling at speeds close to 1.8 million kilometers per hour. Luckily, mother Earth has a trick up her sleeve. A strong magnetic field generated by Earth's internal dynamo acts as a shield and protects us against these potentially hazardous particles. If not, life on Earth, or the absence of it, might be very reminiscent of Mars.

If the conditions are just right, the process of magnetic reconnection may occur in the Earth's magnetosphere, thus enabling the coupling between the solar wind and magnetosphere. The energy released in the Earth's space environment due to reconnection is estimated to reach up to 10^{16} J[1] (*Weiss et al.*, 1992) which consequently leads to the generation of a variety of magnetospheric phenomena such as geomagnetic substorms, energetic particle precipitation, and auroras. The reconnection process may subsequently give rise to strong magnetic field perturbations resulting in induced surface currents which might pose great risks to electrical infrastructure and artificial satellites. In order to achieve a complete understanding of how energy is released by the sun and in the magnetosphere, and how it impacts life on Earth, in orbit, and beyond, we need to understand the process of magnetic reconnection, as it is in its essence the fundamental piece to complete the puzzle.

The evolution of magnetic reconnection is highly dependent on the magnetic field configuration, magnitude, plasma composition and its distribution. The widely reported

---

[1] For context, this corresponds to roughly 3 TWh.

presence of ionospheric ions in the magnetosphere has led to the investigation of the role and effect these plasma species have on the reconnection process. With an estimated outflow rate of 10^{26} ions/s[2], including both H^+ and O^+, ionospheric ions may be quite abundant in the reconnection process in the magnetosphere (*Yau et al.*, 1985). Ionospheric ions are thermally less energetic than their magnetospheric counterpart and will thus give rise to distinct spatial scales for the reconnection process (*Divin et al.*, 2016; *Lotko*, 2007; *Maggiolo and Kistler*, 2014; *Shay and Swisdak*, 2004; *Toledo-Redondo et al.*, 2015). Heavy ionospheric ions such as e.g. O^+, will due to their significantly higher mass, give rise to longer temporal scales which introduce additional kinetic behavior to the reconnection process. This, in turn, alters the dynamics of magnetic reconnection causing a decrease in the rate at which magnetic energy is released. The effect of heavy ions on the reconnection rate has great implications for the large-scale evolution of the dynamics of geomagnetic storms and substorms. Therefore, by understanding how heavy ions couple, and alter the dynamics and rate of the reconnection process, we are one step closer to solving the puzzle of magnetic reconnection.

1.1 Objectives

The scope of this thesis is to enhance our understanding of the role of heavy ions in magnetic reconnection. By tailoring state-of-art numerical particle-in-cell (PIC) simulations of magnetic reconnection events, subject to the presence of heavy ions, we are able to gain deep insight into how the process of reconnection is altered by these heavier species. In addition to PIC simulations, data from NASA's Magnetospheric Multiscale (MMS) mission is utilized to search for oxygen-rich magnetotail reconnection events. This enables the study of the kinetic behavior of O^+ in magnetic reconnection out in nature, specifically the magnetotail. PIC simulations are further used to contextualize the MMS observations.

In Paper I, a magnetotail reconnection event is tailored to mimic a configuration realized by the case of asymmetric ionosphere outflow of oxygen ions. Such, generally expected outflow scenarios give rise to north-south O^+ density asymmetries which show a great impact on the reconnection process with the generation of significant asymmetries of the Hall electric field and the diffusion region. Furthermore, it is shown that the reduction of the reconnection rate does not follow traditional Alfvén scaling.

Paper II investigates the effect of tailward streaming oxygen on the reconnection process. Ionospheric oxygen ions that escape the ionosphere propagate tailwards and may reach energies up to 5 eV ($\sim$250 km/s) (*Liao et al.*, 2015). As compared to protons, the oxygen ions have a smaller gyrofrequency such that their coupling to the magnetic flux is less evident. Even though the cold, inert O^+ are subject to demagnetization as their gyroperiod greatly exceeds the evolutionary time scale of the reconnection process (Ω_p^{-1}), they are still able to impart their momentum onto the reconnection region. Instead of imposing their momenta through flux coupling, it is made possible indirectly through the means of an electrostatic coupling between the electrons and oxygen ions.

Paper III utilized NASA's MMS spacecraft constellation to investigate the dynamics of O^+ in magnetotail reconnection. On the 4th of August 2017, MMS crossed the re-

---

[2] Varying with at least one order of magnitude due to solar EUV and geophysical activity.

connection exhaust in the presence of oxygen ions with number density ratios reaching $n_{O^+}/n_p \approx 0.1$, with respect to the protons. The data captured by MMS uncovered kinetic O^+ signatures consistent with phenomena seen in PIC simulations. The analysis further reveals the first observation of an expanding oxygen wave predicted by *Tenfjord et al.* (2018).

1.2 Outline

The thesis is structured as follows. Chapter 2 gives a basic introduction to the fundamental concepts of plasma to lay the foundation needed to discuss magnetic reconnection. Here we review fundamentals such as plasma criteria, kinetic theory, fluid models and magnetohydrodynamics, and diffusion and the frozen-in theorem. Chapter 3 provides an introduction to magnetic reconnection. The topic of discussion in this chapter is the theoretical advancements, observational studies of magnetic reconnection, as well as the role of ionospheric ions in the reconnection process. In Chapter 4, the means of studying the phenomena of reconnection is discussed. First, the use of nature as a laboratory is introduced, in which the MMS spacecraft are introduced. A quick overview of the instruments used in this thesis is provided. Furthermore, the numerical approach which is used to investigate reconnection is also discussed. Chapter 5 contains a brief summary of Paper I, Paper II, and Paper III. Finally, Chapter 6 provides a conclusion to the thesis and a discussion of the future prospects.

Chapter 2

Plasma

Let us initiate an experiment. Take a piece of ice from the freezer and place it on the frying pan. Even as a child it would seem like we have an a priori understanding of this experiment: it melts, and subsequently, it vaporizes. But what would happen if you managed to contain the vapor and just kept on heating it? By proceeding with this experiment, the H_2O molecules would start to jiggle so rapidly that, eventually, the electric forces binding the constituents can no longer confine them. Now, the electrons and ions (e.g. H^+, O^+, H_2O^+, OH^+) move freely and unconfined within this system. You have now created the fourth state of matter; namely *plasma*. Despite how strenuous this might sound, plasmas are extremely common. In fact, the state of matter of the paper or computer from which you are reading these words is, on the cosmic scale, actually quite rare. The state of matter of you, Earth, and essentially everything around us (with the exception of some TVs, neon signs, and thunderstorms) are so rare that less than 0.1% of matter in the universe is in this state. So where is it? The shining bright stars are gravitationally confined spheres of hot plasma. The space between our planets, stars, and galaxies is not a vacuum - but cold tenuous plasma. Plasmas exist in various forms, with varying density, temperature, and composition. In the next section, we will give a more rigorous definition of what makes up a plasma. In this chapter, we provide an overview of important tools and concepts to probe an understanding of plasma. These concepts and derivations can readily be found in virtually any introductory plasma physics book (e.g. *Baumjohann and Treumann*, 1996; *Choudhuri*, 1998; *Goldston and Rutherford*, 1995; *Parks*, 1991).

2.1 Defining a Plasma

In the previous section, we briefly mentioned that a plasma is a gas of charged particles in which the electrons and ions have been separated and are free to move around in the system - e.g. the star or the space just outside our Earth; the plasmasphere. In the plasma, the positive and negatively charged particles are in roughly equal abundance indicating that on a larger scale, the plasma behaves *quasineutrally* in the stationary state. This means that the plasma, on average, looks electrically neutral even though it is comprised of charges which are free to induce strong electric fields on a local scale. As charged particles of opposite signs are subject to attraction by virtue of Coulomb's law, any local perturbations in the plasma will generate charge imbalances till the spatial potential extent of the charge is shielded away. This is primarily done by the more mobile electrons. Within this region, the microscopic fields of each individual charge carrier must cancel out in order to provide macroscopic charge neutrality (*Baumjohann and Treumann*, 1996). The resulting potential due to the perturbation of a point-like particle of charge q is given by the Debye potential

$$\phi_D = \frac{q}{4\pi\varepsilon_0 r} e^{-r/\lambda_D}, \quad \lambda_D = \left(\frac{\varepsilon_0 k_B T_e}{ne^2}\right)^{\frac{1}{2}} \tag{2.1}$$

where k_B is the Boltzmann constant, T_e is the electron temperature, and n is the mean plasma density outside the sphere of length λ_D, known as the Debye sphere. The influence of the charge quickly decays with distance, and at $r = \lambda_D$, the electrostatic potential has decreased to $1/e$ of its maximum value. It is thus evident that in order for a plasma to behave in a quasi-neutral manner the characteristic length scale L of the plasma must be much larger than the Debye length, i.e.

$$\lambda_D \ll L \tag{2.2}$$

This is known as the first plasma criterion. If Equation (2.2) is not fulfilled there would not be enough space for the collective shielding to occur.

As the charge shielding results from the collective behavior within a Debye sphere, it is paramount that this sphere contains enough particles. The number of particles within a Debye sphere scales with $n_e\lambda_D^3$. This leads us to define the plasma parameter Λ and the second plasma criterion

$$\Lambda = 4\pi n_e \lambda_D^3 \gg 1 \tag{2.3}$$

By raising (2.3) to 2/3 and inserting the Debye length we obtain the plasma coupling parameter Γ

$$\Gamma = \Lambda^{2/3} = \frac{4\pi\varepsilon_0 k_B T_e}{e^2 n^{1/3}} = \frac{E_{th}}{E_{pot}} \gg 1 \tag{2.4}$$

where $E_{th} = k_B T_e$, and $E_{pot} = e^2/4\pi\varepsilon_0 n^{-1/3}$ are the kinetic energy of the particles and the effective electrostatic potential between two charges, respectively. The plasma coupling parameter is a metric of how strongly coupled the plasma system is. For strongly coupled plasmas, i.e. low values of Γ, particle trajectories are highly affected by the interactions of neighboring particles as the potential energy dominates. Such a system is highly collisional and corresponds to having few particles within the Debye sphere. In weakly coupled systems, however, the thermal energy greatly exceeds the potential energy, and particle trajectories are thus not very prone to interactions induced by neighboring constituents. Such a system is regarded as collisionless and is equivalent to having a large number of particles within the system.

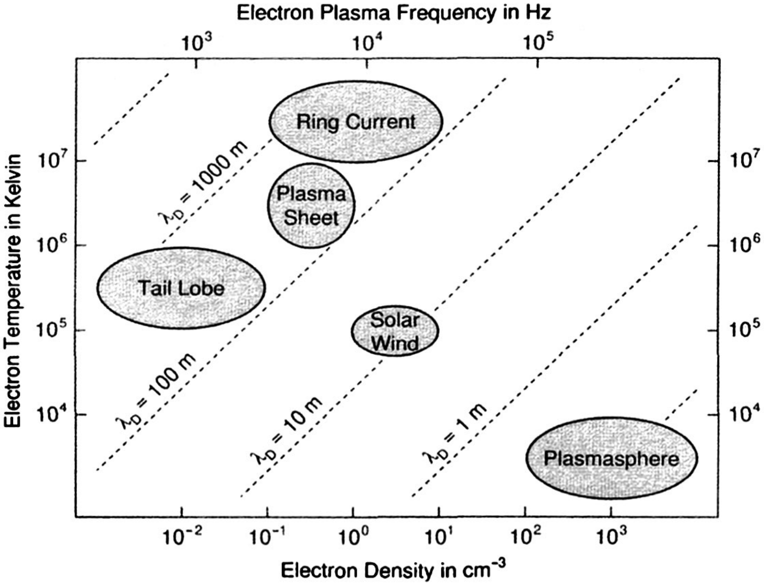

Figure 2.1: a) Typical parameters for different near-Earth plasmas. Adapted from (Baumjohann and Treumann, 1996).

Imagine the case of a fully ionized, quasi-neutral plasma experiencing a perturbation induced by an external force. As the electrons are vastly more mobile than the ions, they will accelerate in an attempt to restore charge neutrality. The electron's inertia will cause them to move back and forth around an equilibrium position, thus resulting in a fast collective oscillation around the much heavier ions. The oscillation frequency for a fully ionized plasma may be written as

$$\omega_{pe} = \left(\frac{n_e e^2}{m_e \varepsilon_0} \right)^{1/2}$$

and is known as the electron plasma frequency. Some plasmas, however, are not fully ionized. An example of a partially ionized plasma is the ionosphere. If the electrons in the ionosphere are subject to collisions with the abundant neutrals, an equilibrium will be established between the electrons and the neutrals causing the plasma to transition its behavior to that of neutral gas. In order for the electrons to remain unaffected by the collisions with the neutrals the average time τ_n between two electron-neutral collisions must be much larger than the electron plasma period, i.e.

$$\omega_{pe} \tau_n \gg 1$$

which further is known as the third plasma criterion. In Figure 2.1, we see typical values of different plasmas in the near-Earth space environment. Although the shown parameters display ranges over several orders of magnitudes, (e.g. $\Delta n_e \sim 10^5$, $\Delta T_e \sim 10^3$, and $\Delta \omega_{pe} \sim 10^2$) they all fulfill the three criteria to constitute a plasma.

2.2 The behavior of single particles

In the situation where the motion of the charged particles does not directly influence one another, nor cause too large changes to the external fields, the motion of each plasma particle may be regarded independently. A simple approach towards a description of the particle dynamics is through Newtonian mechanics where we evaluate the forces acting on the particle and the resultant acceleration gives the motion. A particle with mass m and charge q moving in an electromagnetic field $(\mathbf{E},\mathbf{B})$ with velocity $\mathbf{v}$ yields the following equation of motion

$$m\frac{d\mathbf{v}}{dt} = q\mathbf{E}' \tag{2.5}$$

where $\mathbf{E}' = \mathbf{E} + \mathbf{v} \times \mathbf{B}$ is the electric field experienced by the particle - i.e. the electric field in the inertial frame of the moving particle. The resultant motion of the particle takes various forms depending on the magnitude of the respective fields. In the simplest case of $\mathbf{E} = \mathbf{0}$, a particle with velocity $\mathbf{v}$ will gyrate in the plane perpendicular to $\mathbf{B}$ at a rate known as the particle's gyrofrequency which is given by $\Omega = qB/m$. In the case of $(\mathbf{E},\mathbf{B}) \neq 0$, a particle initially at rest will be accelerated to $\mathbf{v}$ (due to $\mathbf{E}$) before its velocity is diverted to complete its motion around $\mathbf{B}$ due to acceleration by $\mathbf{v} \times \mathbf{B}$. Although the single particle description provides an intuition, it is, however, not feasible to calculate the equation of motion for every particle in a system. A box[1] with side lengths 6 Re in a plasma with 1 particle per cm^{-3}, the number of equations of motion needed to be solved reaches the order of 10^{29}. Furthermore, the collective behavior of charged particles induces changes in the electromagnetic field according to Maxwell's equations, given by,

$$\begin{aligned} \nabla \cdot \mathbf{E} &= \rho/\varepsilon_0 & \nabla \times \mathbf{E} &= -\frac{\partial \mathbf{B}}{\partial t} \\ \nabla \cdot \mathbf{B} &= 0 & \nabla \times \mathbf{B} &= \mu_0 \mathbf{J} + \varepsilon_0 \mu_0 \frac{\partial \mathbf{E}}{\partial t} \end{aligned} \tag{2.6}$$

where ε_0 and μ_0 are the permittivity and permeability of free space, respectively[2]. Thus, to properly solve the plasma dynamics for this small system one would need to quantify the changes of the electromagnetic fields induced by every single particle, and then, incorporate those changes to make 10^{28} versions of Equation (2.5) - one for every particle. Then solve them all!

It becomes quite clear that this is not a very feasible approach to study even for a reasonably small system. We thus make use of a different description which will aid in uncovering the wonders of a plasma.

2.3 Kinetic Theory

As opposed to treating the plasma as a collection of single particles, we will now instead assume that the plasma is an interacting system consisting of an abundance of particles

---

[1] 6 Re is the typical side lengths in our simulation domain.

[2] The quantity ε_0 (μ_0) is related to the **E**-field (**B**-field) capability to store electromagnetic energy and mediate forces in a vacuum.

each having a time-dependent position $\mathbf{x}_i(t)$ and velocity $\mathbf{v}_i(t)$. By introducing the concept of a six-dimensional space with coordinate axes (**x**,**v**), called *phase space*, all the possible states for the plasma particles are represented as points in this phase space. Thus, as a particle propagates through the system in the plasma, its dynamics can be depicted as a trajectory in phase space, as shown in Figure 2.2.

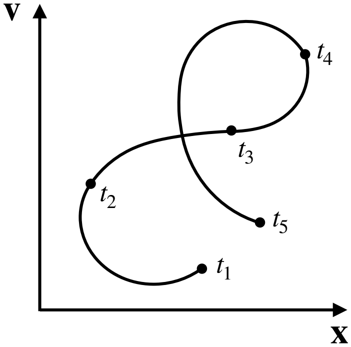

Figure 2.2: Illustration of a path of a particle in the six-dimensional phase space.

The exact microscopic phase space density enables us to write the position and velocity of every particle in the system in a simple manner

$$f_m(\mathbf{x},\mathbf{v},t) = \sum_{i=1}^{N} \delta(\mathbf{x}-\mathbf{x}_i(t))\delta(\mathbf{v}-\mathbf{v}_i(t)) \tag{2.7}$$

where $\delta(x-a)$ is the Dirac delta function which has the useful property that $\int_{-\infty}^{\infty} dx\delta(x-a)f(x) = f(a)$. From this, we see that the only non-zero contribution to $f_m(\mathbf{x},\mathbf{v},t)$ are those evaluated at the exact position **x** and velocity **v** of the particle's position $\mathbf{x}_i(t)$ and velocity $\mathbf{v}_i(t)$ - i.e, at the phase space coordinate ($\mathbf{x} = \mathbf{x}_i(t)$, $\mathbf{v} = \mathbf{v}_i(t)$). If no particle is lost or added to the plasma system, there should be no changes to the exact phase space density f_m. Applying the Lagrangian-derivative to $f_m(\mathbf{x},\mathbf{v},t)$ gives the following expression

$$\frac{d}{dt}f_m(\mathbf{x},\mathbf{v},t) = \frac{\partial f_m}{\partial t} + \mathbf{v}\cdot\nabla_{\mathbf{x}} f_m + \frac{q}{m}(\mathbf{E_m}(\mathbf{x}_i(t)) + \mathbf{v}\times\mathbf{B_m}(\mathbf{x}_i(t)))\cdot\nabla_{\mathbf{v}} f_m = 0 \tag{2.8}$$

which is known as the Klimontovich-Dupree equation (*Dupree*, 1964; *Klimontovich*, 1967). The $\mathbf{E_m}(\mathbf{x}_i(t))$ and $\mathbf{B_m}(\mathbf{x}_i(t))$ are the electromagnetic fields generated by all the particles in the plasma at the exact instantaneous particle position $\mathbf{x}_i(t)$. To solve this equation, we would still need to know the exact location in phase space of every single particle in the system - which was the exact same challenge we faced in section 2.2! Again, it is not of much use to know the trajectories of every single particle in the magnetosheath when trying to forecast the imminent effect of a solar wind zooming towards us. We, therefore, probe towards an average distribution function.

A way to perform this averaging scheme is to integrate the exact phase space density over a small box throughout the 6-dimensional phase space. The volume of one such box would be given as $\Delta V_{\mathbf{x}} = \Delta x\Delta y\Delta z$ and $\Delta V_{\mathbf{v}} = \Delta v_x\Delta v_y\Delta v_z$. So what would the typical size of this box be? We will now consider only one component the phase space, but the argument is the same for all components. It should be large compared to the mean spacing of particles, i.e $\Delta x \gg n^{-1/3}$, to assure we have enough particles in each box to provide a statistically well-defined mean. It should, however, be small enough such that the macroscopic quantities, e.g. density or temperature, do not vary significantly inside the box. An upper limit should be a volume in which the long-range electromagnetic effect from other charged particles in the plasma is screened off by particles of opposite charge. This upper limit is the Debye length λ_D. The average distribution function $\langle f_m \rangle$ will be defined as the number of particles in this small 6-dimensional phase-space box divided by the volume:

$$f(\mathbf{x},\mathbf{v},t) = \langle f_m(\mathbf{x},\mathbf{v},t) \rangle = \lim_{n^{-1/3} < \Delta V_i < \lambda_D} \frac{\int_{\Delta V_\mathbf{x}} \int_{\Delta V_\mathbf{v}} f_m(\mathbf{x},\mathbf{v},t)}{\int_{\Delta V_\mathbf{x}} \int_{\Delta V_\mathbf{v}}} \tag{2.9}$$

The deviation of the exact micro distribution $f_m(\mathbf{x},\mathbf{v},t)$ from the average distribution $f(\mathbf{x},\mathbf{v},t) = \langle f_m(\mathbf{x},\mathbf{v},t) \rangle$ must by, necessity, have zero average, i.e.

$$\begin{aligned} \delta f_m &= f_m - \langle f_m \rangle \\ \langle \delta f_m \rangle &= 0 \end{aligned} \tag{2.10}$$

The same holds for the fields, current densities, and charge densities.

$$\begin{aligned} \delta E_m &= E_m - \langle E_m \rangle \quad & \delta B_m &= B_m - \langle B_m \rangle \\ \delta \rho_m &= \rho_m - \langle \rho_m \rangle \quad & \delta J_m &= J_m - \langle J_m \rangle \end{aligned} \tag{2.11}$$

By substituting Equations (2.9) and (2.11) into the Klimontovich-Dupree Equation (2.8) we obtain the Boltzmann equation

$$\frac{\partial f}{\partial t} + \mathbf{v} \cdot \nabla_\mathbf{x} f + \frac{q}{m}(\mathbf{E} + \mathbf{v} \times \mathbf{B}) \cdot \nabla_\mathbf{v} f = \left(\frac{\partial f}{\partial t} \right)_c \tag{2.12}$$

which describes the evolution of the coarse-grained phase space density f under the influence of averaged electromagnetic fields. Figure 2.3 show an example of integrated velocity distribution functions for the oxygen species ($f_{O^+}(v_L, v_N) =$

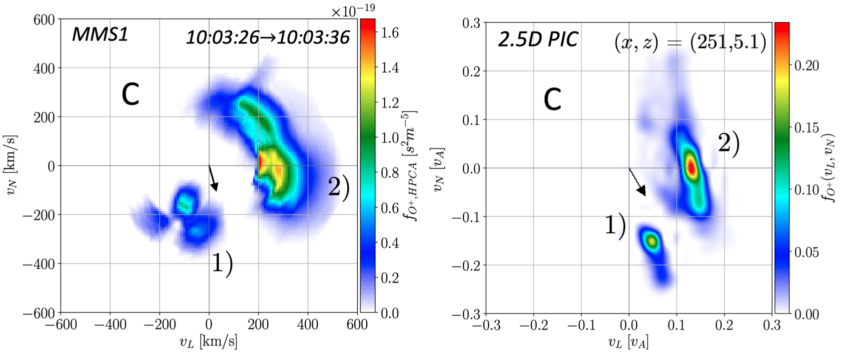

Figure 2.3: Integrated velocity distribution functions for O^+ from both spacecraft measurements (MMS) and numerical simulations (PIC). Adapted from Kolstø et al. (2021).

$\int f_{O^+}(v_L, v_M, v_M)dv_M)$ collected by spacecraft measurements (MMS) and numerical simulations (PIC). The distribution function f is interpreted as the probability of a particle to be found within a given phase space volume element $d\mathbf{x}d\mathbf{v}$, where $\left(\frac{\partial f}{\partial t}\right)_c$ is the particle-particle collision term. The vast majority of space plasma is collisionless[3] which sets $\left(\frac{\partial f}{\partial t}\right)_c = 0$ and hence we obtain the simplest possible form of a kinetic equation of a plasma, namely the *Vlasov* equation (*Vlasov*, 1945)

$$\frac{\partial f_s}{\partial t} + \mathbf{v}_s \cdot \nabla_{\mathbf{x}} f + \frac{q}{m}(\mathbf{E} + \mathbf{v} \times \mathbf{B}) \cdot \nabla_{\mathbf{v}} f = 0 \tag{2.13}$$

The Vlasov equation forms the basis of all kinetic theory in collisionless plasma - like those found in the solar wind, the magnetosphere, or the magnetotail. Together with Maxwell's equations with the charge and current densities are given as

$$\rho = \sum_s q_s \int f_s(\mathbf{x}, \mathbf{v}, t) d\mathbf{v} \tag{2.14}$$

$$\mathbf{J} = \sum_s q_s \int \mathbf{v}_s f_s(\mathbf{x}, \mathbf{v}, t) d\mathbf{v} \tag{2.15}$$

we have obtained a fundamental set of equations providing us with a detailed kinetic description of a mean (**E**, **B**)-field model, in which the particle-particle interactions are negligible compared to the particles interaction with the average electromagnetic field.

2.4 Fluid description and Magnetohydrodynamics

By measuring the distribution function f one does not directly obtain physical properties as density or velocity but rather probabilities of how many particles are to be found within a given velocity or energy interval. When you swim, you regard the water and not its building blocks. When you feel a breeze, you regard the wind and not the molecules. It is constructive to investigate the physical world by the use of physical quantities. However, the nature of f is closely related to the more familiar, less abstract, quantities referred to as *macroscopic quantities*. Physical quantities may be reconstructed from certain *velocity moments*[4] of the distribution function. The approach is rather straight forward. Instead of representing quantities as being a function of **x**, **v**, and t, the macroscopic quantities are now a function of **x** and t. By integrating moments of different orders of f we arrive at

$$n(\mathbf{x}, t) = \int_{-\infty}^{\infty} f(\mathbf{x}, \mathbf{v}, t) d\mathbf{v} \tag{2.16}$$

$$\mathbf{v_b}(\mathbf{x}, t) = \frac{1}{n} \int_{-\infty}^{\infty} \mathbf{v} f(\mathbf{x}, \mathbf{v}, t) d\mathbf{v} \tag{2.17}$$

$$\mathbf{P}(\mathbf{x}, t) = m \int_{-\infty}^{\infty} (\mathbf{v} - \mathbf{v_b})(\mathbf{v} - \mathbf{v_b}) f(\mathbf{x}, \mathbf{v}, t) d\mathbf{v} \tag{2.18}$$

---

[3] The ionosphere is an example of a collisional plasma in which $\left(\frac{\partial f}{\partial t}\right)_c \neq 0$

[4] i-th order velocity moments may be written as $M_i(\mathbf{x}, t) = \int \mathbf{v}^i f(\mathbf{x}, \mathbf{v}, t) d\mathbf{v}$.

where the 0^{th} and 1^{st} moments represent the number density and bulk flow velocity, respectively[5]. The pressure tensor $\mathbf{P}$ is defined as the contribution of the deviation from the velocities of the ensemble from the bulk velocity $\mathbf{v_b}$. In order to investigate the evolution of these macroscopic quantities, we calculate the moments of the Vlasov equation

$$\int_{-\infty}^{\infty} \mathbf{v}^i \left(\frac{\partial f}{\partial t} + \mathbf{v} \cdot \nabla_{\mathbf{x}} f\right) d\mathbf{v} = -\int_{-\infty}^{\infty} \mathbf{v}^i \left(\frac{q}{m}(\mathbf{E} + \mathbf{v} \times \mathbf{B}) \cdot \nabla_{\mathbf{v}} f\right) d\mathbf{v} \tag{2.19}$$

which for the 0^{th} order gives

$$\frac{\partial}{\partial t} n = -\nabla \cdot (n\mathbf{v_b}) \tag{2.20}$$

which we refer to as the *mass continuity equation* and describes the evolution of the plasma density for a given species. The continuity equation tells us that in the absence of any interacting processes on the plasma, which create or annihilate constituents, the total amount of particles or mass (and charge) in the system is conserved. By evaluating the first moment we obtain a second conservation equation known as the *momentum density conservation equation* which takes the form

$$\frac{\partial}{\partial t}(n\mathbf{v_b}) + \nabla \cdot (n\mathbf{v_b}\mathbf{v_b}) = -\frac{1}{m}\nabla \cdot \mathbf{P} + \frac{qn}{m}(\mathbf{E} + \mathbf{v_b} \times \mathbf{B}) \tag{2.21}$$

and describes the evolution of momenta for a particular species. More precisely it describes the fluid momenta and the electromagnetic forces acting on the fluid element. The equation shows clear similarities to the famous Navier-Stokes equation from classical hydrodynamics. In fact, the momentum density conservation equation, or just the *momentum equation*, is the Navier-Stokes equation with the inclusion of a term accounting for the Lorentz forces acting on the charges in the plasma.

With the equations presented thus far, we are closing in on a full description of the plasma system. But as it stands now the system may not be fully described. This macroscopic fluid description makes use of 5 independent quantities to fully describe the plasma system as a whole. These macroscopic quantities are the density n, bulk velocity $\mathbf{v_b}$, the pressure $\mathbf{P}$, and the electromagnetic fields $\mathbf{E}$ and $\mathbf{B}$. In order to arrive at a complete description of the plasma system, it is imperative to know how the quantities that build up the system evolve in time. So far, we have an evolutionary equation for four of them. The evolutionary equations for n and $\mathbf{v_b}$ were found by integrating moments of the Vlasov equation whereas for $\mathbf{E}$ and $\mathbf{B}$ we use the Maxwell's equations. However, we are missing an evolutionary equation for the pressure. We quickly see that integrating the Vlasov equation for a higher moment will not bring us any closer to a complete set as the part subjected to spatial differentiation will always have one rank higher than the temporal differentiation. Thus, in order to complete the set of equations needed, integrating moments of Vlasov's equation to order of infinity will not serve as a solution. Instead, we describe the pressure $\mathbf{P}$ as an approximation to the ideal gas law with the parallel and perpendicular pressures given by $p_{\perp,\parallel} = nk_B T_{\perp,\parallel}$ such that $\frac{d}{dt}\left(\frac{p}{n^\gamma}\right) = 0$, where γ is the adiabatic index. This now closes our system of equations.

---

[5] Do note that n, $\mathbf{v}_b$, and $\mathbf{P}$ have different vector ranks i.e. n is a scalar (rank 0) and $\mathbf{P}$ is a rank 2 tensor.

Magnetohydrodynamics

Equation (2.20) and (2.21) describes the mass and momentum conservation for a given species in the multi-fluid plasma system. If the time-scale variations of the fields and fluids evolve slower than the characteristic time-scale of the heaviest plasma species, the multi-fluid plasma description can be simplified into a single-fluid description. Thus, if the characteristic time-scale variations ω is smaller than the ion cyclotron frequency ω_{gi}, and the characteristic length scale L is larger than the ion gyroradius L_g we can approximate the multi-fluid system into a single-fluid system. At these low frequencies and large spatial scales, we arrive at *magnetohydrodynamics* (MHD), for which Alfén was awarded the Nobel Prize (*Alfvén*, 1942). By adding the momentum equations for ions and electrons we arrive at the MHD momentum equation which takes the following form

$$nm\frac{d}{dt}\mathbf{v_b} = \mathbf{J}\times\mathbf{B} - \nabla\cdot\mathbf{P} \tag{2.22}$$

where, for a simple plasma constituting of e.g. electrons and protons, $n_e = n_p = n$, $m = m_e + m_p$, and $\mathbf{v}_b = (m_e\mathbf{v}_b^e + m_p\mathbf{v}_b^p)/(m_e + m_p) \approx (m_e/m_p)\mathbf{v}_b^e + \mathbf{v}_b^p \approx \mathbf{v}_b^p$, and the current density $\mathbf{J}$ is given as $\mathbf{J} = ne(\mathbf{v}_b^p - \mathbf{v}_b^e)$. Furthermore, $\mathbf{P}$ is the total pressure given by $\mathbf{P} = \mathbf{P}_e + \mathbf{P}_p$. By instead subtracting the ion momentum equation from the electron momentum equation and introducing a friction term η between the two species we arrive at

$$\mathbf{E} + \mathbf{v_b}\times\mathbf{B} = \eta\mathbf{J} + \frac{1}{ne}\mathbf{J}\times\mathbf{B} - \frac{1}{ne}\nabla\cdot\mathbf{P}_e + \frac{m_e}{ne^2}\left(\frac{\partial\mathbf{J}}{\partial t} + \nabla\cdot(\mathbf{J}\mathbf{v_b} + \mathbf{v_b}\mathbf{J} - \frac{\mathbf{J}\mathbf{J}}{ne})\right) \tag{2.23}$$

which is the generalized Ohm's law. In addition to the resistive term, $\eta\mathbf{J}$, the Equation (2.23) includes a Hall term $\mathbf{J}\times\mathbf{B}$, the electron pressure term, as well as a time-variation of the current density which can be interpreted as the contribution of electron inertia to the current flow. Furthermore, the final three terms provide a correction for small-scale variations and are often neglected.

The following assumptions can be made to simplify Equation (2.23). We can neglect the electron inertia term by assuming that the characteristic time scales of the processes we are evaluating are slow enough such that the electrons reach their final state before any field changes have occurred. Furthermore, the Hall term may be dropped if the ions are magnetized. In this case, the gyroradius of both the electrons and the ions are sufficiently small compared to the scale length of the fluid motion. At last, we can neglect the electron pressure term by assuming it to be much smaller compared to the final resistive term. With the assumptions made the simplified Ohm's law takes the following form

$$\mathbf{E} + \mathbf{v_b}\times\mathbf{B} = \eta\mathbf{J} \tag{2.24}$$

This is readily reminiscent of Ohm's law from electric circuit theory where it takes the shape $\mathbf{J} = \sigma\mathbf{E}'$, where $\mathbf{E}' = \mathbf{E} + \mathbf{v_b}\times\mathbf{B}$. Here σ is the plasma conductivity which is a measure of how efficiently the collection of charges responds to the electromagnetic fields. The reciprocal is the resistivity η which measures how strongly the plasma resists any current formation.

2.5 Diffusion and Frozen Flux

In a plasma with constant magnetic field, the plasma particles undergo a well-defined gyromotion due to the Lorentz force $\mathbf{F} = qm\mathbf{v} \times \mathbf{B}$. In the presence of a uniform electric field, this gyromotion is distorted in a regular manner such that a drift $\mathbf{v}_D = \mathbf{E} \times \mathbf{B}/B^2$ of the guiding center is incurred. Particles gyrating around a specific field line will typically continue with this gyromotion drift $\mathbf{v}_D$ unless its motion is inflicted by external processes. Inhomogeneities in the magnetic or electric fields that are comparable to the gyroradius of the particle, or temporal changes that are comparable to the gyroperiod will lead to a decoupling of the particle's gyromotion around the magnetic field. In the presence of external forces, a field line tied to cold plasma will also be set in motion. This is true for a plasma in motion as well. Whenever the plasma moves, the field line will follow. By combining Ohm's law Equation (2.24), Faraday's law, and Ampère's law (2.3) [6], we can investigate this more quantitatively,

$$\frac{\partial \mathbf{B}}{\partial t} = \underbrace{\nabla \times (\mathbf{v_b} \times \mathbf{B})}_{\text{Convection}} + \underbrace{\frac{1}{\mu_0 \sigma} \nabla^2 \mathbf{B}}_{\text{Diffusion}} \tag{2.25}$$

where we see that there are two sources of change to the magnetic field at a specific location in the plasma, namely *convection*, and *diffusion*. This is illustrated in Figure 2.4. The first term describes the convection of the magnetic field with the plasma moving at a velocity $\mathbf{v_b}$. If the plasma is at rest, the equation (2.25) reduces to

$$\frac{\partial \mathbf{B}}{\partial t} = \frac{1}{\mu_0 \sigma} \nabla^2 \mathbf{B}$$

with the solution of the amplitude yielding $B = B_0 e^{-t/\tau_d}$, where $\tau_d = \mu_0 \sigma_0 L_B^2$ is the magnetic diffusion time. If the plasma has a finite resistivity the magnetic field will diffuse across the plasma and smooth out local inhomogeneities. Let us look at the solar wind as an example. Based on a velocity of 500 km/s it takes the solar wind roughly 3.5 days to cover the Sun-Earth distance. Over this transit time, the magnetic field in the solar wind is permitted to diffuse across only the very short distance of 1 km! Hence, the magnetic field is practically frozen into the solar wind carried by the plasma particles.

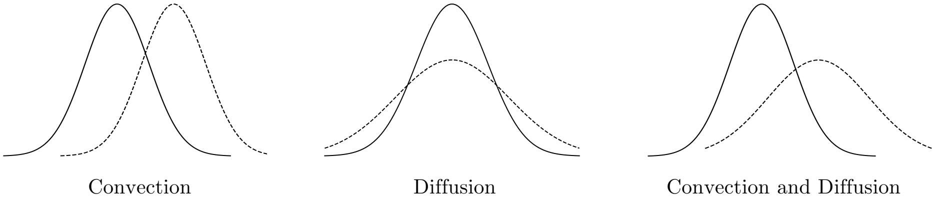

Figure 2.4: Illustration of the concept of convection and diffusion.

---

[6] Where the displacement current is neglected for velocities much smaller than the speed of light: $\frac{1}{c^2}\frac{\partial \mathbf{E}}{\partial t} \sim \frac{1}{c^2}\frac{E}{T} \sim \frac{1}{c^2}\frac{VB}{T} \sim \frac{1}{c^2}\frac{BV}{L}\frac{L}{T} \sim \frac{B}{L}\frac{V^2}{c^2} \approx 0$ as $v \ll c$

In the case of plasma with no diffusion (infinite conductivity $\sigma \to \infty$) equation (2.25) reduces to

$$\frac{\partial \mathbf{B}}{\partial t} = \nabla \times (\mathbf{v_b} \times \mathbf{B})$$

Here, any changes to the **B**-field are such that magnetic field are constrained to move with the plasma. The plasma elements will remain frozen to the magnetic field line and thus any motion of plasma particles will also alter the motion of the **B**-field - and vice versa. The plasma is therefore said to be *frozen in* to the magnetic field which may also be written as

$$\mathbf{E} + \mathbf{v_b} \times \mathbf{B} = 0 \tag{2.26}$$

and is further illustrated in Figure 2.5. This shows that in an infinitely conducting plasma there are no electric fields in the inertial frame of reference of the plasma. Thus, any electric field can only result by means of a Lorentz transformation. Furthermore, it is evident from Equation (2.26) that there are no electric fields parallel to **B**. The assumption of infinite conductivity results in a high mobility parallel to **B** and thus any local charge separations will immediately be cancelled out. The frozen-in condition is violated by the introduction of any form of a resistive term such that $\mathbf{E} \neq -\mathbf{v_b} \times \mathbf{B}$. The so-called diffusion region in magnetic reconnection, which we will talk about in the next section, is one example where this occurs.

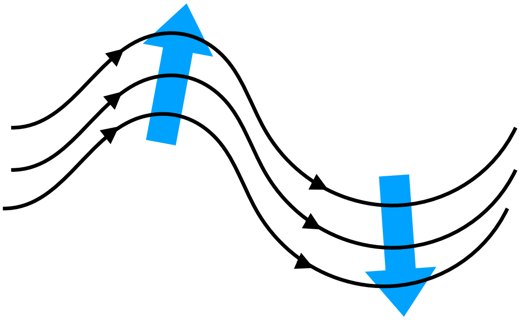

Figure 2.5: Illustration of the frozen-in phenomena. The blue arrows depict the plasma flow, whereas the black lines show the magnetic field lines.

2.6 The Concept of Magnetic Field Lines

In discussing phenomena regarding the dynamics and evolution of space plasmas the term *magnetic field lines* is widely used due to its convenience in depicting the form and topology of a magnetic field configuration. As the process of magnetic reconnection is quite extensively described and communicated as the *merging* and *cutting* of magnetic field lines, both in the scientific literature and to the general public, it is of essence that the fundamental concept of a magnetic field line is properly defined. A magnetic field line (or a field line in general) can be defined as a curve that is everywhere tangential to the magnetic field intensity **B** (*Parker*, 2016). This is illustrated in Figure 2.6. By evaluating the unit tangent vector $\mathbf{B}(\mathbf{x}_i)/|\mathbf{B}(\mathbf{x}_i)|$ at location $\mathbf{x}_i$ and moving a small distance of ds the next point on the field line is found, i.e.

$$\mathbf{x}_{i+1} = \mathbf{x}_i + \frac{\mathbf{B}(\mathbf{x}_i)}{|\mathbf{B}(\mathbf{x}_i)|} ds \Rightarrow \frac{dx_i}{ds} = \frac{B_i}{B} \tag{2.27}$$

Thus the magnetic field line through any point P is found by integration of Equation (2.27). Therefore, the set of all magnetic field lines associated with nearby points P' constitute a manifold which makes up the continuous magnetic field $\mathbf{B}$.

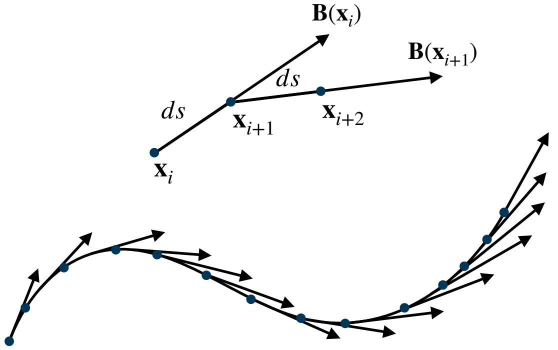

Figure 2.6: Constructing the magnetic field line

Chapter 3

Magnetic Reconnection

Magnetic reconnection is arguably one of the most important energy release and momenta transport processes in plasmas (see e.g. *Antiochos et al.* (1998); *Cassak et al.* (2007); *Gonzalez and Parker* (2016); *Goodman and Uzdensky* (2008); *Paschmann et al.* (1979); *Vasyliunas* (1975)). It is found to be operating in astrophysical plasmas, near Earth-space plasma, the stars, and in man-made plasma in laboratories on Earth. All of these environments are subject to the fundamental process of magnetic reconnection, which results in the release of stored magnetic energy and its conversion into thermal and kinetic energy of the charged particles. The energy release in the Earth's space environment is estimated to be up to 10^{16}J (*Weiss et al.*, 1992), and can be much larger in solar and astrophysical plasmas. As a result of this immense energy release, magnetic storms and solar eruptions are triggered, causing magnetic reconnection to be the engine ultimately behind the deleterious effects commonly referred to as space weather.

Even though magnetic reconnection has far-ranging effects on very large spatial scales, it is facilitated by processes on very small spatial scales. In collisionless plasmas, intricate interactions between charged particles and electromagnetic fields occur in a so-called *diffusion region*, which in the Earth's magnetosphere can be as small as 10-100 km, while the overall reconnecting system may extend to 10^5km. Inside this diffusion region, the charged plasma particles can no longer keep up their gyration around $\mathbf{B}$ and they hence become decoupled from the magnetic field due to either complex particle motions in regions with steep gradients or through wave-particle interactions. Let us look at an illustration of the reconnection process. In the simplest form, magnetic reconnection is a process in which the magnetic field topology changes. In Figure 3.1, we see the evolution of the merging process. We further see the two plasma elements located on the incoming magnetic field line[1] which are confined to the flux tube due to their gyromotion. Leading up to the onset of reconnection, magnetic flux is transported towards the center of the neutral region which, if the right conditions are met, will cause a thinning of the current sheet which subsequently gives rise to the characteristic X-point[2] geometry depicted in Figure 3.1. In the encounter of the anti-parallel field lines, the reconnection process initiates a change in connectivity of the plasma elements - i.e. plasma elements that initially stayed on the same field line end up on different field lines and are transported by the reconnection outflow. This is shown in Figure 3.1 where the yellow dots represents the plasma elements and the blue box de-

---

[1] See section 2.6 for a discussion of the concept of a magnetic field line.

[2] In 3D, this is generally referred to as the X-line.

picts the non-ideal MHD region where the frozen flux is violated which enables the breakdown and altering of the plasma-flux connectivity. The yellow and orange arrows represent the inflow and outflow regions, respectively. A picture put forward by

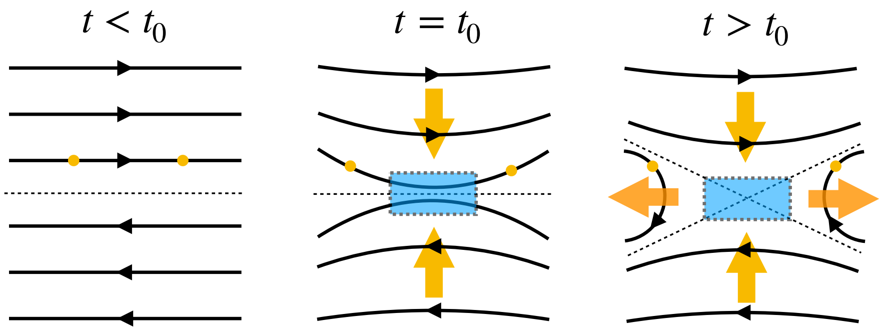

Figure 3.1: Illustration of magnetic merging.

Dungey (1961) provides insight into how magnetic reconnection plays an essential role in shaping magnetospheric dynamics. In Figure 3.2, we see the encounter of southward directed interplanetary magnetic field B_{IMF} with Earth's magnetosphere. As the

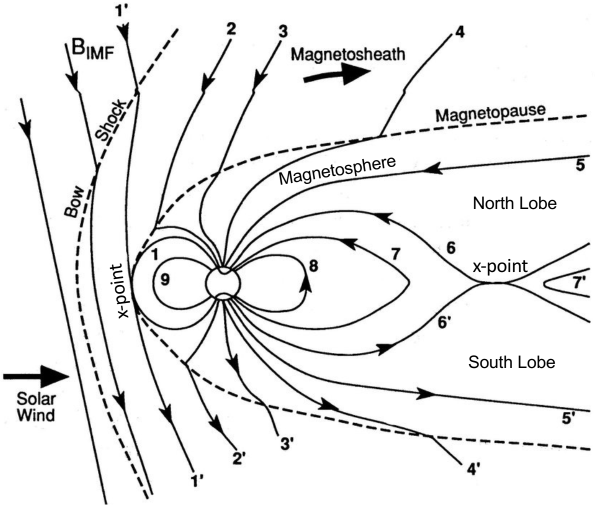

Figure 3.2: Illustration of the Dungey cycle. Adapted from Case (2014)

solar wind transports the IMF towards Earth's magnetosphere, the anti-parallel components of these fields, originating from different domains, may be subject to magnetic reconnection. The open[3] interplanetary magnetic field reconnects with the closed terrestrial field and a new open connectivity forms which are further transported from the dayside to the nightside. As the open magnetic flux is transported towards the magnetotail, the increased pressure imposed by the solar wind forces the flux together, and a

---

[3] The term *open* refers to a **B**-field connectivity extending far beyond the terrestrial magnetosphere.

new reconnection region is formed. Dungey's postulation quickly became the canonical paradigm for a description of magnetospheric dynamics. Merely 18 years after, the first in situ observation of reconnection at the magnetopause was confirmed by the ISEE satellites (*Paschmann et al.*, 1979). The conditions enabling reconnection at the dayside and nightside show clear dissimilarities. As the conditions in the magnetotail display clear symmetries for density, temperature, and the **B**-field the case is quite the contrary on the dayside. The region of dayside reconnection occurs at the intersection between two rather different plasma regimes - namely the magnetosheath and magnetosphere (*Cassak and Fuselier*, 2016). The conditions of the solar wind are perpetually changing causing the upstream conditions on the magnetosheath of the magnetopause side to vary greatly (*Levy et al.*, 1963). Thus, the parameters controlling the reconnection process vary greatly on each side with the asymmetric situation being the default cause. In particular, the asymptotic reconnection magnetic field difference on each side may be around 2, with the magnetospheric magnetic field being the strongest. The density on the magnetosheath side is typical of the order of 10-100 times greater than on the magnetosphere. Furthermore, the plasma temperature on the magnetospheric side typically reaches values 1000 times greater than on the magnetosheath side (*Cassak and Fuselier*, 2016). The typical magnetospheric and magnetosheath values are summarized in Table 3.1 provided by *Cassak and Fuselier* (2016).

Magnetospheric parameter	Typical value
n_{ms} (cm^{-3})	0.1
B_{ms} (nT)	56
$T_{i,\text{ms}}$ ($\times 10^5$ K)	2.4×10^3
$c_{A,\text{ms}}$ (km/s)	3.9×10^3
β_{ms}	0.27

Subsolar magnetosheath parameter (Derived)	Mean	Most probable	Median	5–95 % range start	5–95 % range stop
n_{sh} (cm^{-3})	34.8	20	27.6	12	80
B_{sh} (nT)	24.8	20.4	22.4	8.8	39.6
$T_{i,\text{sh}}$ ($\times 10^5$ K)	12	5	9.5	1	30
$c_{A,\text{sh}}$ (km/s)	92	99	93	55 (21)[a]	97 (250)[a]
β_{sh}	2.4	0.8	1.8	0.5	5.3
$\Delta\beta$	2.1	0.5	1.5	0.2	5.0

Table 3.1: Magnetospheric and magnetosheath plasma parameters. Adapted from Cassak and Fuselier (2016).

In Figure 3.3, we see an example of dayside magnetopause reconnection reported by the Magnetospheric Multiscale (MMS) mission. On the 8th of December 2015, MMS entered the magnetopause boundary layer from the magnetosheath side and crossed the magnetopause during the time of active reconnection (*Burch and Phan*, 2016). The event displays reconnection signatures in agreement with theory and earlier observations *Paschmann et al.* (1979). In panels 3.3b), 3.3e), and 3.3i)-j), we see the readings of **B**, density, and ion and electron temperature, respectively, as MMS advances through the magnetopause. Here, MMS clearly captures the asymmetric nature of dayside magnetopause reconnection: 1) asymptotic reconnection magnetic field ratio, $|B_{L,ms}/B_{L,sh}| \approx 2$, 2) density ratio of $n_{\mathsf{sh}}/n_{\mathsf{ms}} \approx 10$, and, finally 3) a temperature ratio of $T_{\mathrm{ms}}/T_{\mathrm{sh}} \approx 10^3$. The coordinate system used here is referred to as the *boundary normal coordinate system* in which L is along the reconnecting magnetic field direction, M is along the X-line direction, and N is along the magnetopause normal. In this event, the MMS spacecraft entered the reconnection site from the magnetosheath with features as high density (11 cm^{-3}), southward ($B_L < 0$) and duskward ($B_M < 0$) pointing magnetic magnetic field along with $v_L \sim -140$ km/s and $v_L \sim -90$ km/s.

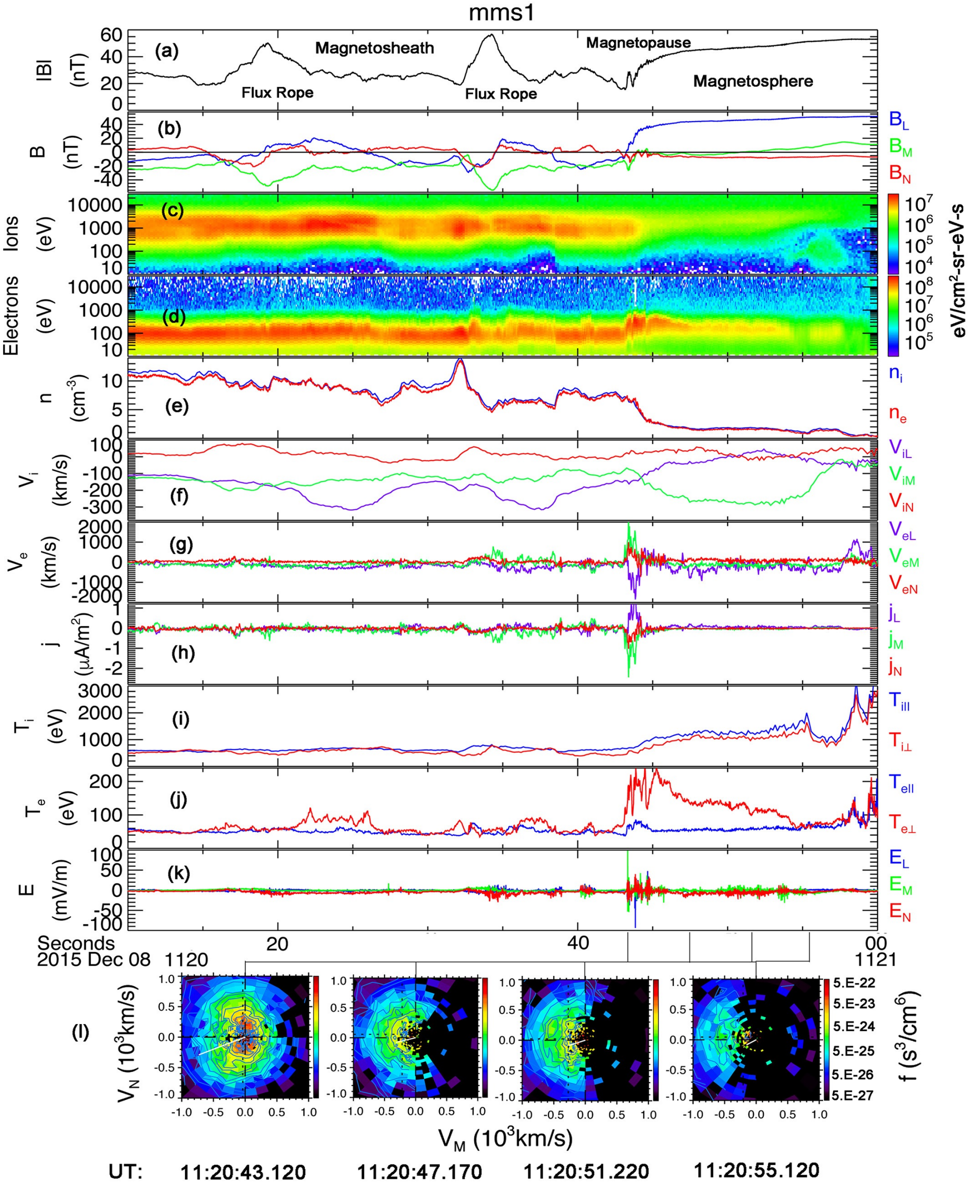

Figure 3.3: MMS observation of dayside magnetopause reconnection. Adapted from Burch and Phan (2016)

Around 11:20:45, we see clear indications of a magnetopause crossing near the X line during active reconnection with strong electron outflows $|v_L| > 1000$ km/s, intense current densities, electron heating, and electric fields in the excess of 100 mV/m. Additionally, at the same time, we see the very clear signature of field reversal of the reconnecting magnetic field B_L along with the evident density drop and temperature increase.

In the next section, we look into theoretical descriptions of magnetic reconnection.

3.1 Theoretical efforts to tackle Reconnection

Motivated by the studies of solar flares, *Giovanelli* (1947) searched for a possible mechanism enabling such vast energy releases in the solar corona. At a conference in 1956[4], Sweet proposed that by forcing two plasmas with oppositely directed magnetic fields together, resistive diffusion is able to occur on length scales much shorter than a typical equilibrium length scale (*Sweet*, 1958). Based on the physical picture put forward by Sweet, *Parker* (1957) developed the first self-consistent theory of magnetic reconnection further noting its importance in the conversion of stored magnetic energy to the thermal and kinetic energy of the plasma particles: *"We suggest that Sweet's mechanism may be of great importance in producing reconnection of the lines of force of a magnetic field into a configuration such that its energy becomes available for mechanical motions, etc." Parker (1957).* In the following section, we will give a quick look at the historical theoretical efforts to tackle the reconnection problem.

3.1.1 Magnetohydrodynamic models

In the Sweet-Parker model, the reconnection process takes place in a current sheet with a thickness of $2l$ and lengths of $2L$. As the incoming magnetic field B_i, transported at a velocity v_i, enters the current sheet, diffusion occurs causing the conversion of stored magnetic energy to kinetic energy. Finally, after diffusion takes place, the energetic plasma exists in the outflow region with v_o and with the weakened magnetic field B_o. The Sweet-Parker takes the basis of a two-dimensional steady-state reconnection process with an incompressible ($\rho_i = \rho_o = \rho$) MHD fluid.

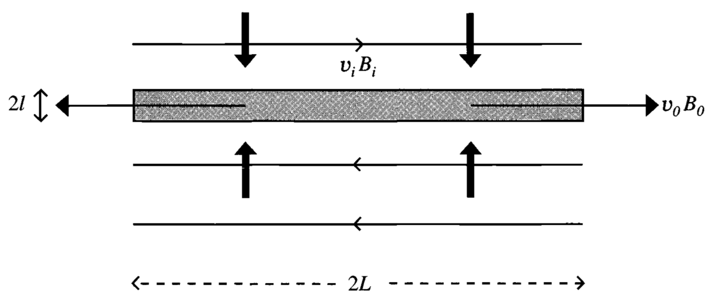

Figure 3.4: Illustration of Sweet-Parker set up. Adapted from Priest and Forbes (2000)

---

[4] Not published until 1958.

Let us consider the force balance between the inflow region and the current sheet. Let x be the outflow direction, y in-to the plane, and z the inflow direction. The MHD momentum equation (2.22) for the upstream region gives

$$\mathbf{j}\times\mathbf{B}-\nabla p=\frac{1}{\mu_0}\mathbf{B}\cdot\nabla\mathbf{B}-\nabla\left(\frac{B^2}{\mu_0}+p_i\right)=\rho\mathbf{v}\cdot\nabla\mathbf{v}\approx 0 \tag{3.1}$$

Where we assume small inflow velocities such that $\mathcal{O}(v^2)\approx 0$. As the magnetic tension force and all terms in the x-direction vanishes by symmetry, we arrive at

$$\frac{\partial}{\partial z}\left(\frac{B_i^2}{2\mu_0}+p\right)\approx 0\Rightarrow\frac{B^2}{2\mu_0}+p_i=p_{NR} \tag{3.2}$$

where p_{NR} denotes the pressure in the neutral region. The next step is to evaluate the force balance in the outflow region. Here the momentum equation yields

$$\rho\mathbf{v}\cdot\nabla\mathbf{v}=\mathbf{j}\times\mathbf{B}-\nabla p\approx-\nabla p \tag{3.3}$$

The outflow velocity v_o has now a considerable magnitude due $\nabla\cdot v=0$ and thus can not be neglected. The magnetic field strength in the outflow region B_o is further considered very weak and neglected. The x-component thus gives

$$\frac{\partial}{\partial x}\left(\frac{\rho v_o^2}{2}+p_o\right)\approx 0\Rightarrow\frac{\rho v_i^2}{2}=p_{NR} \tag{3.4}$$

Equating the expression for the force balance in the inflow and outflow regions we obtain

$$\frac{B_i^2}{2\mu_0}=\frac{\rho v_o^2}{2}\Rightarrow v_o=\frac{B_i}{\sqrt{\mu_0\rho}}=v_{Ai} \tag{3.5}$$

From an energy perspective, this shows that the entire magnetic field energy is converted to kinetic energy. Furthermore, we see that the outflow velocity is equal to the Alfvén velocity in the inflow region v_{Ai}. This result is completely independent of the shape of the diffusion region.

As reconnection powers large-scale phenomena, it is of utmost importance for any theoretical model to accurately predict the rate at which reconnection proceeds. We see from equation (3.5), that the amount of magnetic flux processed is dependent on the inflow speed. Therefore, if we can find an expression for the inflow velocity, we can estimate the rate of reconnection. The into-plane electric field must remain spatially constant due to the time-independent nature of the system. We thus get, simply from Ohm's law, the electric field in the three regions

$$E=-v_iB_i=\eta j_{NR}=\eta\frac{B_i}{\mu_0 l} \tag{3.6}$$

where η is the neutral region resistivity, and j_{NR} is the into-plane current. Let us further apply the continuity equation $\nabla\cdot\mathbf{v}=0$ which gives, $v_iL=-v_ol$, and combine it with equation 3.6 to get

$$v_i=-\eta\frac{1}{\mu_0 l}=\frac{\eta}{\mu_0}\frac{v_o}{v_iL}=\frac{\eta}{\mu_0}\frac{v_{Ai}}{v_iL}\Rightarrow\frac{v_i^2}{v_{Ai}^2}=\frac{\eta}{\mu_0 Lv_{Ai}}=\frac{1}{S} \tag{3.7}$$

where we have introduced the inflow Lundquist/Magnetic Reynolds number $S = \mu_0 L v_{Ai}/\eta$ which is a ratio of the time scales of diffusion to convection. Thus we obtain an expression for the reconnection rate

$$\frac{v_i}{v_{Ai}} = \frac{1}{\sqrt{S}} \tag{3.8}$$

In practice, the reconnection rate predicted by the Sweet-Parker model is too slow due to the extended nature of the diffusion region causing very slow inflow speeds. Typical parameters in solar flares are $S \sim 10^8$, (with $v_A \sim$100 km/s, and $L \sim 10^4$km) which indicates that the magnetic energy is released to the plasma via reconnection on a typical time-scale of a few tens of days. In reality, the typical energy-release time occurs over a few minutes to an hour. Thus the Sweet-Parker model can not sufficiently describe the explosive releases of energy observed in the solar flares (*Baumjohann and Treumann*, 1996). A model put forward by *Petschek* (1964) enabled fast reconnection mode. In the Petschek model, the inflow and outflow regions are separated by stationary slow mode shocks. These shocks extend outwards from a central Sweet-Parker current layer where the aspect ratio of the diffusion region is on the order of unity. Although the Petschek model enables fast reconnection modes, it has some serious drawbacks. The results are purely based on analytical assumptions, and furthermore, no numerical simulation with constant resistivity has reproduced Petschek reconnection *Baty et al.* (2009); *Forbes* (2001); *Kulsrud* (2001); *Shibayama et al.* (2019)[5].

3.1.2 Fluid models of Magnetic Reconnection

The fact that the Sweet-Parker model provides insufficient predictions to the reconnection rate, indicates that the physics of magnetic reconnection requires a far more detailed description. In the MHD description, one omits effects arising due to the relative motions of the electrons and protons. Furthermore, as the space plasma is highly collisionless the resistive term η, which includes collisional effects, is omitted. We thus obtain the two-fluid, collisionless, Ohm's law (*Sonnerup*, 1979)

$$\mathbf{E} + \mathbf{v_i} \times \mathbf{B} = \frac{1}{ne}(\mathbf{J} \times \mathbf{B} - \nabla \cdot \mathbf{P_e}) + \frac{m_e}{ne^2}\left(\frac{\partial \mathbf{J}}{\partial t} + \nabla \cdot (\mathbf{J}\mathbf{v_b} + \mathbf{v_b}\mathbf{J} - \frac{\mathbf{J}\mathbf{J}}{ne})\right) \tag{3.9}$$

$$\mathbf{E} + \mathbf{v_e} \times \mathbf{B} = \frac{1}{ne}\nabla \cdot \mathbf{P_e} + \frac{m_e}{ne^2}\left(\frac{\partial \mathbf{J}}{\partial t} + \nabla \cdot (\mathbf{J}\mathbf{v_b} + \mathbf{v_b}\mathbf{J} - \frac{\mathbf{J}\mathbf{J}}{ne})\right) \tag{3.10}$$

By treating the system as a two-fluid model, rather than a single MHD fluid, we arrive at a vastly more detailed description of the underlying dynamics occurring within the region of diffusion. Due to the significantly higher mass of the protons, as compared to the electrons, $m_p/m_e \approx 1836$, their respective dynamics in the reconnection region thus differ greatly. The much larger mass of the protons results in a much lower gyroperiod Ω_p around $\mathbf{B}$. If a proton and electron are to gyrate around the same magnetic field line, the electron would have proceeded 1836 gyrations at the time it takes the proton to complete one[6]. It is thus evident that the electrons are able to respond much faster to

---

[5] Although localized enhanced resistivity does give a Petschek-like behaviour (see e.g. (*Baty et al.* (2014); *Uzdensky* (2003)))

[6] For reference: One O^+ gyration correspond to $\sim$ 30000 electron gyrations

any **B**-field variations and they are, therefore, deemed to have a higher coupling to the magnetic field than the heavier species.

Generation of Hall Fields and Formation of an X-line

Imagine the case of two-dimensional collisionless reconnection seen in Figure 3.5. As the magnetic flux tubes are transported towards the reconnection region, the plasma species continue with their gyration around **B**. When incoming plasma gets closer to the current sheet region, the large gyration orbit of the protons causes them to decouple from the magnetic field. This marks the entry of the ion diffusion region (IDR) and is depicted as the grey region in Figure 3.5. Inside this region, the electrons are the only plasma species subject to magnetization. The two plasma species are now set to follow different trajectories as the ions are no longer confined to any field lines and the electrons continue to be convected with the magnetic field. The electrons remain magnetized until the entry of the electron diffusion region (EDR) depicted as the yellow region in Figure 3.5. Here, the gyroradii of the electrons exceeds the current sheet thickness causing a breakdown of the frozen-in behavior, i.e. $\mathbf{E}+\mathbf{v}_e\times\mathbf{B}\neq 0$. The distinctive motion of the electrons and protons within the reconnection region results in the characteristic planar Hall current systems which can be seen as the blue and red arrows in Figure 3.5. We further see the generation of the out-of-plane Hall magnetic field, due to the in-plane currents formed by the decoupled motions of the plasma species.

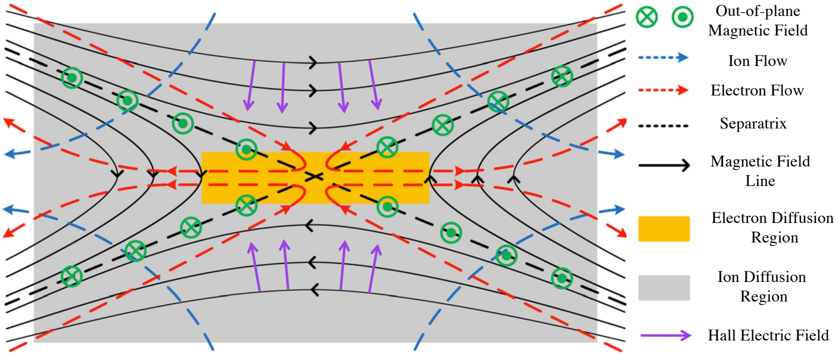

Figure 3.5: Depiction of the reconnection geometry for a simple planar reconnection. Adapted from Yamada et al. (2015)

The reconnection system itself shows a distinct geometry. As reconnection proceeds, and field line breaking occurs, the plasma is ejected in the outflow forming separate regions divided by the newly reconnected field lines. The oblique dark-dashed lines separating the inflow and outflow region, and intersecting in the center at the X-line, are known as the separatrices.

Processes Affecting the Hall Fields

Differences in the inflow conditions, such as magnetic field variations, plasma composition, and number density asymmetries greatly impact the dynamics of the plasma species which in turn shows significant alternation of the resulting Hall electric and magnetic fields (*Mozer et al.* (2008), *Markidis et al.* (2011), *Dai* (2018), *Kolstø et al.* (2020a)). Figure 3.6 shows an overview of the generation of the Hall electric E_z and Hall magnetic fields B_y for three simulational studies each with different conditions. The simulations are 2.5D particle-in-cell simulations such that fields and velocities are 3D whereas the spatial extent is 2D (x,z). The fields are taken when similar amounts of magnetic energy have been converted in each simulation. The in-plane velocities of the protons (white/brown) and electrons (black) are overlaid B_y, illustrating how the inflow is affected by varying the reconnection parameters and how, in turn, this flow alters the out-of-plane Hall magnetic field.

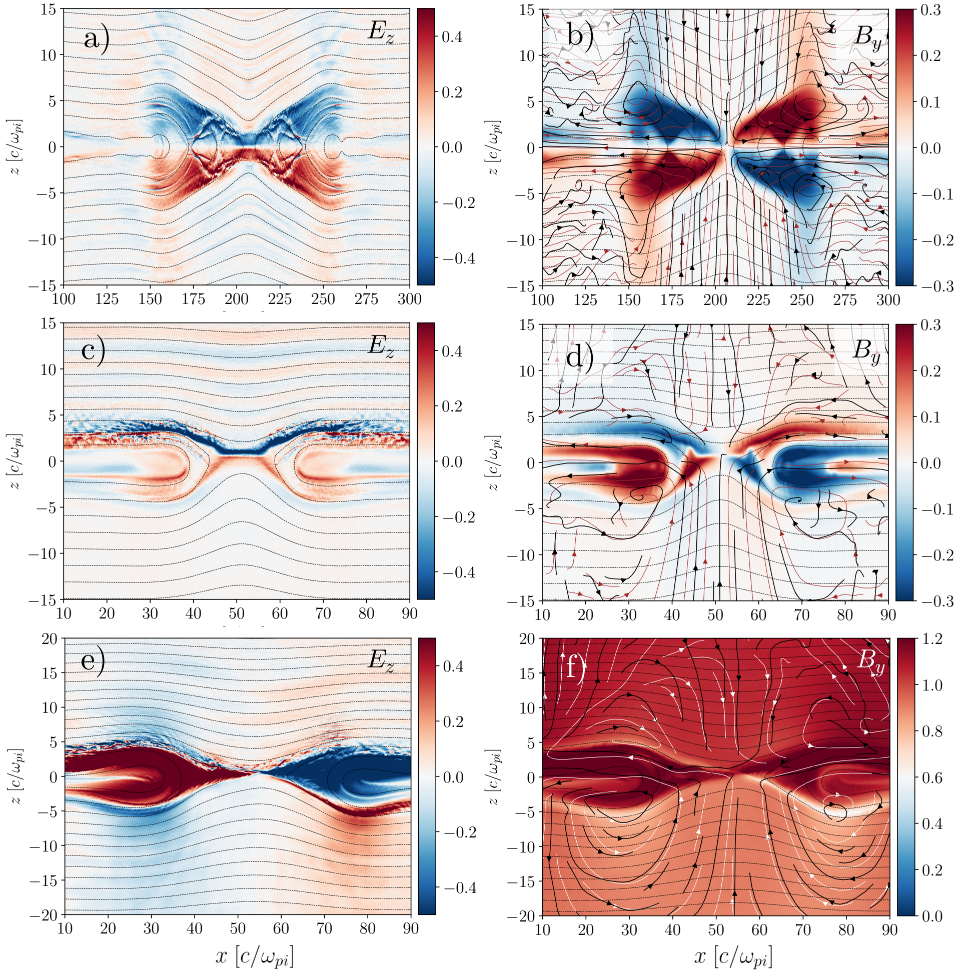

Figure 3.6: Three particle-in-cell simulations with different inflow conditions displaying distinct Hall fields E_z (left) and B_y (right) for each case. In the B_y plots, the velocity vectors are overlaid for the protons (white/brown) and electrons (white).

Panels 3.6a-b shows the fields for a symmetric reconnecting system; both the number densities and the magnetic field magnitudes are the same in each inflow region. This consequently generates symmetric (a) Hall electric field and (b) Hall magnetic field signatures and are in close agreement with the simple illustration of planar reconnection depicted in Figure 3.5. Panels 3.6c-d display the fields in the case of reconnection with north-south lobe asymmetries in the magnetic field strength, density, and temperature across the current sheet (z-direction). To preserve flux conservation, the inflow velocity in the southern lobe must exceed that of the northern lobe, such that,

$$E_y \approx -v_z^U B_x^U \approx -v_z^L B_x^L \text{ gives } |v_z^L| > |v_z^U| \text{ as } |B_x^U| > |B_x^L|$$

where indices U and L refer to the upper and lower inflow regions, i.e. the north and south lobe, respectively. This in addition to the lower field magnitude causes the decoupled motion of the electrons and protons ($\Omega_s \sim B$) to eventuate over a larger region resulting in a weaker and extended Hall electric field as compared to the northern lobe. This is seen in panel 3.6c. Similarly, the differences in the inflow velocity and magnetic field coupling alter the characteristic quadrupole signatures (seen in panel 3.6b) and accentuates the field strength and extent in the lower inflow region.

Panels 3.6e-f represent the same setup as that in 3.6c-d, with the addition of a strong B_y guide field component (of comparable size to the asymptotic B_x value). The introduction of a guide field component greatly impacts the characteristic Hall field signatures in the reconnection domain. As the plasma is ejected out in the exhaust, it encounters a strong B_y component which gives rise to electric field signatures ($E_z \approx -v_x B_y$) which are generated in addition to the Hall electric fields. The simulations presented above have been designed and executed by the author and include an additional heavy plasma species to represent oxygen ions. The effects of O^+ are discussed later in this chapter (see section 3.2.4).

Reconnection Electric Field in Fluid Models

In order for magnetic reconnection to take place, there must be some diffusive processes taking place to sustain the reconnection electric field. In the Sweet-Parker and Petschek models, the diffusion was enabled by a resistive term $\eta \mathbf{j}$. However, in a collisionless plasma, the nature of the diffusion is not immediately obvious. As stated before, in order for diffusion to take place a violation of the frozen-in condition needs to be met. Thus, if frozen-in is violated at the electron scale, is by necessity violated for all plasma species. Therefore, in order to investigate the underlying mechanism which sustains the electric field in the reconnection region, we investigate Ohm's law for the electron fluid (e.g. *Hesse et al.* (1995)).

$$\mathbf{E} = -\mathbf{v}_e \times \mathbf{B} - \frac{1}{n_e e} \nabla \cdot \mathbf{P}_e + \frac{m_e}{e} \left(\frac{\partial \mathbf{v}_e}{\partial t} + \mathbf{v}_e \cdot \nabla \mathbf{v}_e \right) \tag{3.11}$$

By virtue of Faraday's law, the electric field sustaining diffusion needs to be rotational. Thus in the planar case where the y-direction is the out-of-plane direction we obtain the following for the reconnection electric field (*Lyons and Pridmore-Brown*, 1990; *Vasyliunas*, 1975)

$$E_y = -\mathbf{v}_e \times \mathbf{B} \cdot \hat{y} - \frac{1}{n_e e} \left(\frac{\partial}{\partial x} P_{xy}^e + \frac{\partial}{\partial z} P_{zy}^e \right) + \frac{m_e}{e} \left(\frac{\partial}{\partial t} + \mathbf{v}_e \cdot \nabla \right) v_{ey} \tag{3.12}$$

It is to be noted that equation (3.11) must hold self-consistently for all plasma species, including the electrons, which we show here. Terms important for sustaining the reconnection electric field in the diffusion region have been extensively studied by the use of numerical simulations (*Hesse et al.*, 1999, 2014, 2018; *Lapenta et al.*, 2017). At the location of the X-line, the dominant term for sustaining the reconnection electric field has been shown to be the gradients of the off-diagonal pressure tensor

$$E_y \approx -\frac{1}{n_e e}\left(\frac{\partial}{\partial x}P^e_{xy} + \frac{\partial}{\partial z}P^e_{zy}\right) \tag{3.13}$$

However, the inertial term contributes as well but only becomes important in the electron diffusion region where inertia comes into play, with the time derivative being of lesser importance (*Treumann and Baumjohann*, 2013). In a paper by *Hesse et al.* (2018), the authors discuss the physical foundation and role of the reconnection electric field arguing that it is twofold: 1) it is to maintain the current and, 2) to sustain the pressure in the diffusion region. The reconnection electric field's most fundamental role is that of current conservation. Any process giving rise to a reduction of the current density required by the magnetic field reversal across the neutral sheet will inevitably induce an electric field in the out-of-plane direction. As a consequence of Ampere's law, $\frac{1}{c^2}\frac{\partial \mathbf{E}}{\partial t} = \nabla \times \mathbf{B} - \mu_0 \mathbf{j}$, the electric field will continue to accelerate the charged particles such that the current density matches the curl of magnetic field. The time derivative of the electric is very small such that this current density adjustment occurs continuously (*Hesse et al.*, 2018).

The Reconnection Rate

A highly important quantity in a reconnection system is the reconnection rate. The magnetic reconnection rate provides information about how fast the process evolves and how much magnetic energy in the system is transformed into the kinetic and thermal energy of the plasma constituents per time. The reconnection rate is defined as the change in magnetic flux per time, i.e.

$$\frac{\partial \Phi_B}{\partial t} = \frac{\partial}{\partial t}\iint_A \mathbf{B}\cdot d\mathbf{A} = -\iint_A \nabla \times \mathbf{E}\cdot d\mathbf{A} = -\oint_C \mathbf{E}\cdot d\mathbf{l} \tag{3.14}$$

where Faraday's law and Stokes' theorem are used. Furthermore, A is the surface of integration containing the reconnected magnetic field and C is a closed curved along the reconnection electric field (which bounds **A**). This setup is depicted in the simple 2D planar reconnection system shown in Figure 3.7, where the coordinate is as follows: z is the inflow direction, x is the component of the reconnected field, whereas the y-component points in-to-the plane along the X-line direction.

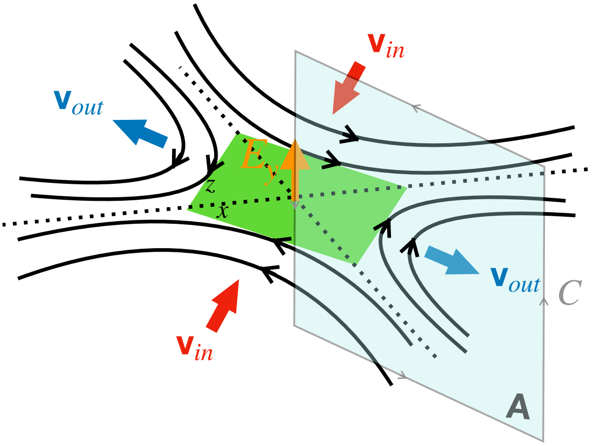

Figure 3.7: Illustration of the integration loop to determine the reconnection rate from the out-of-plane electric field.

The green surface in Figure 3.7, represents the diffusion region where dissipative processes enable flux annihilation. Counterclockwise integration along the closed-loop C according to Equation (3.14) gives $\partial t \Phi_B = \int E_y dy$, where it is assumed that the electric field far out is zero. It is thus evident that the amount of reconnected magnetic flux per time can be expressed as the integral of the out-of-plane electric field at the X-line. This field is referred to as the reconnection electric field denoted as the orange arrow.

3.1.3 General Magnetic Reconnection

So far, we have looked at the simple case of 2D planar reconnection. However, in nature, the most common case is that of 3D magnetic field configuration. In such 3D systems, the geometry of the reconnection system may be vastly more complex. *Schindler et al.* (1988) states that arbitrarily small three-dimensional perturbation of a two-dimensional plasmoid configuration in a reconnecting system may eliminate the possibility of defining separatrices. This lead to the proposition that instead of defining magnetic reconnection as dependent on the rearrangement of a specific topology, the general definition instead rely on the violation of the line conservation property - i.e. the breakdown of magnetic connection. This is the general foundation for the theory of General Magnetic Reconnection proposed by *Hesse and Schindler* (1988). Here the general requirement for reconnection to take place is dependence on the non-zero integral of the parallel electric field

$$\int E_{\|} ds \neq 0 \tag{3.15}$$

in which the integral is done along $d\mathbf{s}$ of a measurable set of field lines inside the diffusion region.

3.2 The Role of Ionospheric Ions in Magnetic Reconnection

Plasma found in Earth's magnetosphere originate either from the solar wind or the ionosphere. As energetic particles[7] from the Sun encounter Earth's atmosphere, atoms and molecules may be subject to ionization. Therefore, especially during the daytime, the top layer of Earth's atmosphere may be filled with charged particles. The ionized layer in the upper atmosphere is known as the ionosphere and particles from this region are continuously ejected into space.

In addition to the more common ion species, such as protons, many systems also include heavier species (*André and Cully*, 2012; *Baker et al.*, 1982; *Chappell et al.*, 1987; *Moore et al.*, 2001). Heavy ions originating from the ionosphere are typically cold, and may vary in density. For example, cold plasma arriving at the dayside magnetopause with the plasmaspheric drainage plume may have densities reaching several tens of cm^{-3} (*Zou et al.*, 2021). In contrast, the more dilute stream of ions leaving the polar regions may bring more cold plasma to both the dayside magnetopause and nightside lobes and plasma sheet. The additional cold, ion species, observed in both the dayside and nightside of Earth's magnetosphere, have their origin from the ionosphere (*André et al.*, 2016; *Borovsky and Denton*, 2006; *Fuselier et al.*, 2016; *Kistler and Mouikis*, 2016; *Toledo-Redondo et al.*, 2017) and can alter the reconnection process greatly by introducing distinct kinetic behavior and reducing the reconnection rate.

3.2.1 Origin of Ionospheric Ions

The ionization of Earth's upper atmosphere occurs primarily through photoionization due to, e.g., incoming extreme ultraviolet emission or other ionizing radiation (*Toledo-Redondo et al.*, 2021). Precipitating charged particles, for instance, accelerated electrons, also contribute to the ionization of neutral particles in energetic collisions which generate auroras. As the density decreases rapidly with height, the plasma becomes to a good approximation collisionless. This enables the light electrons to move to higher altitudes which gives rise to an ambipolar electric field causing outward acceleration of the positive ions along the geomagnetic field (*Axford*, 1968; *Banks and Holzer*, 1968). This constitutes the *classical* polar wind at high latitudes, carrying the lighter ions (H^+, He^+) out to the magnetosphere.

Further energization of the outflowing ions may be enabled by waves and parallel electric fields in the auroral and cusp regions (*André and Yau*, 1997; *Toledo-Redondo et al.*, 2021). Furthermore, the mirror force also provides parallel acceleration (*Comfort*, 1988). Ion transport to the magnetotail is made possible by the combination of the convection of magnetic field lines, as well as the parallel ion motion along the magnetic field direction (*Toledo-Redondo et al.*, 2021).

---

[7] Including photons

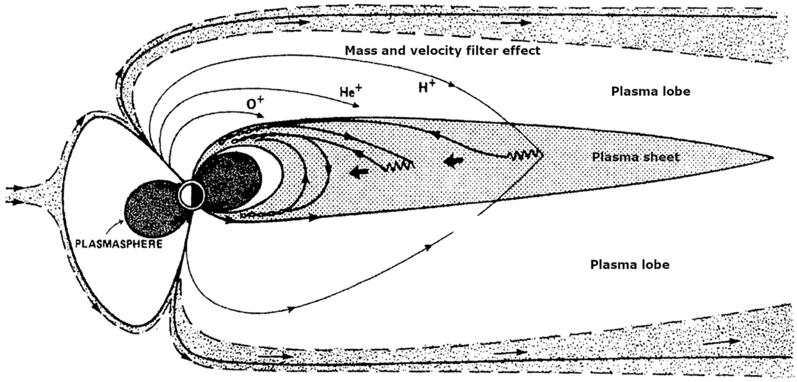

Figure 3.8: Illustration of ionospheric outflow. Adapted from Chappell et al. (1987)

The heavier ions such as NO^+, N^+, and O^+, are typically too massive to obtain the needed escape velocity through the sole mechanism of the ambipolar electric field. Upon acceleration by the electric field, these heavy ions are pulled back to the ionosphere by gravitational forces. As compared to the polar cap region, the auroral oval and cusp regions, which are the boundary between open and closed magnetic field lines, are home to additional processes which enable ion energization. In these regions, the charged particles are accelerated to higher energies than the ions originating from the polar cap (*Toledo-Redondo et al.*, 2021).

In addition to the ambipolar electric field, frictional forces between the neutrals and the charged particles affected by the convection electric field in the collisional part of the ionosphere may generate ion heating and upflow (*Schunk*, 2007). This additional energization can come in the form of waves generated far away from the local upflowing ion population (typically Alfvén waves), or carried by e.g. lower-hybrid waves. As the mass composition and the overall energy of the outflowing species are highly dependent on the ionospheric and magnetospheric conditions, several studies indicate that the major ion species comprising outflow from the dayside cusp and nightside auroral oval are H^+, He^+, and O^+ (*Craven et al.*, 1985; *Hoffman et al.*, 1974; *Ilie and Liemohn*, 2016; *Yau et al.*, 1993). These types of outflows are often referred to as energetic outflows and were the first indicators of the ionosphere being a source of plasma in the magnetosphere (*Shelley et al.*, 1972).

3.2.2 Observations of Heavy Ions in the Magnetosphere

Multispecies plasmas with the inclusion of oxygen ions have been widely observed by numerous spacecraft; polar-orbiting spacecraft (*Yau and André*, 1997), Geotail Spacecraft (see e.g. *Christon et al.*, 1998; *Kasahara et al.*, 2008; *Wilken et al.*, 1995; *Zong et al.*, 1998), Cluster mission (e.g. *Kistler and Mouikis*, 2016), and the Magnetospheric Multiscale mission (*Toledo-Redondo et al.*, 2016).

Lee and Angelopoulos (2014) used data collected from three spacecraft from the THEMIS constellation gathered over the course of five years (January 2008 - May 2013) to gain statistics on the abundance of cold and heavy ions on the dayside magnetosphere. They found that the median ratio of the number density of O^+ to protons were $n_{O^+}/n_{H^+} < 0.1$ in the dusk sector, and $n_{O^+}/n_{H^+} \sim 0.5$ in the dawn sector. In calculating the number density ratios, detections with total energies exceeding 1 keV are excluded. As opposed to the protons, which originate both from the solar wind and the ionosphere, the heavier ions, such as O^+, almost exclusively originate from the high-latitude ionosphere.

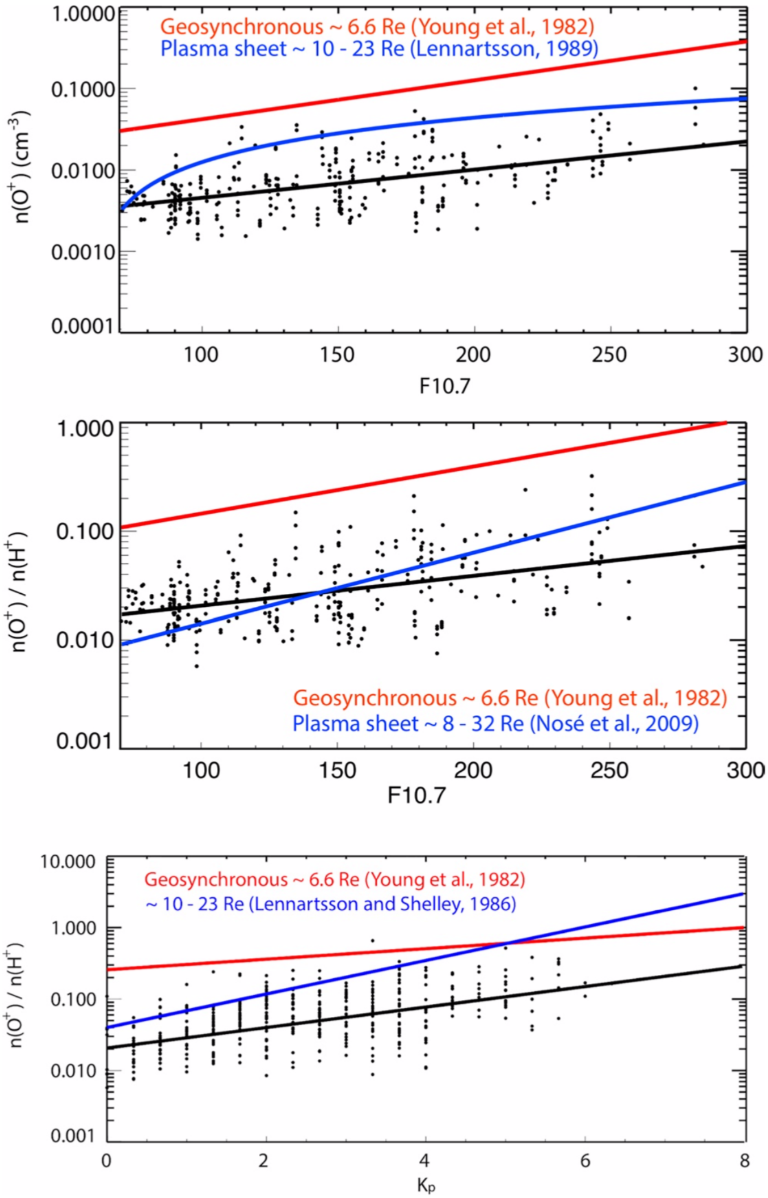

Figure 3.9: Oxygen number density as a function of solar radiation (F10.7) and substorm activities (Kp). Adapted from Mouikis et al. (2010).

Statistical studies of the mid-tail (10-30 R_E) plasma sheet ion composition were performed by *Lennartsson and Shelley* (1986) and *Lennartsson* (1989) using the Plasma Composition Experiment on ISEE 1, during the rise of solar cycle 21 in 1978 and 1979. This enabled them to compare the plasma ion composition with geomagnetic activity using the Auroral Electrojet (AE) index - which is a measure of the magnetic field perturbations in the auroral regions which are typically associated with substorm activity. It was found that the number density ratio n_{O^+}/n_{H^+} increased with the AE, ranging from 0.01 for low values of AE, to 0.6 for AE 1000 nT. This increase was due to a ten-fold O^+ density increase, from 0.02 cm^{-3} to 0.2 cm^{-3}, in addition to a reduction in the proton density by a factor of around 6.

Furthermore, the authors also showed a distinct increase of the O^+ density related to the solar EUV, increasing from 0.02 cm^{-3} to 0.08 cm^{-3} when the solar radio flux at 10.7 cm (known as the F10.7 index which is a good proxy for the solar EUV activity) increased from 50 solar flux units[8] (sfu).

Baumjohann et al. (1989) reported on ion number density values consistent with *Lennartsson* (1989) in the plasma sheet at 9-14 R_E by data collected from the AMPTE spacecraft. A statistical study was performed by *Nosé et al.* (2009) using 16 years of data from the STICS instrument on the Geotail spacecraft (9-212 keV) to examine the plasma sheet ion composition in ranges 8-100 R_E in comparison with solar cycle variability. The authors found that as F10.7 increased from 70 to 200 sfu, the oxygen ion to proton number density n_{O^+}/n_{H^+} increased from 0.01 to 0.06.

Mouikis et al. (2010) investigated H^+ and O^+ densities inside a more limited spatial range in the plasma sheet (15-19 R_E). By using 5 years of data (2001-2005) collected by the CIS/CODIF (40 eV - 40 keV) instrument from the Cluster mission the authors reported a similar increase in the O^+ density with F10.7. Although *Lennartsson* (1989) observed overall higher densities (seen in Figure 3.9a), which are likely due to the fact that the radial range extended to lower distances where the O^+ density is higher. In Figure 3.9b we see the comparison of the O^+/H^+ density ratio from the Cluster spacecraft (*Mouikis et al.*, 2010) with the Geotail spacecraft (*Nosé et al.*, 2009) as a function of F10.7 (solar EUV). Furthermore, in Figure 3.9c), we see the O^+/H^+ density ratio as a function of the Kp index (index used to characterise the magnitude of geomagnetic storms). *Young et al.* (1982) and *Kistler and Mouikis* (2016) characterised the plasma sheet densities closer to the Earth, at radial distances of $\sim 6-7$ R_E, and found that the O^+ density, as well as the O^+/H^+ density ratio, in this region was a factor of 10 higher than in the 15-19 R_E region. In both these regions, both n_{O^+} and n_{O^+}/n_{H^+} show similar dependencies with respect to the solar EUV (F10.7) and geomagnetic activity (Kp and AE). At larger radial distances, Solar EUV will increase the n_{O^+}/n_{H^+} ratio by a factor of ~ 8, which is later increased by another factor of 10 by geomagnetic activity (*Toledo-Redondo et al.*, 2021).

A mapping technique to derive 2D maps of the density of protons and oxygen ions in the XY-equatorial were utilized by *Maggiolo and Kistler* (2014) using data from the Cluster spacecraft. In Figure 3.10, we see n_{O^+} and n_{O^+}/n_{H^+} as a function of the equatorial X position. In agreement with *Young et al.* (1982) and *Kistler and Mouikis* (2016), we see strong enhancements of the O^+ density and O^+/H^+ density ratio closer to Earth. Furthermore, during high solar EUV, and geomagnetic activity, the profiles

---

[8] 1 sfu = 10^{-22} $Wm^{-2}Hz^{-1}$

are similar although shifted towards higher values. The authors did not observe any strong dawn-dusk asymmetries and they reported that the oxygen and protons density both remained similar across the magnetotail at distances of 15-20 R_E.

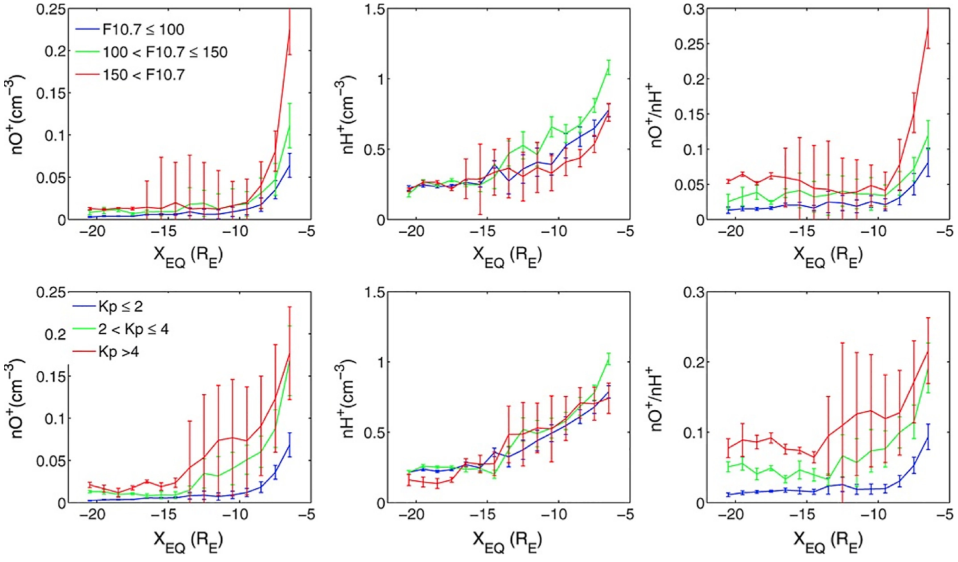

Figure 3.10: Number density of the oxygen ions as a function of the distance from the Earth in the equatorial X direction subjected to various solar radiation (F10.7) and substorm activities (Kp). Adapted from Maggiolo and Kistler (2014).

The studies mentioned thus far have mainly analyzed the hot plasma sheet population which are comprised of a fuse of heated ions originating both from the solar wind as well as from the ionosphere. In addition to the warmer populations, low-energetic cold ion populations of ionospheric origin may also be present in the plasma sheet. Due to their low-energy, typically less than ~ 10 eV (*Toledo-Redondo et al.*, 2021), these cold ions are often hard to detect in space plasmas. The main source of difficulty arises from the fact that a spacecraft in a low-density plasma may become positively charged (reaching 10V) when exposed to sunlight (*Garrett*, 1981; *Grard*, 1973; *Whipple*, 1981). As a consequence, low-energetic positively charged ions will simply not reach the spacecraft and hence a direct detection can not be performed. See *André and Cully* (2012) for techniques to overcome this issue.

Seki et al. (2003) presented an observation of the direct detection of cold ions in the plasma sheet by the use of the Geotail spacecraft. This direct detection was made possible due to the fact that the spacecraft were in eclipse by Earth's shadow resulting in a suppression of the photo-electric emission. Furthermore, this causes the spacecraft to charge negatively due to the impacting electrons from the ambient plasma. This negative potential can now attract the low-energetic ions and an direct detection is made possible. It is also to be noted that cold ions are directly detectable in the case when the ion plasma bulk drift energy exceeds the equivalent spacecraft potential energy *Alm et al.* (2018, 2019); *Xu et al.* (2019).

In a study performed by *Lee and Angelopoulos* (2014), the cold ion (energies less than 1 keV) densities in the near-tail plasma sheet ($6 - 12\ R_E$) was examined by the use of THEMIS data collected over a 5 year period (same study as mentioned above). They reported on an average proton density in the magnetotail of $0.05 - 0.1$ cm^{-3} with average temperatures of 10 eV. Furthermore, the average of He$^+$ and O$^+$ densities were also investigated and they reported on higher densities for the heavier species than for H$^+$ with ~ 0.1 cm^{-3} at 50 eV for He$^+$ and ~ 0.2 cm^{-3} at ~ 200 eV for the oxygen ions. In the table below (adapted from *Toledo-Redondo et al.* (2021)), the statistical observation of oxygen ions of ionospheric origin observed in the plasma sheet is summarized.

Observation	**Geometric Distance [R_E]**	**Observed** n_{O^+}/n_{H^+}	**Observed** n_{H^+} **[cm^{-3}]**	**Energy Range [keV]**
Young et al. (1982)	6-7	0.4-0.5 (Kp < 3) 0.5-0.9 (3 < Kp < 6) 0.9-1.4 (Kp > 6)	0.3-0.4 (Kp < 3) 0.4-0.5 (3 < Kp < 6) 0.5-0.6 (Kp > 6)	0.9-16
Gloeckler and Hamilton (1987)	8-9	0.11	0.35	1.5-315
Lennartsson and Shelley (1986)	<10	0.1	0.8	0.1-16
Lee and Angelopoulos (2014)	5-10	> 1	< 0.1	<1
Maggiolo and Kistler (2014)	7-8	0.2-0.3 (Kp < 3) 0.3-0.6 (3 < Kp < 6) 0.6-1.3 (Kp > 6)	0.5-0.7 (Kp < 3) 0.7-0.8 (3 < Kp < 6) 0.6-0.8 (Kp > 6)	1-40
Kistler and Mouikis (2016)	6-7	0.1 (Kp < 2) 0.1-0.2 (2 < Kp < 4) 0.2-0.5 (Kp > 4)	0.6-0.8 (Kp < 2) 0.8-1.3 (2 < Kp < 4) > 1.3 (Kp > 4)	-
Lennartsson and Sharp (1985)	10-23	0.1 (AE < 100 nT) 0.2-0.7 (AE > 300 nT)	-	0.1-16
Lennartsson and Shelley (1986)	10-23	0.01-0.08 (AE < 100 nT) 0.6 (AE > 700 nT)	0.5-1 (AE < 100 nT) 0.2-0.3 (AE > 700 nT)	0.1-16
Lennartsson (1989)	> 10	0.03 (F10.7 < 100) 0.05 ((100 < F10.7 < 150) 0.15 (F10.7 > 150)	0.65 (F10.7 < 100) 0.55 (100 < F10.7 < 150) 0.4-0.48 (F10.7 > 150)	0.1-16
Seki et al. (2003)	9-18	< 0.5	$\sim$ 0.2	< 1
Mouikis et al. (2010)	15-19	0.01-0.07	0.2-0.3	1-40
Maggiolo and Kistler (2014)	15-20	0.01-0.05 (Kp < 3) 0.05-0.2 (3 < Kp < 6) 0.2-0.7 (Kp > 6)	0.3	1-40
Frank et al. (1977)	$\sim$ 35	$10^{-3} - 10^{-2}$	3	0.5-45
Wygant et al. (2005)	$\sim$ 18	2.3 (0.7/0.3)	0.3	0.7-32

Observations of O$^+$ in the Plasmaspheric Lobes

Two highly important regions controlling the process of magnetic reconnection are the plasmaspheric lobes depicted in Figure 3.8. Magnetotail reconnection is first initiated in the plasma sheet where the magnetic field lines from the southern and northern hemisphere are stretched and forms a thin current sheet. As reconnection proceeds, magnetic field lines from the lobe regions, which are filled with ions originating from the high-latitude ionosphere, are transported toward the current sheet and contribute to the reconnection process. Therefore, understanding the composition and abundance of heavy ions in the lobe regions provide great insights into the mechanisms enabling and controlling reconnection. Oxygen ions in the plasmaspheric lobes has been characterized by *Liao et al.* (2010, 2012, 2015). The authors reported that during the solar maximum of 2001-2002 the occurrence frequency of oxygen ions in the lobes were close to 100% during storm time, and even 50% during quiet times. In the lobes, the

O^+ location shows a dawn-dusk asymmetry dependent on the IMF B_y component. If the B_y component is positive, oxygen ions in the north lobe shifts to the dawn side, while in the southern lobes it tends towards the dusk side. For negative B_y, the asymmetry is reversed but not to such a strong degree. Differences in ionospheric outflow between the northern and southern hemisphere may also give rise to asymmetrically distributed O^+ both in the north and south lobe as well as in the dawn-dusk direction (*Glocer et al.*, 2020; *Liao et al.*, 2010).

3.2.3 The Impact of Heavy ions on the Reconnection Process

Heavy ions play a key role in magnetospheric dynamics introducing new spatial scales and distinct kinetic behaviour (*Lotko*, 2007; *Maggiolo and Kistler*, 2014; *Shay and Swisdak*, 2004; *Toledo-Redondo et al.*, 2015). Due to their high mass, they contribute significantly to the plasma mass density scaling of the Alfvén velocity. During storm time conditions, the oxygen ions can in fact be the dominating species in the plasma sheet (*André and Cully*, 2012; *Kistler and Mouikis*, 2016; *Kistler et al.*, 2005, 2006; *Mouikis et al.*, 2010). The presence of O^+ in magnetic reconnection can also influence the Hall fields (*Lindstedt et al.* (2010), *Kolstø et al.* (2020a)) and alter the dynamics of dipolarization fronts (*Liang et al.*, 2017; *Markidis et al.*, 2011). Further effects arising with the inclusion of oxygen ions include altering the tearing mode growth rate (*Karimabadi et al.*, 2011), as well as the generation of ambipolar electric fields induced by charge separation (*Liang et al.*, 2016) which may contribute to the development of bifurcated current sheets (*George and Jahn*, 2020).

It is of importance to understand how additional plasma species with a different temperature or mass couple to the reconnection process. Distinct time and spatial scales introduced by the heavier ions alter the dynamics in the diffusion region and greatly affect how the process converts stored magnetic energy to plasma thermal and kinetic energy. Important quantities that provide insight into the coupling of a given plasma species s are the Larmor radius (or gyroradius) r_{gs} and the cyclotron frequency Ω_s

$$r_{gs} = \frac{m_s v_s^{th}}{q_s B} \qquad \Omega_s = \frac{q_s B}{m_s} \tag{3.16}$$

where v_s^{th} is the thermal speed, q is the particle charge, and B is the magnetic field magnitude. From this, we can see that heavy ions (e.g. He^+, O^+) will experience a much larger Larmor radius for similar thermal energies. Therefore, coupling to the magnetic field only occurs at much larger scales. As opposed to the Larmor radius, the gyrofrequency is independent of the particle energy. This consequently introduces different temporal scales for different plasma species regardless of their thermal energy. As discussed in the introduction of this chapter, the reconnection region is characterized by the different decoupling scales of the present plasma species. The decoupling scale of the electrons, the EDR, is embedded inside the ion decoupling scale, the IDR, due to the much larger mass of the ions. In a multi-species plasma, e.g. with the presence of oxygen ions, the reconnection region is compartmentalized even further. Due to the much larger spatial scales of the gyromotion of the oxygen ions, as compared to the protons, the IDR can be separated into two diffusion regions; the proton diffusion region (H^+DR) which is now embedded inside the oxygen diffusion region (O^+DR).

In Figure 3.11, we see an illustration of the multi-scale ion diffusion regions due to the O$^+$. Such multi-scale regions have been observed in both PIC simulations for both O$^+$ (*Liu et al.*, 2015) and cold ions (see e.g. *Divin et al.*, 2016; *Spinnangr et al.*, 2021), and in observations (*Toledo-Redondo et al.*, 2016).

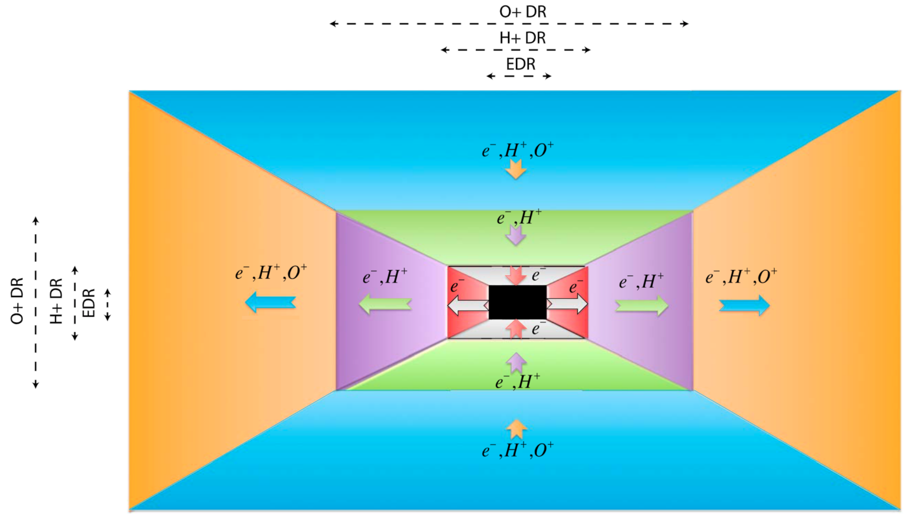

Figure 3.11: Multi-scale structure of the diffusion regions in the presence of both H$^+$ and O$^+$. Adapted from Liu et al. (2015).

As discussed in the previous section, the heavier ions of ionospheric origin can dominate the mass density on the magnetospheric side of the magnetopause, and in the magnetotail. Both are regions where magnetic reconnection takes place in the near-Earth environment. With the mass density being greatly modified, the reconnecting system becomes mass-loaded causing a change in the upstream Alfvén velocity which in turn directly modifies the reconnection efficiency - or reconnection rate.

Mass-Loading effect on the Reconnection Rate

In section 3.1.1, the Sweet-Parker analysis provided us with the reconnection rate in a simple, 2D steady-state magnetic reconnection process in which the normalized reconnection rate was readily defined as the ratio between the inflow and the outflow velocity. By assuming incompressible flow, $\nabla \cdot \mathbf{v} = 0$, the rate can further be related to the aspect ratio of the diffusion region,

$$M_A = \frac{v_{in}}{v_A} \sim \frac{l}{L}.$$

Furthermore, it is assumed that the value of the electric field is unchanged on the boundaries of the diffusion region such that, with $\nabla \cdot \mathbf{B}$, we obtain

$$E \sim v_A B_o = v_A B_i \frac{l}{L}$$

The reconnection electric field is dependent on the magnetic field strength and the mass density in the inflow region through the Alfvén velocity. Quantitatively, the increase of the mass density by an additional ion species, e.g. O^+, will lead to a reduction of the reconnection rate by a factor of $\sqrt{1+(m_{O^+}n_{O^+}/m_p n_p)}$. This is known as the mass-loading effect and may intuitively be depicted by inert flux tubes encumbering the transport of magnetic flux.

Several statistical studies have reported on observations of the mass-loading effect of magnetopause or magnetotail reconnection imposed by the presence of ionospheric ions (*Fuselier et al.*, 2017, 2019; *Walsh et al.*, 2013, 2014; *Wang et al.*, 2015). In situ observational studies of the mass-loading effect were first performed by *Su et al.* (2000) where they observed plasma from the magnetosheath and the plasmaspheric plume simultaneously in the same flux tube, indicating potential mass-loading during ongoing reconnection. *Wang et al.* (2015) reported that mass-loading by ionospheric ions may reduce the reconnection rate by as much as 20% . In a paper by *Fuselier et al.* (2019), the authors studied a situation in which, during periods of northward IMF, O^+ escapes from the high-latitudes and moves to the magnetopause where the abundance accumulates until the IMF turns southward and initiates reconnection. In this case, it was predicted that the reconnection rate can be reduced by as much as 32% by the participation of ionospheric oxygen ions.

Kinetic Effects of O^+ on the Reconnection Process

Due to the cyclotron frequency dependence on mass (Equation 3.16), the heavy ionospheric oxygen ions will introduce additional time scales. For a magnetic field of $B = 20$ nT (typical magnetotail lobe field strength), the gyroperiod of protons will approximately be 3 seconds. In comparison, the O^+ mass is 16 times that of the protons, leading to a gyroperiod of ~ 50 seconds. During an active time of reconnection lasting around 200 $\Omega_p^{-1} \sim 10$ min (e.g. a bursty bulk flow *Merkin et al.* (2019)), the oxygen ions will only have proceeded 12 gyrations about the magnetic field making it difficult for the O^+ to respond to changes by fast convection of the magnetic flux. Therefore, if the evolutionary timescale of reconnection is faster, or comparable, to the O^+ gyroperiod, the oxygen ions will be subject to demagnetization (*Markidis et al.* (2011), *Tenfjord et al.* (2018), *Tenfjord et al.* (2019), *Kolstø et al.* (2020a)). With the decoupling from the magnetic field realized, the effect of oxygen ions on the reconnection process can no longer be adequately attributed to the mass-loading effect. Particle-in-cell (PIC) simulations conducted by *Tenfjord et al.* (2018, 2019) and *Kolstø et al.* (2020a,b) investigated the behavior of oxygen ions in magnetotail reconnection. The authors found that as demagnetization was realized, the O^+ became ballistically accelerated primarily by the Hall electric field. This is in agreement with observations from the Cluster spacecraft (*Wygant et al.*, 2005). The PIC simulations further revealed that ballistic Hall field acceleration gives rise to the generation of O^+ density enhancements propagating as waves in the reconnection exhaust (*Tenfjord et al.* (2018), *Kolstø et al.* (2020a)). This predicted behavior was observed in magnetotail reconnection by the use of data collected from the MMS spacecraft (*Kolstø et al.*, 2021).

In the simulational studies conducted by *Tenfjord et al.* (2019) and *Kolstø et al.* (2020a) it was found that even though the oxygen ions were not magnetized, and hence not able to make the flux tubes inert by mass-loading, they still alter the reconnection rate. The authors propose a mechanism in which the demagnetized oxygen ions act as an energy sink in the system and thereby altering the energy partition. The rate reduction mechanism by the demagnetized species is possible due to the fact that the oxygen ions extract energy from the fields that otherwise would have gone to the acceleration of the electrons and protons. The authors further developed a scaling relation for the reduction of the reconnection electric field by the inclusion of a demagnetized species

$$E_{\text{rec}} \sim \left(1+\frac{n^U_{O^+}+n^L_{O^+}}{2n_p}\right)^{-1} v_A B_0 \tag{3.17}$$

where $n^U_{O^+}$ and $n^L_{O^+}$ refers to the O^+ density distribution on either side of the current sheet, whereas n_p is the proton density. Furthermore, v_A is the Alfvén velocity which is calculated with the basis of the proton peak density in the current sheet and the asymptotic value of the magnetic field B_0 for the Harris profile.

In Figure 3.12, we see an overview of the reconnection rate by different configurations of O$^+$. In Figure 3.12a, the reconnection rate is shown for 6 different simulation runs with O$^+$ number density ranging from 0-0.4 in units normalized to the foreground current sheet density.

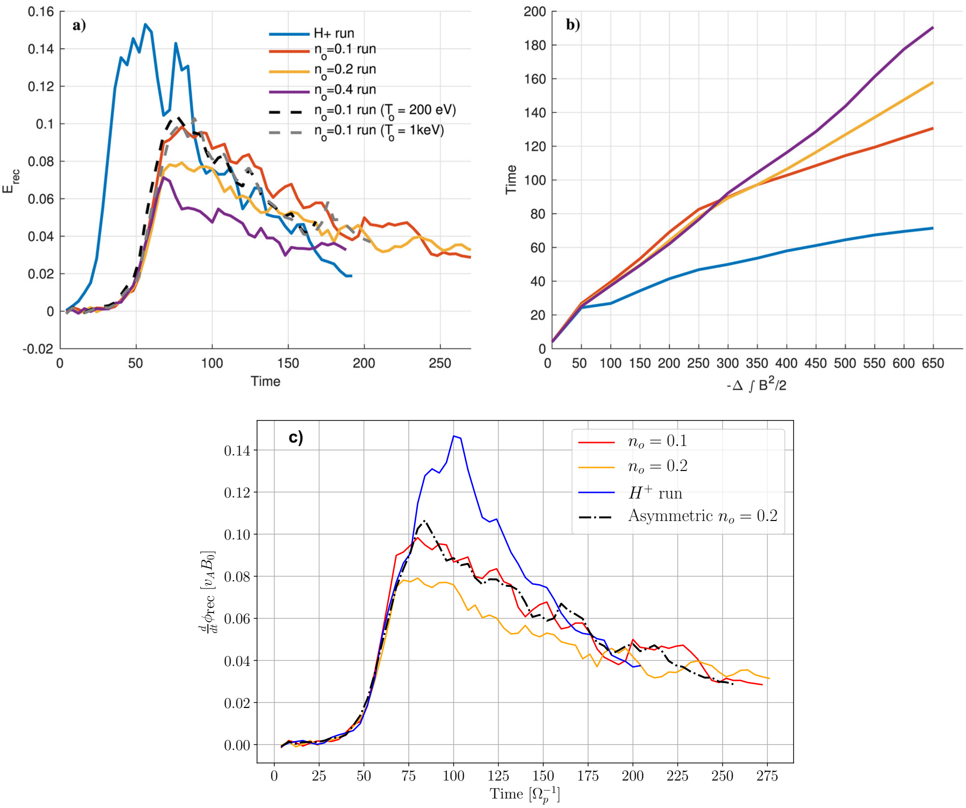

Figure 3.12: a) Reconnection rate and b) reconnected flux for different oxygen abundance adapted from Tenfjord et al. (2019). c) Reconnection rate for different spatial configurations of the oxygen density adapted from Kolstø et al. (2020a).

As indicated by the scaling relation (3.17), the reconnection rate reduces with an increasing abundance of O^+ but shows no dependence on the initial thermal energy of the oxygen ions. In Figure 3.12c, we see the reconnection rate for systems with different oxygen number densities and lobe configurations - symmetric and asymmetric. Of particular interest is the clear agreement between the reconnection rate of the symmetric density configuration ($n^U_{O^+} = n^L_{O^+} = 0.1$) (red) and the asymmetric density configuration ($n^U_{O^+} = 0.2$, $n^L_{O^+} = 0$) (black dash-dotted line). This reveals that the reconnection rate is dependent on the average density distribution of the oxygen ions in the system. This is also captured by Equation (3.17).

As previously stated, traditional mass-loading effects cause a reduction of the reconnection rate by a factor of $\sqrt{1+(m_{O^+}n_{O^+}/m_p n_p)}$. As an example, *Wygant et al.* (2005) reported on density conditions during magnetotail reconnection by the use of Cluster reading $n_{O^+} = 0.07$ cm^{-3} and $n_p = 0.03$ cm^{-3}. This leads to a reduction of the reconnection rate of a factor of 6.3 through the mass-loading effect, and 3.3 for the proposed scaling relation, Equation (3.17). The new scaling relation obtained by considering the kinetic behavior of heavier plasma species have great implications for magnetospheric dynamics. During some phase of the evolution of the reconnection process, this might imply that the dynamics of geomagnetic storms and substorms evolve twice as fast as expected when oxygen is present (*Kolstø et al.*, 2020a; *Tenfjord et al.*, 2019).

Even if the oxygen ions exhibit a demagnetized behavior during phases of fast flux transport, they are still able to alter the dynamics in the region of reconnection. Ionospheric ions entering the magnetotail stream parallel to the magnetic field lines at velocities reaching up to $\sim$ 50 km/s (*André et al.*, 2015; *Bouhram et al.*, 2004; *Fuselier et al.*, 2019; *Haaland et al.*, 2012). These tailward streaming ions contribute to the overall momentum balance thus altering the reconnection dynamics. In a simulation performed by *Tenfjord et al.* (2020), the effect of cold tailward streaming ($0.5v_A$) protons on the reconnection process was investigated. The streaming cold protons deposits parts of their momenta in the reconnection region resulting in a tailward propagation of the X-line corresponding to the center of mass velocity. To investigate whether this coupling between the streaming ions and the reconnection region also held for heavier ions that remain demagnetized over longer times and larger scales, *Kolstø et al.* (2020b) initiated a similar study in which the the effect of tailward streaming oxygen ions on magnetotail reconnection is investigated. The authors found that despite its demagnetized behaviour, the oxygen ions still impart their tailward directed momentum through an electrostatic coupling with the electrons. This causes a motion of the X-line also corresponding to the center-of-mass velocity. These findings suggest that a demagnetized species alters the dynamics of the reconnection site long before the time of magnetization is realized. Further, it shows that, regardless of whether the streaming population is magnetized or not, the system will reorganize itself in such a manner as to retain a net zero outflow momenta in the frame of reference of the X-line. The reconnection rate was not further suppressed by the streaming populations, such that the reconnection rate follows the same scaling relation as in Equation (3.17) (*Tenfjord et al.* (2019), *Kolstø et al.* (2020b)).

3.2.4 Dayside O$^+$ Reconnection Study

This subsection gives an overview of preliminary results of an ongoing O$^+$ magnetopause reconnection study. The main objective of this study is to investigate the potential additional effects heavy ions introduce in dayside magnetopause reconnection.

The previously referenced simulations (*Tenfjord et al.* (2018), *Kolstø et al.* (2020a,b)) dedicated to studying the role and effects of oxygen ions in the reconnection process was designed to represent the case of magnetotail reconnection. In these simulations, the plasma species are symmetrically distributed across the current sheet (with the exception of the simulation used in *Kolstø et al.* (2020a)). The plasma temperature profile as well as the magnetic field profile display a symmetric nature across the current sheet. As previously discussed, and seen in Table 3.1, the magnetopause dayside reconnection conditions differs greatly from the magnetotail. To investigate the effect of oxygen ions in dayside magnetopause reconnection two simulations were designed and executed: 1) Magnetopause reconnection in the presence of oxygen ions, and 2) Guide-field magnetopause reconnection in the presence of oxygen ions. The initial configurations are summarized in Figure 3.13.

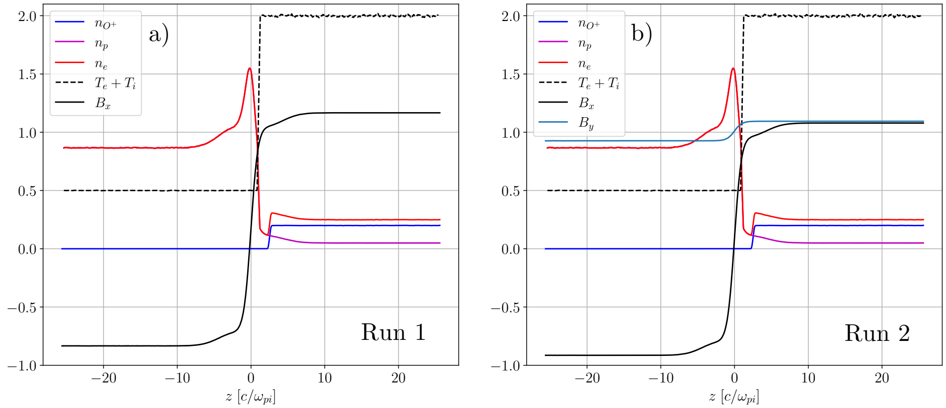

Figure 3.13: Initial configurations (in normalized units) of two simulations dedicated to study the effects of O$^+$ in dayside magnetopause reconnection. Panel a) shows the case of asymmetric reconnection without a guide field and panel b) shows the case in which the guide field is included.

The initial conditions models asymmetric configurations to mimic dayside magnetopause reconnection without a guide field ("run 1") and with a guide field ("run 2"). The magnetic field is given as a Harris sheet configuration (see e.g. *Hesse and Birn* (2004)), i.e. $B_x(z) = B_0 \tanh(z/\lambda) + a_1$, with the current sheet thickness $\lambda = 2d_p$. The factor a_1 is the symmetry offset chosen here to be $a_1 = 1/6$. The magnetic field is normalized to a typical value in the inflow region B_0, whereas the density is normalized to a typical density n_0 in the current layer. Furthermore, time and length are normalized to the ion gyroperiod Ω_p^{-1} and the ion inertial length d_p. The density profile is carefully chosen to preserve pressure balance in the z-direction across the current sheet such that

$$\left(n(T_i+T_e)+\frac{B^2}{2}\right)_U = \left(n(T_i+T_e)+\frac{B^2}{2}\right)_L$$

where the initial pressure is given as $p = 0.1 + 0.5(1 + a_1)^2 - 0.5B_x^2$, such that the initial density is given as

$$n^U = 0.5p$$
$$n^L = 2p$$

This implies that the total temperature $T = T_i + T_e$ has a variation between $T = 0.5$ (in units of $m_p v_A^2$) on the upper (magnetosheath) side, and $T = 2$ on the lower (magnetospheric) side. In addition, cold ($T_{O^+} = 0$) oxygen is added at a distance $z > 2.5d_p$. The coordinate system is as follows: x is the reconnection outflow direction, y is the direction of the initial current flow, whereas z is the reconnection inflow direction. For run 2, an guide field component of $B_y = 1$ is included. Further considerations regarding the use of an appropriate coordinate system are needed in investigating the effect of a guide field component in an asymmetric reconnecting system in 2.5D simulations. Depicted in Figure 3.6, is the asymptotic magnetic field values in a frame of reference rotated by an angle of α.

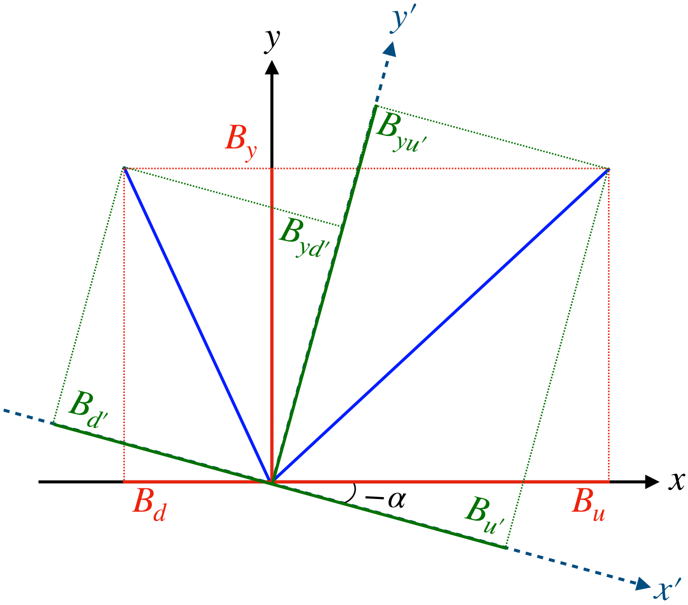

Figure 3.14: Illustration of the asymptotic magnetic field values in a coordinate system rotated by an angle α around the z-axis. The indices u and d refer to the asymptotic field values above and below the current sheet.

As the reconnection process proceeds, the X-line is preferentially oriented in such a manner that it bisects the asymptotic magnetic field values on each side of the current sheet (*Hesse et al.*, 2013). This corresponds exactly to the rotation of the X-line which maximizes the magnetic energy density to be available for reconnection, i.e.,

$$E_r = \psi B_{u'}^2 B_{d'}^2 \tag{3.18}$$

where ψ is a factor dependent on factors as density, total magnetic field strength etc., which are held constant during the time of investigation. Using Figure 3.14 to extract the asymptotic magnetic fields to optimize Equation (3.18), we readily obtain an equation for the angle for the coordinate transformation which optimizes the reconnection electric field component

$$\cot^2 \alpha_{\mathsf{max}} - 2\frac{B_d B_u - B_y^2}{B_y(B_u + B_d)}\cot \alpha_{\mathsf{max}} - 1 = 0$$

which amounts to $\approx 5^\circ$ from the chosen asymptotic field values. The result of this coordinate transformation is evidently seen in Figure 3.13b in which the field strength differences in the B_y component between the northern and the southern lobe has been altered from 1 to 1.1 and 0.9, respectively.

Behavior of O^+ in Magnetopause Reconnection

In Figure 3.15 we show the evolution of the oxygen density for both runs. The Hall fields for these simulations are shown in Figure 3.6c-f in section 3.1.2. The leftmost column of Figure 3.15 displays the asymmetric run without a guide field component. The onset of reconnection is initiated by an x-type perturbation which commences the inflow of plasma towards the current layer. As reconnection proceeds, the Hall electric field expands due to the increasingly decoupled motion of the ions and electrons. The large gyroperiod of the oxygen ions as compared to the characteristic time scale of the reconnection process (Ω_p) results in a demagnetized behavior of the oxygen ions. The oxygen ions situated in the lobe are picked up by E_z and become subject to collective acceleration towards the neutral line. This gives rise to the inclined density striations depicted in panel b in Figure 3.15, which are commonly referred to as an oxygen wave (see e.g. *Tenfjord et al.* (2018) and *Kolstø et al.* (2021)).

In panel c), at $\Omega_p t = 100$, the oxygen wave has continued to expand into the reconnection exhaust region while the oxygen ions that were ballistically accelerated through the current layer has now established a quasi-steady horizontal striation (at $z \approx -5$) which marks the outer edge of the oxygen's bounce orbit[9]. The stronger Hall electric field in the north lobe (as compared to the south lobe), causes a strong ballistic O^+ acceleration through the current layer which enables the oxygen ions to overcome the electric potential in the southern lobe. As a result of this, the oxygen ions is freely transported from the magnetosphere and into the magnetopause. This magnetosphere-magnetosheath transport is not evident in the presence of a guide field.

As we saw in Figure 3.6 in section 3.1.2, a guide field component will greatly alter the electric field configuration which is, ultimately, the controlling factor of the oxygen dynamics. In panel d-f, we see the evolution of the oxygen number density for the guide field run. In this case, the electric field signatures are asymmetric in the x-direction around the X-line. On the left side of the X-line, the downward propagation of the oxygen ions is impeded by the positively z-directed electric E_z. This results in a high density localized band which encumbers the transport of oxygen ions into the magnetosheath. Similar signatures have been reported in a study by *Markidis et al.* (2011). To the right of the X-line, a negatively electric field persist enabling a small fraction of the O^+ to be transported into the exhaust region. As compared to the case

---

[9] The bounce orbit refers to the case where O^+ is ballistically accelerated through the neutral line, turned by the Lorentz force, and subsequently, continue its motion past the neutral line again.

without a guide field, only small amount of the oxygen ions are able to cross to the neutral line to escape the magnetosphere and enter the magnetosheath.

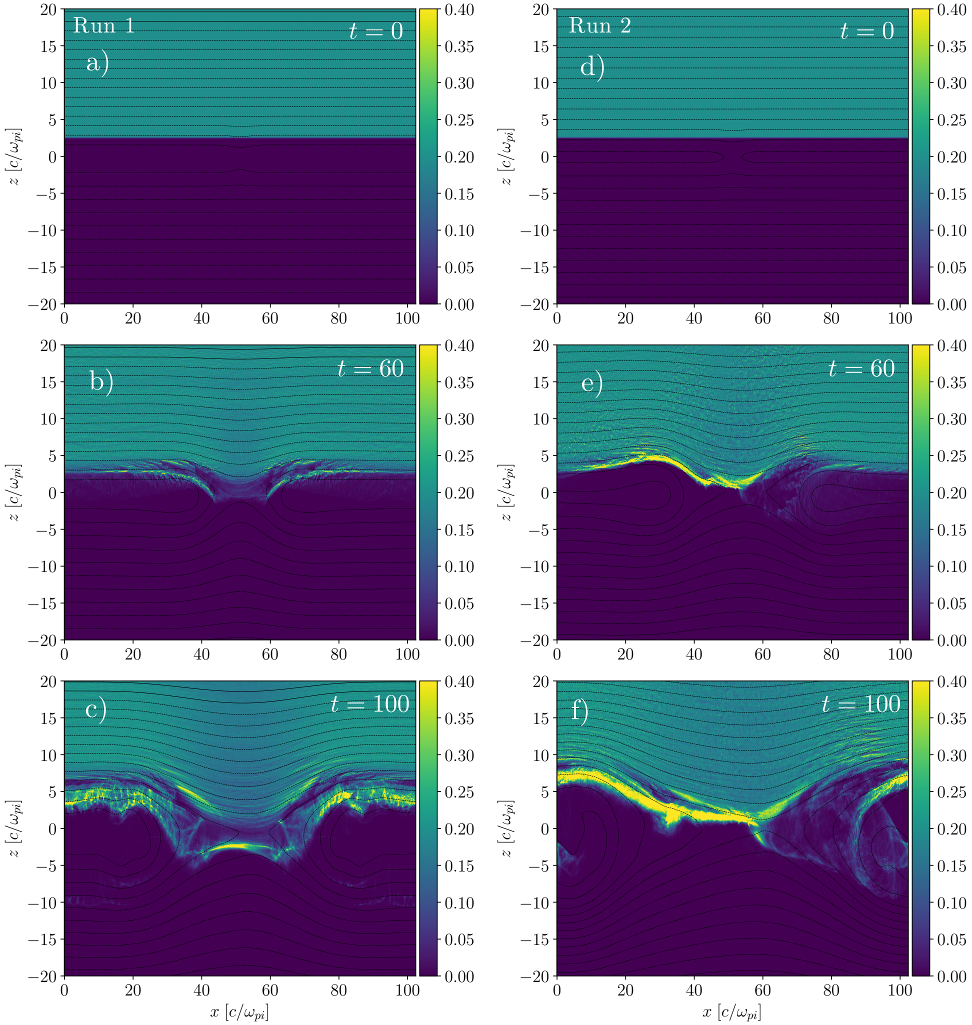

Figure 3.15: Evolution of the number density of the oxygen ions for 1) asymmetric reconnection, and 2) asymmetric + guide field reconnection.

Motion of the X-line

For run 1 we do not observe any significant displacement of the X-line. However, in run 2, where the guide field is introduced, the X-line exhibit a clear net motion towards positive values of x moving at a velocity of $\sim 0.1 v_A$. This is shown in Figure 3.16 in panel a and b. Furthermore, in the color map in panel b, we see the evolution of the oxygen number density (for a cut through the X-line along x), with the motion of the X-line. Here we see the asymmetrically (around the X-line) distributed density of O^+ as a result of the characteristic electric field signatures present in the guide field case. As reconnection proceeds an increasing amount of O^+ is transported into the reconnection region resulting in a pile-up of oxygen ions to the left of the X-line.

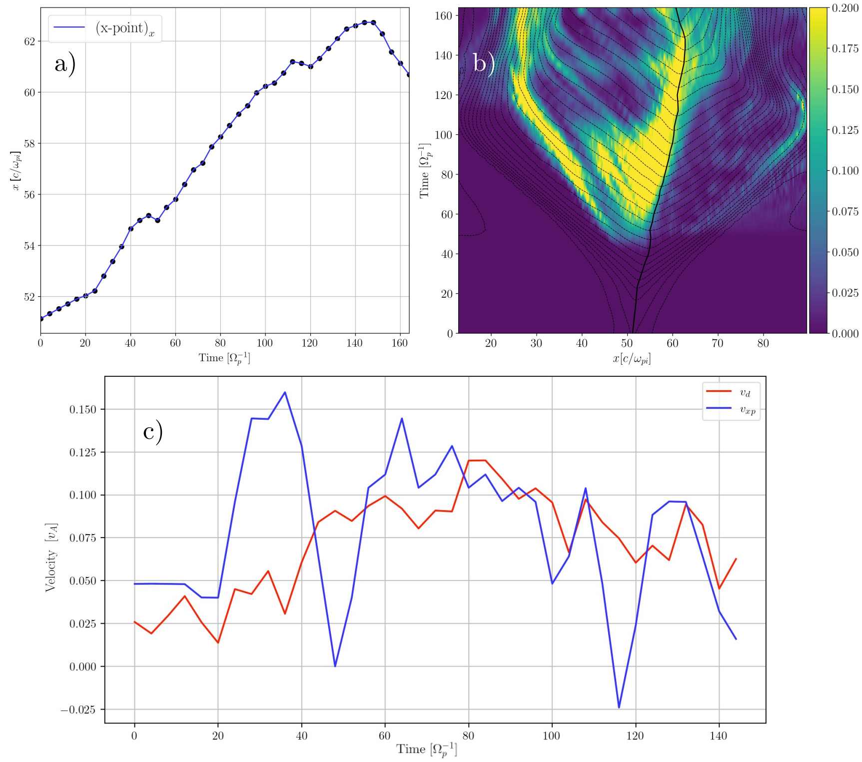

Figure 3.16: All Figures show data from Run 2. a) Displacement of the X-line. b) A cut through the X-line along x following how the oxygen ion density evolves as a function of time. The color map shows n_{O^+}, the dotted black line shows the contours of the magnetic vector potential A_y, defined by $\boldsymbol{B} = \nabla \boldsymbol{A} \times \hat{y} + B_y\hat{y}$, and the solid black line is the X-line location. c) Comparison of the X-line velocity v_{xp} (black) and the diamagnetic drift velocity v_d (red) obtained from Swisdak et al. (2003).

Previous studies conducted by *Kolstø et al.* (2020a,b) have shown that heavy ions, such as oxygen, may impart their momenta onto the reconnection region and induce a net motion of the X-line, regardless of its degree of magnetization. Therefore, we were led to investigate if the pile-up of O^+ might impede the flux transport by imposing its inertia on the leftmost exhaust which could result in such a rightward displacement of the X-line. Such an effect due to the oxygen ions was not found, and thus the X-line motion does not seem to be attributed to the O^+. The motion of the X-line is readily resolved when considering the presence of the guide field. The strong y-component of the guide field, in conjunction with a z-directed pressure gradient, gives rise to an x-directed diamagnetic propagation. Even though the diamagnetic drift is not a guiding center drift, i.e. it does not correspond to any actual net particle motions, it nevertheless advects the magnetic field (*Swisdak et al.*, 2003, 2010). In a study by *Swisdak et al.* (2003), the authors found that as a stability criterion in magnetopause reconnection, the X-line velocity v_{xp} matches that of the diamagnetic drift velocity v_d at the reversal region, e.g. $B_x = 0$, given by

$$v_d = \frac{T_e}{q_e L_{pe} B_y}$$

where $L_{pe}^{-1} \sim |\partial_z P_{zz}^e|/P_{zz}^e$, and the other quantities have their usual meaning. This has further been observationally confirmed in a study by *Phan et al.* (2013). In panel 3.16c we see the comparison between the diamagnetic drift velocity (red) and the X-line velocity (blue). Although there are some clear fluctuations during the fast phase of reconnection, the overall agreement is evident during the stable phase of reconnection (60-140Ω_p^{-1}). We thus conclude that the X-line motion is not induced by the oxygen ions.

Regarding the behavior of oxygen ions in dayside magnetopause reconnection, no additional kinetic effects induced by O^+, as compared to magnetotail reconnection (e.g. *Markidis et al.* (2011), *Tenfjord et al.* (2018), *Kolstø et al.* (2020a,b, 2021)), have been found in the investigation of this study.

Chapter 4

Probing Reconnection

The process of magnetic reconnection may occur in several environments ranging from man-made laboratories on Earth, the Magnetosphere, solar flares, and even X-ray flares in the pulsar wind nebula (*Hesse and Cassak*, 2020). It is rather natural for a magnetized plasma to exhibit a field reversal component at a boundary layer. One might therefore be led to think that as the process of reconnection can occur in such an abundance of cases that it be straightforward to investigate. Unfortunately, this is not the case. A major problem studying reconnection is that of its multiscale nature. As an example, the reconnection in the Earth's magnetosphere is governed by physics occurring at scales of the electron Larmor radius of 1-10 km. However, the direct impact of magnetic reconnection affects scales of the whole magnetosphere extending orders of 10^6 km.

Studying the process of magnetic reconnection in laboratory experiments imposes challenges related to resolving small-scale electron structures as the typical Larmor radius in such systems is approximately 0.5 mm (see *Yamada et al.* (2010)). To fully capture the large scale effects of reconnection, a coupling to the ions must be achieved. As the typical gyroradius of an ion in such a system is close to 1 m, it would require a controlled system with size on the order of 10-100m in which the electron physics are simultaneously resolved (*Hesse and Cassak*, 2020). Owing to the cost and logistics of such an experiment, it is rather likely that such a device will remain difficult to realize within the close future.

As opposed to the man-made laboratories, the large spatial extent of the Earth's magnetosphere makes it achievable for a direct investigation of the role of electron physics in magnetic reconnection. This is done using spacecraft performing high cadence measurements. As an example, a typical structure at the dayside magnetopause propagates at 100 km/s. If the electron gyroradius is around 10 km, the electron scale physics can be resolved with a measurement resolution of 100 ms (*Hesse and Cassak*, 2020). Up until the launch of the Magnetospheric Multiscale mission of 2015, no spacecraft missions had been able to resolve physics at the scale of the electron inertial length.

Figure 4.1: NASA's four Magnetospheric Multiscale, or MMS, satellites in a clean room at the Astrotech Space Operations facility in Titusville, Florida. Obtained from NASA/Smegelsky (2015).

Although the physical insight to any given phenomena is inherently based on empirical evidence, it has become clear that the advent of numerical simulations has become instrumental in uncovering mysteries in virtually any field of science. By employing numerical models and testing their validity against observations, one can determine the strength of the theory or to which degree it needs to be modified and improved. Furthermore, numerical simulations may greatly aid in the contextualization of spacecraft measurements which are limited only to a relative local (10-400 km) region of investigation. Earlier spacecraft missions regarded only point measurements per time, proving the differentiation between spatial and temporal phenomena difficult. The launch of constellation missions, such as THEMIS, Cluster, and MMS resolved the issue of distinguishing between spatial and temporal phenomena but only at limited scales depending on the spacecraft separation. Furthermore, to simultaneously resolve the physics occurring at both the ion and electron scales would require at least 7 spacecraft which are configured as two nested tetrahedrons (with one spacecraft shared between the two tetrahedrons). The usage of numerical simulations is unquestionably cheaper and enables us to study physics at all scales, at all times, and further investigate regions inaccessible to in situ experiments. In this chapter, we will give an overview of the techniques and tools used in this thesis to uncover the role and effect of O^+ in magnetic reconnection.

4.1 Nature as a laboratory; MMS

On the 12th of March, 2015, the NASA Magnetospheric Multiscale (MMS), a constellation of four spacecraft was launched into orbit and set out on a mission to investigate the process of magnetic reconnection in the boundary regions of Earth's magnetosphere, extending to the magnetopause, the bowshock, the solar wind, and the neutral sheet in the magnetotail. The primary scientific goal of the MMS mission, as stated by *Burch et al.* (2016), is to

> *understand the microphysics of magnetic reconnection by determining the kinetic processes occurring in the electron diffusion region that is responsible for collisionless magnetic reconnection, especially how reconnection is initiated.*

The multi-point data acquisition at an inter-spacecraft separation ranging from as low as ~ 7 km (*Holmes et al.* (2018)), to several hundred km, enables MMS to discern temporal variations from spatial gradients at both ion and electron scales. In addition to the high spatial resolution, MMS is able to perform measurements at unprecedented time scales. Resolving 3D electron distribution functions at every 30 ms (150 for ions for FPI) allows MMS to directly observe the microphysics enabling the violation of the frozen-in theorem allowing the process of reconnection to occur (*Pollock et al.*, 2016).

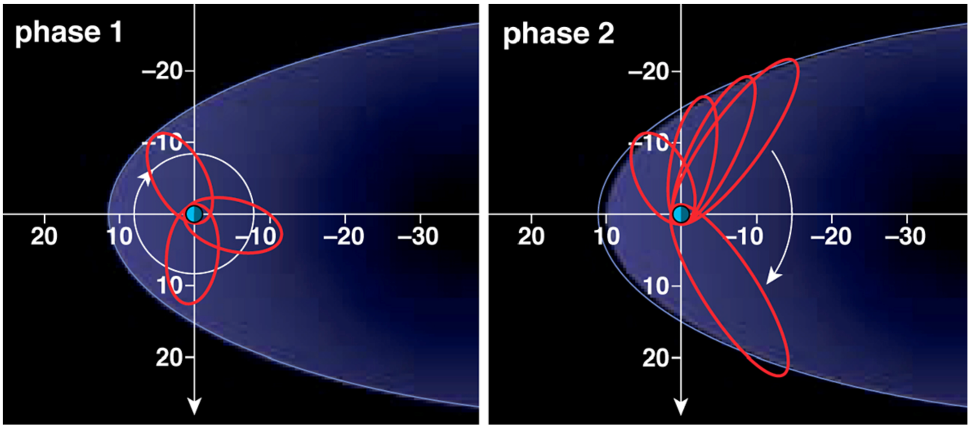

Figure 4.2: Illustration of the ecliptic plane of the MMS orbits for phase 1 and 2 covering the magnetopause and magnetotail, respectively. Obtained from Burch et al. (2016).

The prime mission orbits for the MMS mission are shown in Figure 4.2. As the mission length originally was planned for 2 years, MMS was to conduct 2 phases investigating reconnection at 1) the dayside magnetopause, and 2) at the magnetotail. In order to sample the most likely reconnection sites repeatedly, the apogee for phases 1 and 2, were $\sim 12\ R_E$ and $\sim 25\ R_E$, respectively. MMS has extended its operation and is in 2022 on its 7th phase. The four MMS spacecraft are maintained in a tetrahedral or pyramid-shaped configuration throughout the regions of interest. The tetrahedral formation enables the measurement of three spatial gradients of field and plasma parameters. Resolving the spatial gradients further allows for solving the Maxwell equations for quantities such as the current density $\frac{1}{\mu_0}\nabla \times \mathbf{B}$, the dB/dt through $\nabla \times \mathbf{E}$, and $\mathbf{E}$ contributions from $\nabla \cdot \mathbf{P}_e$ (*Henderson et al.*, 2006).

The high data rate sampling in combination with the measurements collection extending over large regions introduces major challenges of the storage and downlink capabilities. This issue motivated the development of a system which is able to rapidly analyze and evaluate the data in order to select the most promising intervals which satisfy the criteria for data to be downlinked. MMS collects a combined volume of $\sim$ 100 Gb per day (*Baker et al.*, 2016). However, only around 4% of that volume can be transmitted to the ground. In addition to nested automation, one employs Scientist-In-The-Loop (SITL) processes which are designed to downlink high sampling rates based on their inferred scientific importance. Typically, the high rate data, referred to as burst data, represents 2-4% of the time collection but corresponds to 74 % of the data. For the rest of the day, the burst data must be averaged down to either Slow Survey (50% of the time, $\sim$1.5% of data) or Fast Survey (50% of the time, $\sim$24% of data).

4.1.1 Instruments Overview

The MMS spacecraft extend 3.5m x 1.2m in width x height and at the time of launch, with propellant tanks fueled up, weighed 1360 kg. The instruments enabling pristine particle and fields measurements are introduced below. The MMS FIELDS suite provides measurements of the magnetic and electric field and is comprised of the following instruments.

Magnetic and Electric Field Measurements

- The **F**lux**G**ate **M**agnetometer (FGM): Enables a measurement of the magnetic field every $\sim$ 7.8 ms (burst mode) with an accuracy of $\sim$ 0.1 nT (DC field) (*Russell et al.*, 2016). For slow survey mode, the data rate is 16 Hz. The magnetic field measurements are made possible by ferromagnetic cores embedding two windings. An alternating current set up in the drive winding will induce a current in the sense-winding. In the case of a zero external magnetic field, the two windings cancel out. However, a current disparity between the two windings is realized in the presence of an external field. A net magnetic flux in the sense-winding can thus be measured as a voltage by virtue of Faraday's law.

- The **E**lectric field **D**ouble **P**robe (EDP): Measures the 3D electric field at a maximum frequency rate of 100 kHz (*Ergun et al.*, 2016; *Lindqvist et al.*, 2016). Comprised of Spin-plane Double Probes (SPD) and Axial Double Probes (ADP). SPD enables electric field measurements by estimating the potential differences between two spherical titanium-nitride electrodes with radii of 8 cm separated at a distance of 60 cm. SPD has 4 such probes enabling the measurement of two orthogonal E-field components in the rotation plane of MMS. The maximum sampling rate of SPD is 65kHz. As SPD provides field measurements in the spin plane, ADP measures the E-field along the rotation axis. Combining measurements from the SPD and ADP probes (separated by 30 m) enables us to estimate the 3D electric field.

- The **E**lectron **D**rift **I**strument (EDI): Provides measurements of the magnetic and electric field with a cadence of 10 samples/s.

- The **S**earch **C**oil **M**agnetometer (SCM): Measures magnetic field fluctuations in the frequency range of 1-6000 Hz (*Torbert et al.*, 2016).

Particle Measurements

- The **F**ast **P**lasma **I**nvestigation (FPI): At a time resolution of 30 ms and 150 ms for electrons and ions, respectively, the FPI instrument provides extraction of the 3D phase space density in the energy range of 10 eV-30 keV. (*Pollock et al.*, 2016). The high resolution is made possible by four dual 180-degree top hat spectrometers for electrons and four dual 180-degree (θ) top hat spectrometers for ions which are placed around the periphery of MMS. This approach by distributing many high-speed sensors around the perimeter, which covers the full azimuthal (ϕ) range, allows for much faster sampling rates as compared to the traditional spin-plane approach in which the sampling rate is dependent on the rotation period of the spacecraft. The final 3D phase space distribution for either species is then stitched together from the measurements of eight different spectrometers which covers the full zenith and azimuthal ranges (θ, ϕ).

- The **H**ot **P**lasma **C**omposition **A**nalyzer (HPCA): The HPCA instruments provides plasma composition-resolved 3D phase-space distributions for ions at energies ranging from 1 eV to 40 keV (*Young et al.*, 2016). As there is one HPCA device per MMS spacecraft, the time resolution is dependent on the rotation period. HPCA is, therefore, able to measure three-dimensional composition in one half of the spacecraft spin period, which nominally amounts to 10-15 seconds. HPCA is a time-of-flight (TOF) mass spectrometer that is designed to extract phase space density distributions for the four ion species H^+, He^+, He^{++}, and O^+, which shows a great impact on reconnecting phenomena.

- The **E**nergetic **P**article **D**etector (EDP): Suite including Energetic Ion Spectrometer (EIS) and Fly's Eye Energetic Particle Sensor (FEEPS) (*Mauk et al.*, 2016). EIS and FEEPS measure energy-angle distributions and ion composition between 20-500 keV at time resolutions 0.5-30 seconds depending on the energy range of investigation.

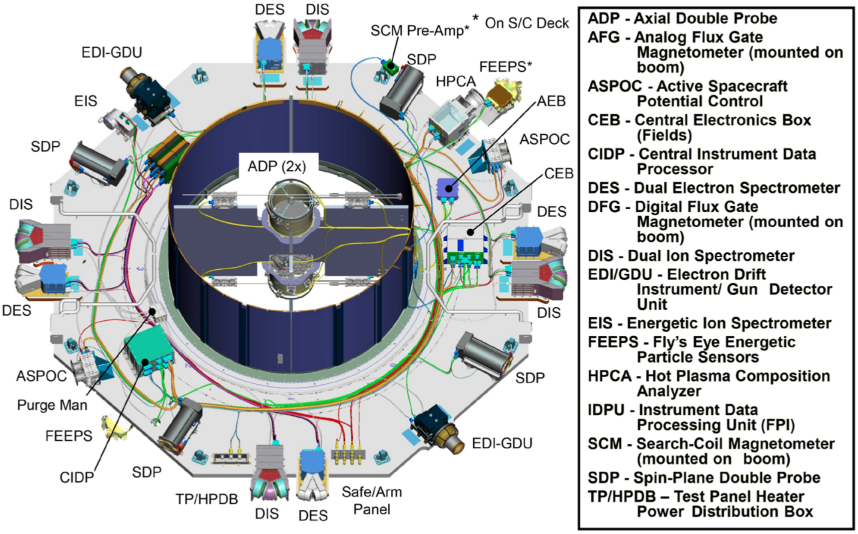

Figure 4.3: The MMS instrument deck layout. Adapted from Burch et al. (2016).

The MMS spacecraft also has the capability for dealing with surface potential changes due to exposure to sunlight. As briefly discussed in section 3.2.2, a spacecraft in sunlight will continuously emit photo-electrons which cause positive charge build-up on the spacecraft surface resulting in a positive voltage reaching up to several tens of volts. Therefore, low-energetic positive ions may fail to reach the spacecraft thus preventing direct detection. This may further interfere with electric field measurements (*Burch et al.*, 2016). MMS makes use of a device called Active Spacecraft Potential Control (ASPOC) which neutralizes the photo-electron current by generating beams of indium ions. This limits positive spacecraft potentials up to +4 V causing an improvement of the readings obtained from ADP, SDP, FPI, and HPCA (*Torkar et al.*, 2016).

4.2 Particle-In-Cell and Plasma Simulations

Advances in the understanding of the properties of a plasma have, traditionally, counted on experiments and observations on one hand, and analytic theory which is to match the observations on the other hand. A third approach emerged following the vast increase in computing power over the last 50 years, enabling high granularity numerical simulations of plasma phenomena (*Pritchett*, 2003). By utilizing a synergistic interplay between these approaches, one probes physics through experiments whose results are subsequently used to either prove or disprove theoretical expectations.

4.2.1 Simulating Interacting Particles

Choosing a suitable approach to simulate the plasma is paramount as the number of participating particles in the system introduces severe computational challenges. Imagine a system of N interacting charged particles which evolves according to the simple Newtonian mechanics presented in section 2.2. The particle position and velocity between two-time steps, discretized by Δt, are thus given by

$$\begin{aligned}\mathbf{x}_p^{new} &= \mathbf{x}_p^{old} + \mathbf{v}_p^{old}\Delta t\\ \mathbf{v}_p^{new} &= \mathbf{v}_p^{old} + \mathbf{F}_p\Delta t\end{aligned}$$

where $\mathbf{F}_p = \sum_{p'}^{N-1} F_{pp'}$ is the sum of the electromagnetic forces imposed on particle p by all the other $N-1$ particles in the system (see e.g. *Lapenta*, 2015). Once the total force on particle p has been found, the advances in velocity and, subsequently position can be computed and the process may be repeated. As each particle interacts with $N-1$ other particles, and each pair only are to be calculated once, the number of computations needed are thus $N(N-1)/2$. It is clear that even a small system of tenuous plasma, containing $\sim 10^{30}$ particles, makes this a highly unfeasible approach. Instead, a statistical approach is pursued in which the model is not composed by single particles interacting, but rather *macroparticles* (or computational particles) which represent a collection of many real particles that can be represented as a small piece of phase space.

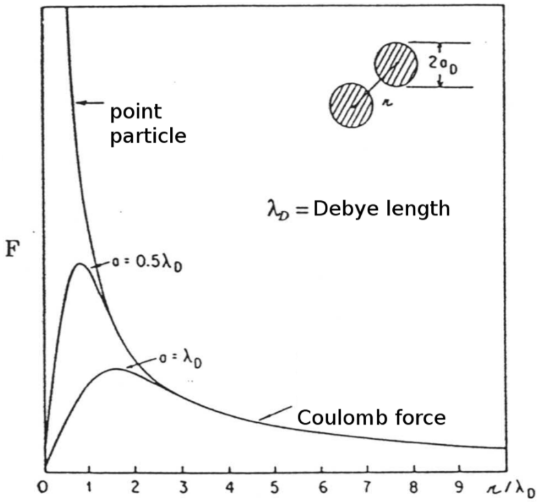

Figure 4.4: Coulomb force from a point particle and finite-sized macroparticles of different radii. From Dawson (1983).

The main advantage of introducing finite-sized macroparticles is that the Coulomb interaction is weaker compared to point particles (*Lapenta*, 2015). The Coulomb force for two point-like particles increases with decreasing distance reaching infinity as the separation approaches zero. The Coulomb force for macroparticles, however, behaves identically as point particles at a distance but is set to zero as the respective surfaces of the macroparticles overlap. This is shown in Figure 4.4 by *Dawson* (1983), which displays the Coulomb force for a point-like particle and two macroparticles of different radii. The Coulomb force of the macroparticle with the largest surface area weakens faster due to its larger spatial extent compared to the smaller one. Furthermore, another important aspect of the macroparticles is related to that of the plasma coupling parameter Γ introduced in section 2.1. Recall the definition

$$\Gamma = \frac{E_{th}}{E_{pot}} \tag{4.1}$$

in which Γ provides insight into how strongly coupled the plasma system is. A weakly coupled system, $\Gamma \gg 1$, has the characteristic feature that the mean-field acting on the particles are produced by the superposition of contributions by an abundance of particles. It is thus clear that by introducing finite-sized macroparticles which reduce the potential energy due to their properties (Figure 4.4), the system may remain weakly interacting for the same kinetic energy. This gives the advantageous consequence that the preferred plasma coupling parameter is achieved by fewer particles interacting more weakly. Electric field fluctuations in this system are thus correctly smooth as it is expected to be in a weakly coupled system (*Lapenta*, 2015).

From a computational perspective, the introduction of macroparticles is greatly favorable. The method of combining many real particles into clouds of macroparticles greatly reduces the number of interacting components in the system. As an example, consider a medium-sized system containing 10^7 macroparticles to be executed over 10^4

time steps. Assuming an evaluation of the force requires 10 arithmetic operations, the total number of operations amounts to 10^{18} (*Pritchett*, 2003). With a fast computing time of $\sim$ 10 GHz, the total time needed to complete the simulation is $\sim$ 3.2 years. Therefore, an additional technique must be introduced to make plasma simulations viable. In addition to the usage of macroparticles, a disruptive approach in which fields are discretized and interpolated to a grid was introduced. This greatly reduces the number of operations from $\mathcal{O}(N^2)$ to $\mathcal{O}(N\log N)$ (*Shalaby et al.*, 2017). The macroparticles are used to discretize the distribution function and move along characteristics of the Vlasov equation in phase space (*Lapenta et al.*, 2006). These are the fundamental features of the particle-in-cell (PIC) approach.

4.2.2 Particle-In-Cell Approach

Particle-In-Cell simulations enable state-of-art numerical modeling of plasmas in the framework of kinetic theory (*Evans and Harlow* (1957), *Buneman* (1959)), *Dawson* (1983), *Birdsall and Langdon* (2004), *Hesse et al.* (1999), *Markidis et al.* (2010), *Lapenta et al.* (2006)). In the PIC approach, macroparticles in a Lagrangian frame are traced in continuous phase space, whereas moments of the distribution function, i.e. n, $\mathbf{v}$, and fields $\mathbf{E}$ and $\mathbf{B}$ are calculated in grid points in the Eulerian frame (*Pritchett*, 2003). This stems from the idea that the particle trajectories are characteristics of the Vlasov equation (2.13) in phase space. Hence, f is constant along a particle orbit such that $\frac{d}{dt}f(\mathbf{x},\mathbf{v},t) = 0$, from Liouville's theorem. The general approach is straightforward. First, the particle positions and velocities are interpolated to the grid in order to calculate the corresponding charge and current densities $(\rho,\mathbf{J})$. Next, Maxwell's equations are solved by the use of the extracted ρ and $\mathbf{J}$ to calculate the self-consistent electromagnetic fields. The newly found $\mathbf{E}$ and $\mathbf{B}$ is then interpolated back to the particle locations in the grid where the acceleration due to the Lorentz force is calculated. The acceleration now completes the set of parameters needed to evolve the particles in time. The approach in the following derivation may readily be found in e.g. *Lapenta* (2015); *Markidis et al.* (2010); *Shalaby et al.* (2017).

Fundamentals

The particle-in-cell approach is dependent on the discretization of the distribution function. Under assumption that the distribution function f_s for a given species s is given by the sum of the distribution function of several macroparticles f_p,

$$f_s(\mathbf{x},\mathbf{v},t) = \sum_p f_p(\mathbf{x},\mathbf{v},t) \tag{4.2}$$

where the macroparticles are comprised of abundant real particles that exist close to each other in the phase space. As the macroparticles represent small elements of phase space, their finite size is realized by a shape function S which are dependent on the six phase-space coordinates $(\mathbf{x},\mathbf{v})$. The functional dependence is a tensor product of the shape function along with the respective coordinates in the phase space

$$f_p(\mathbf{x},\mathbf{v},t) = N_p S_{\mathbf{x}}(\mathbf{x}-\mathbf{x}_p(t)) S_{\mathbf{v}}(\mathbf{v}-\mathbf{v}_p(t)) \tag{4.3}$$

where N_p is the number of physical (or real) particles in the element of phase space which are represented by the macroparticle. The shape functions are to represent only a small region of the phase space, and hence they are quickly set to zero outside a small range. Furthermore, the convenient property in which its integral is unity is imposed

$$\int_{-\infty}^{\infty} S_\xi(\xi - \xi_p) d\xi = 1$$

in which ξ represents any coordinate of the phase space. Although not strictly needed, another convenient criteria is that of imposing symmetry, i.e. $S_\xi(\xi - \xi_p) = S_\xi(\xi_p - \xi)$. The standard choice of the shape function for the velocity coordinate is that of the Dirac delta function, i.e. $S_{\mathbf{v}}(\mathbf{v} - \mathbf{v}_p(t)) = \delta(\mathbf{v} - \mathbf{v}_p(t))$. This is motivated by the fact that physical particles in an element of phase space will remain close in phase space during the evolution if their velocity is the same. The shape function for the spatial components $S_{\mathbf{x}}$ are commonly described by orders of *b-spline* functions defined as (*Boor*, 1978)

$$b_0(\xi) = \begin{cases} 1 & if\ |\xi| < \frac{1}{2} \\ 0 & elsewhere \end{cases}, \quad b_l(\xi) = \int_{-\infty}^{\infty} d\xi' b_0(\xi - \xi') b_{l-1}(\xi') \tag{4.4}$$

in which the higher orders are obtained by successive integration. The different orders of the b-splines are shown in Figure 4.5, and follow the imposed criterion of symmetry and unitary integral.

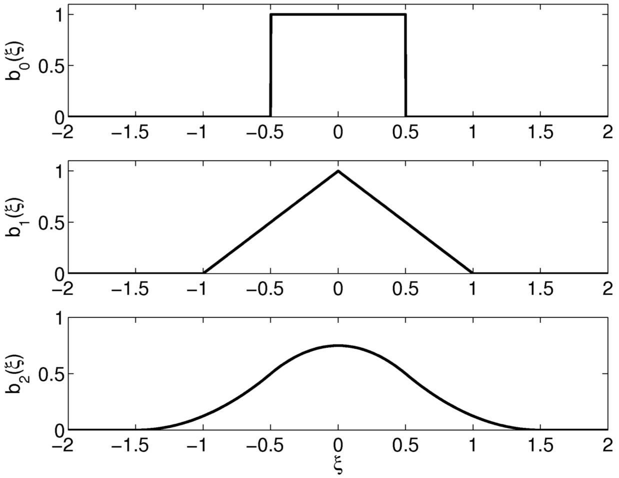

Figure 4.5: b-spline shape functions for different orders. Adapted from Lapenta (2015).

The spatial shape function may then be chosen to be represented by a given order of the b-spline function such that

$$S_{\mathbf{x}}(\mathbf{x} - \mathbf{x}_p(t)) = b_l \left(\frac{\mathbf{x} - \mathbf{x}_p(t)}{\Delta \mathbf{x}} \right)$$

where $\Delta \mathbf{x}$ is the grid spacing in the spatial directions. In this thesis, we make use of the 0^{th} order b-spline. This choice is typically referred to as Cloud-In-Cell as the macroparticle now takes the form of a uniform finite square in the $\mathbf{x}$-direction with an infinitesimal extent for the $\mathbf{v}$-components (*R W. Hockney*, 2021).

Dynamic Equations for the Macroparticles

Now that an expression for f_p has been obtained, the next step is to derive a set of dynamic equations governing the behavior of the macroparticles. By taking the moments of the Vlasov equation, Equation (2.13), with the phase space element f_p, Equation (4.3), we are able to arrive at a complete dynamic description. Note that the Vlasov equation is linear in terms of the full distribution function f_s, which is a superposition of each element of phase space f_p. Thus, if f_s satisfy the Vlasov equation, so will f_p. As an example, let us take the first order moment in $\mathbf{v}$, and integrate over both the spatial and velocity components, to obtain the equation-of-motion for the phase space element,

$$\iint \left(\mathbf{v}\frac{\partial f_p}{\partial t} + \mathbf{v}\mathbf{v}\cdot\nabla_{\mathbf{x}} f_p + \mathbf{v}\frac{q_s}{m_s}(\mathbf{E}+\mathbf{v}\times\mathbf{B})\cdot\nabla_{\mathbf{v}} f_p \right) d\mathbf{x}d\mathbf{v} = 0$$

where the first term simply gives $d(N_p\mathbf{v}_p)/dt$ and the second term computes to zero due the integration over $\mathbf{x}$, which amounts to evaluating f_p at the boundaries, i.e. $f_p(\pm\infty) = 0$. Here the electromagnetic fields are the total fields due to all elements. The third, and final term, gives, by integration by parts

$$-\int \frac{q_s}{m_s}(\mathbf{E}+\mathbf{v}\times\mathbf{B})d\mathbf{x}\int f_p d\mathbf{v} = \frac{q_s N_p}{m_s}(\mathbf{E}_p + \mathbf{v}_p\times\mathbf{B}_p)$$

which gives, combined with the first term, the familiar expression $\frac{d\mathbf{v}_p}{dt} = \frac{q_s}{m_s}(\mathbf{E}_p + \mathbf{v}_p \times \mathbf{B}_p)$. Note now that the electromagnetic fields $\mathbf{E}_p$ and $\mathbf{B}_p$ represent the average electric and magnetic fields acting on a macroparticle. By using the definition of f_p, Equation (4.3), we have

$$\mathbf{E}_p = \int \mathbf{E}(\mathbf{x})S_{\mathbf{x}}(\mathbf{x}-\mathbf{x}_p)d\mathbf{x}, \qquad \mathbf{B}_p = \int \mathbf{B}(\mathbf{x})S_{\mathbf{x}}(\mathbf{x}-\mathbf{x}_p)d\mathbf{x} \tag{4.5}$$

where the property of the shape function for the $\mathbf{v}$-components are imposed, i.e. $\int S_{\mathbf{v}}(\mathbf{v}-\mathbf{v}_p)d\mathbf{v} = 1$. The evolutionary equations for $\mathbf{x}_p$ and $\mathbf{v}_p$ for the macroparticles resemble the Newtonian mechanics as physical particles with the exception that the electromagnetic fields represent the average field acting over the domain of the macroparticle. By evaluating the 0^{th} and 1^{st} moments (in $\mathbf{x}$) we arrive at the final evolutionary equations

$$\frac{dN_p}{dt} = 0 \qquad \frac{d\mathbf{x}_p}{dt} = \mathbf{v}_p \qquad \frac{d\mathbf{v}_p}{dt} = \frac{q_s}{m_s}(\mathbf{E}_p + \mathbf{v}_p\times\mathbf{B}_p) \tag{4.6}$$

Once the dynamic behavior for the macroparticles has been established, we need a way to evolve the particle position and velocity in time based on the imposed Lorentz forces. Before time-discretizing the equations of motions along with Maxwell's equations, we introduce an eulerian grid which will greatly aid us in the computation. When the new locations of the macroparticles are found, the charge and fluxes are deposited onto the grid where the electromagnetic fields are calculated. The newly found electromagnetic fields are thus interpolated to the macroparticle location where the new Lorentz force is computed which enables the next location and velocities to be found. In order to realize this method, we need a means for the particle and grid to communicate with each other.

Grid-Particle Communication

The next step is to introduce the grid which will greatly reduce the computational cost. The grid enables the discretization of charge and current densities. Furthermore, the points correspond to the location where the electromagnetic fields are calculated. From the name of this method, *particle in the cell*, we need to know how the charge and fluxes are distributed onto the cell vertices from the given macroparticle within that cell. We further need a method to allow communication between the fields at the grid points $\mathbf{x}_i$ and the particle location $\mathbf{x}_p$. Figure 4.6a illustrates how the charges and fluxes are distributed. The charge and particle fluxes are distributed among the nodes according to weight factors w which are dependent on the fractional node-to-particle distance.

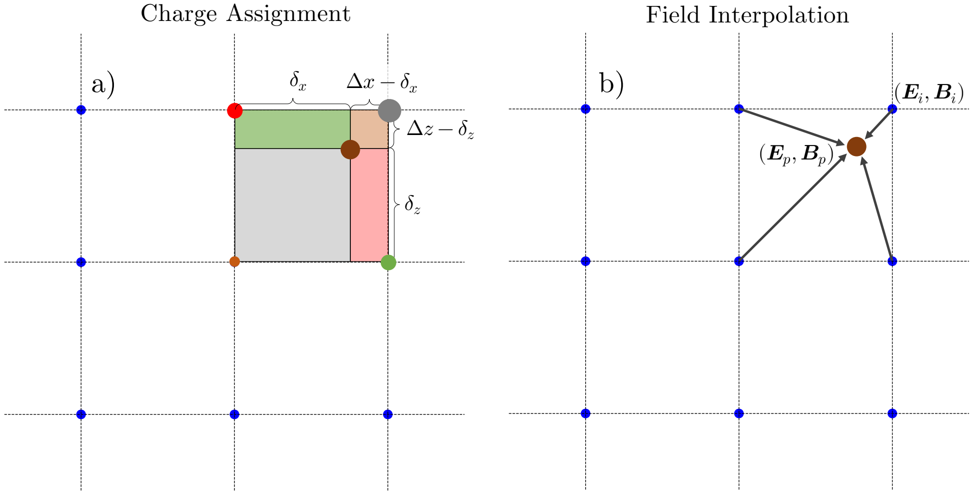

Figure 4.6: a) Illustration of how the charge is distributed among the grid points in the cell the particle is within. Hence the name of this approach: particle-in-cell. b) The second panel shows the field interpolation between the grid and the macroparticle.

Depicted in Figure 4.6a, the macroparticle is closest to the grey node and hence the largest fraction of the charge is deposited on to this node with a weighting factor $w_{\text{green}} = \delta_x \delta_z$. On the contrary, the distance from the macroparticle to the brown node is largest and thus this node receives the smallest fraction of the charge and current density with a weighting factor $w_{\text{brown}} = (\Delta z - \delta_z)(\Delta x - \delta_x)$. The charge deposited on to a specific node is then given by $\rho_{j,k} = q_p w_{j,k}/(\Delta x \Delta z)$, where j,k are grid indices.

The communication of the fields between the particle and the grid location, and vice versa, is made possible by the interpolation function

$$W(\mathbf{x}_i - \mathbf{x}_p) = \int_{-\infty}^{\infty} S(\mathbf{x}_i - \mathbf{x}_p) b_0 \left(\frac{\mathbf{x}_p - \mathbf{x}_i}{\Delta \mathbf{x}} \right) d\mathbf{x} = \frac{b_1(\mathbf{x}_i - \mathbf{x}_p)}{\Delta \mathbf{x}}$$

where the definition of the b-splines, Equation (4.4), is used. The indices i and p correspond to the cell center (vertices at $\mathbf{x}_{i\pm1/2}$) and particle location, respectively. The moments of the macroparticle distribution function, i.e. the charge and current densities (same goes for the pressure tensor), onto the grid may easily be written by the use of the interpolation function in the following manner

$$\rho_i^n = \sum_s^{n_s}\sum_p^{N_s} q_s W(\mathbf{x}_i - \mathbf{x}_p^n) \qquad \mathbf{J}_i^n = \sum_s^{n_s}\sum_p^{N_s} q_s v_p^n W(\mathbf{x}_i - \mathbf{x}_p^n) \tag{4.7}$$

where the sum denotes iteration over N_s macroparticles, with a total charge of $q_s = q_p N_p$, within a total number of n_s different species within the system. The interpolation function enables us to express the electromagnetic fields acting on the macroparticles, Equation (4.8), in a more convenient manner

$$\mathbf{E}_p = \sum_i \mathbf{E}_i W(\mathbf{x}_i - \mathbf{x}_p) \qquad \mathbf{B}_p = \sum_i \mathbf{B}_i W(\mathbf{x}_i - \mathbf{x}_p) \tag{4.8}$$

This is illustrated in Figure 4.6b. As we now have established the necessary tools to allow for information exchange between the macroparticle location and the grid points,

Push the Particles

There are essentially two schemes in which the governing parameters can be advanced; i.e. the *explicit* and *implicit* integration. As stated above, the equations of motion are dependent on fields acting on the particle, and, furthermore, the fields are dependent on the moments extracted from the particles. In the explicit scheme (see e.g. *Birdsall and Langdon* (2004); *R W. Hockney* (2021)), the evolution of the particle position and velocity are solely dependent on the fields evaluated from the previous time step. Furthermore, the updated fields also only need the sources computed from the previous time step. Thus, one needs only the information which is already easily accessible. The explicit scheme is favorable for its simplicity and computational speed but is subject to stability constraints (i.e. $c\Delta t/|\Delta\mathbf{x}| < 1$, $\omega_{pe}\Delta t < 2$, and $|\Delta\mathbf{x}| < \lambda_D$) in the investigation of large scale phenomena and slow occurring processes (*Birdsall and Langdon*, 2004; *Brackbill and Forslund*, 1982; *Markidis et al.*, 2010).

The implicit integration scheme (e.g. (*Brackbill and Forslund*, 1982; *Hesse et al.*, 1999; *Langdon*, 1985; *Lapenta et al.*, 2006; *Markidis et al.*, 2010; *Mason*, 1983)) was introduced to avoid severe stability constraints in the investigation of multi-scale processes. Implicit formulations of PIC algorithms exhibit strong conservation properties, up to numerical round-off errors, and are not subject to time-step limitations (*Kube et al.*, 2021). The implicit PIC method has also been shown to be linearly stable and is further not subject to the stability constraints imposed on the explicit scheme (*Brackbill and Forslund*, 1982). Additionally, the implicit approach is able to provide an accurate estimation of the system evolution when the displacement of the macroparticle per time is smaller than the grid spacing, i.e. $\mathbf{v}_{th}\Delta t/|\Delta\mathbf{x}| = \lambda_D\omega_{pe}/|\Delta\mathbf{x}|$ (*Brackbill and Forslund*, 1985). In the implicit method, the source terms that go into Maxwell's equations are computed at a future time. The challenge of solving the implicit scheme lies in the dependencies of the computation of the fields and particle momenta: The new particle position and velocity are dependent on the future values of the fields, and the computation of the field is further dependent on the future particle moments. As opposed to the explicit scheme, which follows a clear 4-step computational cycle, the implicit scheme must instead solve all the particle and field equations simultaneously. Through clever algebraic manipulations, we can restore the explicit feature of once-through calculation per Δt. This removes computationally heavy iterative processes in which particles are pushed several times per cycle. In this thesis, the implicit particle integration scheme is chosen, and not a full implicit PIC method. The current density $\mathbf{J}$ and charge density ρ are not predicted in the future per each computational cycle. The full scope of this technique is introduced in this section.

The equations of motion, Equation (4.6), may be time-discretized in the following manner

$$\mathbf{x}_p^{n+1} = \mathbf{x}_p^n + \mathbf{v}_p^{n+\alpha}\Delta t \tag{4.9}$$

$$\mathbf{v}_p^{n+1} = \mathbf{v}_p^n + \frac{q_p\Delta t}{m_s}\left(\mathbf{E}^{n+\theta}(\mathbf{x}_p^{n+\alpha}) + \mathbf{v}_p^{n+\alpha} \times \mathbf{B}^{n+\theta}(\mathbf{x}_p^{n+\alpha})\right) \tag{4.10}$$

where θ and α denotes the intermediate time steps between n and $n+1$ at which the arbitrary quantity Γ is taken, e.g. $\Gamma^{n+\theta} = (1-\theta)\Gamma^n + \theta\Gamma^{n+1}$, with $\theta, \alpha \in [\frac{1}{2}, 1]$. In this thesis, we chose $\alpha = 1/2$, but vary the choice of θ to have a slight forward bias in the range 0.55-0.65 to handle the case of instabilities. By algebraic manipulations (see e.g. *Lapenta et al.* (2006); *Vu and Brackbill* (1992)) we arrive at the exact expression for $\mathbf{v}_p^{n+1/2}$

$$\mathbf{v}_p^{n+1/2} = \Phi^n \cdot \left(\mathbf{v}_p^n + \kappa_s \mathbf{E}^{n+\theta}\left(\mathbf{x}_p^{n+1/2}\right)\right) \tag{4.11}$$

where $\kappa_s = q_p\Delta t/(2m_s)$ and the tensor Φ^n is introduced for simplification, which is given as,

$$\Phi^n = \frac{1}{1+(\kappa_s B^n)^2}\left(\mathbf{I} - \kappa_s \mathbf{I} \times \mathbf{B}^n + \kappa_s^2 \mathbf{B}^n\mathbf{B}^n\right)$$

where $\mathbf{I}$ is the identity matrix. The computation of the electric and magnetic fields are dependent on the mid-orbit position of the macroparticles, i.e. $\mathbf{x}^{n+1/2} = \frac{1}{2}(\mathbf{x}^{n+1} + \mathbf{x}^n)$ and hence Equation (4.11). When the evolution of the macroparticle has been established, we need a means of distributing the charge and current densities appropriately onto the grid.

Update the Fields

After ρ and $\mathbf{J}$ have properly been distributed onto the respective grid points, Maxwell's equations are used to calculate the electric and magnetic fields. The computational sequence per cycle must be carefully time-discretized in order to follow the implicit scheme. By initialization of the simulation, we have information of the particle velocities $\mathbf{v}_p$ at time n and $n+1/2$, whereas the particle position $\mathbf{x}_p$ and electromagnetic fields are known at $n+1/2$. The evolution after one computational cycle is summarized as follows

$$\begin{gathered}
\mathbf{x}_p^{n+1/2}, \rho^{n+1/2} \rightarrow \mathbf{x}_p^{n+3/2}, \rho^{n+3/2} \\
\mathbf{v}_p^n, \mathbf{J}^n \rightarrow \mathbf{v}_p^{n+1}, \mathbf{J}^{n+1} \\
\mathbf{B}^{n+1/2} \rightarrow \mathbf{B}^{n+3/2} \\
\mathbf{E}^{n+1/2} \rightarrow \mathbf{E}^{n+3/2}
\end{gathered}$$

To proceed with the field advancement, the next step is to time-discretize Maxwell's equations. We start off with the time-discretized Faraday's law which takes the following form after implicitly integrating the EM wave from Maxwell's equation (see Appendix A)

$$\begin{aligned}\left[1-(\theta c\Delta t)^2\nabla^2\right]\mathbf{B}^{n+3/2} &= \mathbf{B}^{n+1/2}-\Delta t\nabla\times\mathbf{E}^{n+1/2}\\ &\quad -\theta(c\Delta t)^2(\nabla^2\mathbf{B}^{n+1/2}(1-\theta)-\mu_0\nabla\times\mathbf{J}^n)\end{aligned} \tag{4.12}$$

where we have used that $\nabla\cdot\mathbf{B}=0$, such that $\nabla\times(\nabla\times\mathbf{B})=\nabla^2\mathbf{B}$. Equation (4.12) is a second order elliptic equation which needs some further handling,

$$\mathbf{B}^{n+3/2}=\mathbf{S}+(\theta c\Delta t)^2\nabla^2\mathbf{B}^{n+3/2}$$

where $\mathbf{S}$ is the right hand side of Equation (4.12). After the magnetic field at time $n+3/2$ has been found, we utilize the time discretized Ampère's law to advance the electric field

$$\mathbf{E}^{n+3/2}=\mathbf{E}^{n+1/2}+c^2\Delta t(\nabla\times(\mathbf{B}^{n+3/2}\theta+\mathbf{B}^{n+1/2}(1-\theta))-\mu_0\mathbf{J}^n) \tag{4.13}$$

After the electric field has been found we proceed with a cleaning step in order to ensure that Poisson's equation is fulfilled, i.e. $\nabla^2\phi=\nabla\cdot\mathbf{E}^{n+1}-\rho^n/\varepsilon_0$ to guarantee $\mathbf{E}^{n+1}$ is corrected which further implies charge density conservation. Where we used that $\varepsilon_0\nabla\cdot\mathbf{E}=\rho$ such that $\nabla\cdot\mathbf{E}^{n+1}-\rho^n/\varepsilon_0=0$ is fulfilled. By designing the grid according to the properties of the spatial operators, the process of calculating $\varepsilon_0\nabla\cdot\mathbf{E}=\rho$ and $\nabla\times\mathbf{E}=-\frac{\partial}{\partial t}\mathbf{B}$ becomes a straight forward task. In the PIC approach used in this thesis, the fields and velocities have a 3D extent, whereas the spatial gradients are only performed in the (x,z)-plane. Hence, the y-axis is into-plane such that $\frac{\partial}{\partial y}=0$. In Figure 4.7, we see the outline of the grid where the components of the electromagnetic fields ($\mathbf{E}$,$\mathbf{B}$) are computed. The red dots at the $x(i),z(j)$ locations are coincident with the grid point locations at which the charge and current densities, and fields are interpolated to.

Let us proceed with the computation of the electromagnetic fields using the grid as depicted in Figure 4.7. The components of the magnetic field at a specific location in the grid, denoted $\mathbf{B}_{i,j}$, is found by first computing the right hand side of the implicit Equation (4.12), and then proceeding with an finite elliptic solver to compute $\mathbf{B}_{i,j}^{n+3/2}$. Calculation of the right-hand side, $\mathbf{S}_{i,j}$, of Equation (4.12) gives

$$\begin{aligned}S_{x_{i,j}}^{n+3/2} &= B_{x_{i,j}}^{n+1/2}+\frac{\Delta t}{\Delta z}\left[(E_{y_{i,j+1}}^{n+1/2}-E_{y_{i,j}}^{n+1/2})-\theta c^2\Delta t(-J_{y_{i,j+1}}^{n}+J_{y_{i,j}}^{n})\right]\\ &\quad +(1-\theta)\theta(c\Delta t)^2\left[\frac{B_{x_{i+1,j}}^{n+1/2}-2B_{x_{i,j}}^{n+1/2}+B_{x_{i-1,j}}^{n+1/2}}{(\Delta x)^2}+\frac{B_{x_{i,j+1}}^{n+1/2}-2B_{x_{i,j}}^{n+1/2}+B_{x_{i,j-1}}^{n+1/2}}{(\Delta z)^2}\right]\end{aligned}$$

$$\begin{aligned}S_{y_{i,j}}^{n+3/2} &= B_{y_{i,j}}^{n+1/2}-\Delta t\left[\frac{E_{x_{i,j+1}}^{n+1/2}-E_{x_{i,j}}^{n+1/2}}{\Delta z}-\frac{E_{z_{i+1,j}}^{n+1/2}-E_{z_{i,j}}^{n+1/2}}{\Delta z}\right]\\ &\quad +\frac{\theta}{2}(c\Delta t)^2\left[\frac{J_{x_{i,j+1}}^{n}-J_{x_{i,j}}^{n}+J_{x_{i+1,j+1}}^{n}-J_{x_{i+1,j}}^{n}}{\Delta z}-\frac{-J_{z_{i,j+1}}^{n}-J_{z_{i,j}}^{n}+J_{z_{i+1,j+1}}^{n}+J_{z_{i+1,j}}^{n}}{\Delta x}\right]\\ &\quad +(1-\theta)\theta(c\Delta t)^2\left[\frac{B_{y_{i+1,j}}^{n+1/2}-2B_{y_{i,j}}^{n+1/2}+B_{y_{i-1,j}}^{n+1/2}}{(\Delta x)^2}+\frac{B_{y_{i,j+1}}^{n+1/2}-2B_{y_{i,j}}^{n+1/2}+B_{y_{i,j-1}}^{n+1/2}}{(\Delta z)^2}\right]\end{aligned}$$

$$S^{n+3/2}_{z_{i,j}} = B^{n+1/2}_{z_{i,j}} - \frac{\Delta t}{\Delta x}\left[(E^{n+1/2}_{y_{i,j+1}} - E^{n+1/2}_{y_{i,j}}) - \theta c^2 \Delta t (J^n_{y_{i,j+1}} + J^n_{y_{i,j}})\right]$$
$$+ (1-\theta)\theta(c\Delta t)^2 \left[\frac{B^{n+1/2}_{z_{i+1,j}} - 2B^{n+1/2}_{z_{i,j}} + B^{n+1/2}_{z_{i-1,j}}}{(\Delta x)^2} + \frac{B^{n+1/2}_{z_{i,j+1}} - 2B^{n+1/2}_{z_{i,j}} + B^{n+1/2}_{z_{i,j-1}}}{(\Delta z)^2}\right]$$

where the last term is the finite difference approximation of the Laplacian of **B**. Equation (4.12) is an elliptic partial differential equation that we can readily solve by

$$\mathbf{B}_{i,j} = \mathbf{S}_{i,j} + \frac{k_x(\mathbf{B}_{i+1,j} - \mathbf{B}_{i-1,j}) + k_z(\mathbf{B}_{i,j+1} - \mathbf{B}_{i,j-1})}{1 + 2k_x + 2k_z} \tag{4.14}$$

where $k_{\mathbf{x}} = (\theta c \Delta t / |\Delta \mathbf{x}|)^2$. As the magnetic field now has been found, we proceed with the computation of the electric fields.

$$E^{n+3/2}_{x_{i,j}} = E^{n+1/2}_{x_{i,j}} + c^2 \Delta t \left[\frac{-\theta(B^{n+3/2}_{y_{i,j}} - B^{n+3/2}_{y_{i,j-1}}) - (1-\theta)(B^{n+1/2}_{y_{i,j}} - B^{n+1/2}_{y_{i,j-1}})}{\Delta z} - J^{n+1}_{x_{i,j}}\right]$$

$$E^{n+3/2}_{y_{i,j}} = E^{n+1/2}_{y_{i,j}} + c^2 \Delta t \left[\frac{\theta(B^{n+3/2}_{x_{i,j}} - B^{n+3/2}_{x_{i,j-1}}) + (1-\theta)(B^{n+1/2}_{x_{i,j}} - B^{n+1/2}_{x_{i,j-1}})}{\Delta z}\right]$$
$$+ c^2 \Delta t \left[\frac{-\theta(B^{n+3/2}_{z_{i,j}} - B^{n+3/2}_{z_{i-1,j}}) - (1-\theta)(B^{n+1/2}_{z_{i,j}} - B^{n+1/2}_{z_{i-1,j}})}{\Delta x} - J^{n+1}_{y_{i,j}}\right]$$

$$E^{n+3/2}_{z_{i,j}} = E^{n+1/2}_{z_{i,j}} + c^2 \Delta t \left[\frac{\theta(B^{n+3/2}_{y_{i,j}} - B^{n+3/2}_{y_{i-1,j}}) + (1-\theta)(B^{n+1/2}_{y_{i,j}} - B^{n+1/2}_{y_{i-1,j}})}{\Delta x} - J^{n+1}_{z_{i,j}}\right]$$

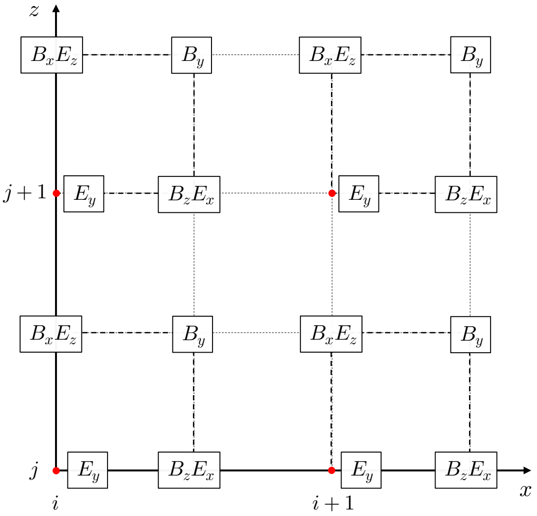

Figure 4.7: Outline of the grid showing where the components of **E** *and* **B** *are computed. The red dots correspond to the locations the densities and fluxes are interpolated to.*

The current densities $J^{n+1}_{x_{i,j}}$ and $J^{n+1}_{z_{i,j}}$ are defined on the spatial grid and must therefore be averaged in x and z, respectively. To complete the evolution of $\mathbf{E}$ and $\mathbf{B}$ we proceed with the cleaning of the electric field to preserve charge conservation by using Poisson's equation as described above. As the time-advanced electromagnetic fields $\mathbf{B}^{n+3/2}$ and $\mathbf{E}^{n+3/2}$ now have been found the next is to interpolate the fields onto the coordinate grid (red dots in Figure 4.7) so that the fields can easily be extracted at the particle locations $\mathbf{x}_p$ through Equation (4.8). When the updated fields are interpolated to the particle locations, updated velocities and positions are found, i.e. $\mathbf{v}_p^{n+3/2}$ and $\mathbf{x}_p^{n+3/2}$ through Equation (4.9) and (4.10). These updated positions and velocities are further used to compute and interpolate the charge and current density onto the grid by the use of Equation (4.7), and which are then finally used to calculate the electromagnetic field as by Equation (4.12) and (4.13), and the cycle repeats (see Figure 4.8).

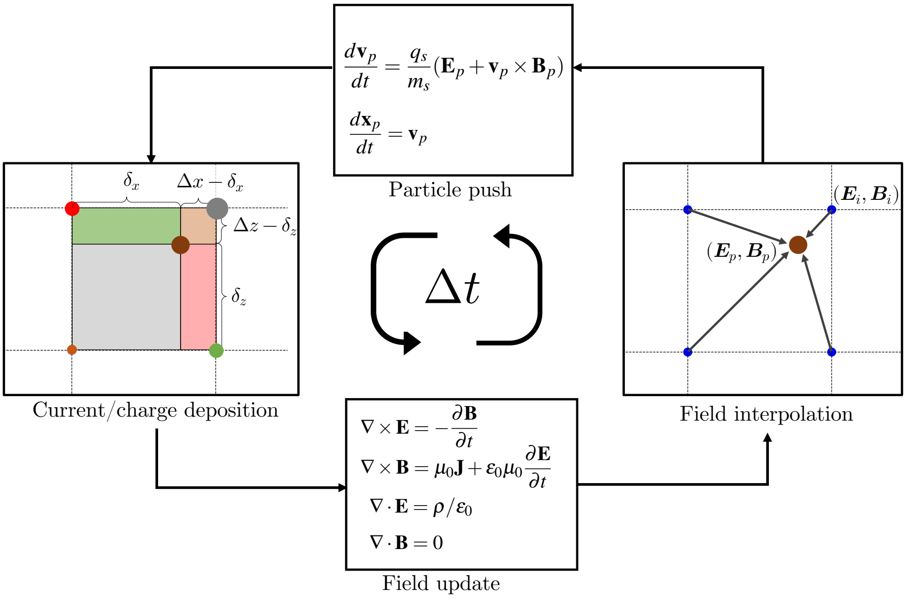

Figure 4.8: Illustration of the PIC-cycle.

Boundary Conditions

The PIC simulations in this thesis utilizes periodic boundary conditions at $x = x_{\min}$ and at $x = x_{\max}$. Any particles moving out of the x domain are simply reinserted at the opposite boundary. For example, if a particle moves to $x_{\max} + d$, then its x coordinate is changed to $x_{\min} + d$, with d being the the next cell position. Given n_x cells in the x-direction, quantities at cell index $i = 1$, and $i = 2$, are associated with quantities at index n_x and $n_x - 1$, respectively. Quantities from index 2 are added to quantities from index n_x, and then they are both assigned to index 2. At $z = z_{\min}$ and $z = z_{\max}$ particles are specularly reflected such that if a particle escapes the domain with velocity v_z, it is inserted back into the same location with velocity $-v_z$. For the electromagnetic fields, the boundary conditions for the normal direction for the electromagnetic fields are obtained by $\nabla \cdot \mathbf{B}_n$, and $\mathbf{E}_n = \nabla \cdot \sigma$, where σ now is the surface charge density. The tangential boundary conditions are further obtained through $\nabla \times \mathbf{B}_n = \mu_0 \mathbf{J}$, and the out-of-plane electric field E_y, is set to zero to preserve the magnetic flux in the simulation domain.

Chapter 5

Introduction to Papers

This chapter contains a brief summary of the three papers included in this thesis.

Paper I: Collisionless Magnetic Reconnection in an Asymmetric Oxygen Density Configuration

This paper investigates how the reconnection process is altered by an asymmetrically distributed O^+ component. As discussed in section 3.2.1, the presence of oxygen ions in the plasmaspheric lobe is enabled due to strong ionospheric outflows from the high-latitude ionosphere. At certain times, north-south asymmetries of ionospheric outflow may generate asymmetric O^+ inflow densities (*Barakat et al.*, 2015; *Glocer et al.*, 2020). Such asymmetries are generally expected at both the Earth's magnetopause (*Li et al.*, 2013) and in the magnetotail (*Glocer et al.*, 2020). A 2.5 PIC simulation is utilized in order to investigate this case. The oxygen ions are initially located at $|z| > 3d_i$, which in the simulation domain corresponds to the northern lobe. As the reconnection process proceeds, O^+ are slowly transported towards the current center and slightly encumber the magnetic flux mobility in the northern lobe. This gives rise to a disparity in the magnetic flux velocity between the two inflow regions which initiates a northward displacement of the reconnection region. The cold, inert oxygen ions are subject to demagnetization as their gyroperiod greatly exceeds the characteristic time scale of the reconnection process (Ω_p^{-1}). Thus, their dynamics are predominantly dictated by the electric field. When the oxygen ions fully enter the reconnection region, an asymmetry in the diffusion region arises. Due to the acceleration of oxygen by the Hall electric field, the dynamic oxygen pressure increases, and a reduction of the magnetic pressure arise to preserve the pressure balance. As a consequence, asymmetries in the Hall electric field are generated. As a result of the enhanced dynamic pressure, the oxygen ions no longer impose a drag on the transport of magnetic flux but instead contribute to an increase of the flux velocity causing a strong downward shift of the X-line. The asymmetrically distributed O^+ thus realize dynamics which enables current sheet flapping over time scales of $\sim 250\Omega_p^{-1}$. The demagnetized oxygen ions further reduce the reconnection rate, but not to the extent predicted by conventional mass-loading effects. A scaling relation, similar to that of *Tenfjord et al.* (2019), for the reconnection rate was developed which accounts for any spatial configuration of O^+ across the current sheet. The new scaling relation shows that the reconnection process proceeds twice as fast as predicted by mass-loading. The demagnetized O^+ enables a reduction in the reconnection rate by acting as an energy sink on the system. The rate reduction mechanism is realized by the fact that the oxygen ions extract energy from the fields that would otherwise have gone to the acceleration of the electrons and protons. It is further shown that the reconnection rate during the fast phase shows no dependency on the oxygen density.

Paper II: On the Impact of a Streaming Oxygen Population on Collisionless Magnetic Reconnection

The plasma in the inflow regions in magnetotail reconnection is highly dependent on the conditions imposed by ionospheric outflow. Oxygen ions flowing towards the nightside reconnection region have been shown to have a tailward streaming component due to their ionospheric origin (*Kistler et al.*, 2010). Statistical studies performed by *Liao et al.* (2015) found over 7500 tailward streaming oxygen events in the plasmaspheric lobes reaching energies of 5 keV (corresponding to 250 km/s). With this abundance of events, the scope of this study is to investigate how the reconnection process is affected by a streaming oxygen population. A 2.5D PIC simulation is utilized in which the oxygen ions has a streaming component of $v_x = 0.5v_A$, where x is the outflow direction and v_A is the Alfvén velocity obtained from the asymptotic magnetic field and the Harris peak density in the current sheet. *Tenfjord et al.* (2020) found that tailward streaming protons lead to a tailward motion of the reconnection region. Having oxygen ions as the streaming population, however, is considerably different as they do not exhibit a magnetized behavior throughout the times of investigation. In this paper, it is found that even though the oxygen ions remain demagnetized, i.e. not directly coupled to the magnetic field, they are still able to impose its momenta and alter the magnetic flux velocity which results in a tailward displacement of the reconnection region.

It is shown that a demagnetized species is able to alter the dynamics of the reconnection site long before the time of magnetization is realized. The coupling of O^+ to the magnetic flux occurs instead indirectly through the electrons by an electrostatic coupling. As the demagnetized oxygen ions enter the reconnection region, they are subject to collective acceleration by the Hall electric field. This results in localized density enhancements that propagate through the reconnection exhaust and are referred to as oxygen waves. Associated with these localized density enhancements is the buildup of electron density around the O^+ enhancements. These enhancements enable us to study how this electrostatic coupling between the electrons and oxygen ions takes place. The buildup of electrons introduce a strong pressure gradient which attempts to diffuse this electron density enhancement but are instead kept together by electric forces such that $\frac{\partial}{\partial x} P^e_{xx} \approx -en_eE_x$ is fulfilled. This electrostatic coupling forces the electrons to accompany the oxygen ions. In turn, this induced electron motion leads to the flux transport consistent with the X-line motion. It is further shown that this effect persists even for very low oxygen densities indicating that this is a continuous effect. The reconnection rate is evaluated and, compared to a non-streaming run, shows that a streaming population does not impose any further reduction of the reconnection rate. Compared to a non-streaming run (e.g. *Tenfjord et al.* (2018)), the streaming feature of the oxygen ions introduces distinct kinetic behavior which gives rise to involved velocity distribution functions.

Paper III: Magnetospheric Multiscale Observations of an Expanding Oxygen Wave in Magnetic Reconnection

In this paper, the goal is to tie together predictions obtained from the two previous simulational studies to investigate the behavior of oxygen ions in magnetotail reconnection by the use of observations from the MMS mission. On August 4^{th} 2017, during a time window of ~ 3 minutes, the MMS spacecraft entered a region in the magnetotail during active reconnection in the presence of oxygen ions. The spacecraft entered from the northern lobe, flew through the reconnection exhaust, and exited out to the lobe again. They remained on the north side of the current sheet throughout the time of the investigation. The observations display clear reconnection features. The LMN boundary normal coordinate system is used and is found through a minimum variance analysis on the $\mathbf{B}$-field. As the spacecraft moves toward the neutral sheet, MMS observes increasing B_M, coinciding with a prominent E_N which is identified as the Hall electric and magnetic fields, respectively. Furthermore, MMS observes strong Earthward flowing ion and electron jets reaching speeds up to 1000 km/s. The observations of the Hall fields coinciding with the ion and electron jets show a clear indication that the spacecraft passed through the reconnection exhaust.

The oxygen ions are decoupled from the motion of the lighter plasma species. Instead, they exhibit strong flows towards the neutral sheet $v_N^{O^+}$. The region of enhanced N-directed O^+ flows coincides with a region of low oxygen density which is referred to as the *density cavity*. Such density cavities are expected to be found as these regions represent the low-density wake after the collective E_N acceleration of O^+ which ultimately gives rise to the oxygen wave. In order to contextualize the observations, a 2.5D PIC simulation is used which is designed to represent a general reconnection process with an abundance of O^+ made to capture the additional effects introduced by heavier plasma species. To provide context to these observations, a simple, time-evolutionary, trajectory is constructed to search for a probable path of MMS1 with respect to the reconnection region. The strong match of the electromagnetic fields, as well as the bulk velocity and density moments between the simulation and observations, provides a confident contextualization of the MMS data. Along the inferred MMS trajectory, oxygen velocity distribution functions is extracted at designated locations which further displays a remarkable agreement. The remarkable match between observations and simulations suggest strongly that the features in the observations are, in fact, signatures of an oxygen wave.

Chapter 6

Conclusions and Future Prospect

6.1 Conclusions

The goal of this thesis has been to investigate the role and effect of heavier plasma species such as oxygen ions in magnetic reconnection. The evolution of the reconnection process is known to be highly dependent on the plasma composition, both in terms of species and quantity, and the field configuration. As lighter plasma species, such as electrons and protons, have a much higher gyrofrequency (and smaller gyroradii) as compared to the heavier species, they are able to respond much faster to any spatial or temporal variations in the magnetic field. They are thus much stronger coupled to the magnetic field than heavier ions are. Heavier ions, however, such as O^+, exhibit a much lower gyrofrequency (and larger gyroradii) which inhibits them to respond to any magnetic field variations occurring at small spatial and temporal scales. Even though oxygen ions are not as coupled to the magnetic flux tubes, as the lighter species, it is shown as a result of this thesis that they are still able to alter both the large and small scale dynamics of the reconnecting system. This is seen in Paper I, which presents how the demagnetized oxygen ions, which is asymmetrically distributed across the neutral line, introduce larger (separatrices) and smaller (diffusion) scale changes to the z-directed electric field (from the lobes towards the neutral line). The strong asymmetries of E_z, imposed by the oxygen ions, persists 5-10 d_i from the neutral line as well as in the diffusion region which further shows how the oxygen ions impact the dynamics of the lighter species.

In generating the asymmetries in the Hall electric field, the oxygen ions also induce a z-directed displacement of the X-line. This further demonstrates the oxygen's ability to impose changes to the reconnection region. Furthermore, Paper I expands on the work of *Tenfjord et al.* (2019) to investigate asymmetric O^+ systems. The scaling relation introduced in Paper I shows that the reconnection rate is not dependent on the density configuration, but rather on the total oxygen content in the reconnecting system. This new scaling law further provides a correction to the traditional Alfvèn scaling (or mass-loading) in which the heavier ions are treated as a magnetized species. Under certain conditions, scaling the reconnection rate through traditional mass-loading effects may be off by a factor of two! As the evolution of the geomagnetic environment is highly dependent on the reconnection process, such rate changes imposed by heavier ions are important considerations in understanding the large-scale magnetospheric dynamics.

In Paper II, it is shown that a tailward streaming demagnetized species may still be able to impart their momenta to the flux tubes which in turn causes a displacement of the reconnection region as a whole. As the O^+ is not magnetized, this momentum transfer is realized by an indirect coupling between the oxygen ions and the magnetic flux through the electrons. It is found that the induced motion of the X-line corresponds to the center-of-mass velocity of the plasma constituents. Thus, due to their high mass, the O^+ may give rise to a significant displacement of the reconnection region even if the oxygen ions represent only a fraction of the proton density.

In Paper III, the goal was to search for proposed oxygen dynamics in nature. A clear signature from the theoretical predictions that should be observable in nature is that of the oxygen waves. These are quasi-steady structures that extend over several ion inertial lengths and are a direct consequence of their large-scale dynamics. By utilizing NASA's Magnetospheric Multiscale mission this thesis further present the first in situ observation of this exact phenomenon. The kinetic behavior enabling the O^+ to produce such oxygen waves is attributed to their relatively large demagnetization scales, with respect to the lighter plasma species. This relative large-scale decoupling from $\mathbf{B}$ is also the exact same kinetic behavior which enables the generation of the other discussed effects such as the E_z asymmetries, X-line motion, and a reconnection rate that proceeds faster than the previously predicted mass-loading reduction. These MMS observations are therefore a clear indication that the theoretical predictions made in this thesis might be aligned with the physical nature of the magnetosphere and elsewhere in the universe where the reconnection process is subject to heavier ions.

6.2 Future Prospects

This thesis was conducted with the following 3-step approach: 1) Numerical simulations are tailored on the basis of previous observations of the presence of O^+ in the magnetotail. 2) Based on the simulations, gain a detailed theoretical description of the behavior of O^+ in magnetotail reconnection. And finally, 3) search for those predicted signatures out in nature by the use of in situ spacecraft observations. A total of nine 2.5D PIC simulations have been used as a part of this thesis, of which six have been designed and executed by the author.

Two of these simulations were designed to investigate the effects of oxygen ions in magnetopause reconnection where the conditions are substantially different from the magnetotail. A natural next step would be to collect a large set of in situ observations of reconnection at the magnetopause with the presence of O^+ to examine if there are additional effects not predicted by the simulations. Although many theoretical conclusions have been reached regarding the role and effect of heavy ions in magnetic reconnection (many of which were realized in this thesis), observational studies of heavier ions in reconnection are still highly underrepresented in the scientific literature. Additional in situ observations, e.g. the MMS constellation both in the magnetopause and in the magnetotail, will further provide useful in strengthening the bridge between numerical simulations and spacecraft observations.

In terms of further simulation studies, an advantageous approach would be an embedded PIC simulation in which the large-scale implications of heavier ions in the reconnection process could be investigated. In such a simulation, the demagnetization scales could further be studied enabling us to thoroughly understand under which conditions heavier ions show the greatest impact on the reconnection process. Furthermore, the usage of Global hybrid-Vlasov simulations, such as the Vlasiator (*von Alfthan et al.*, 2014), may provide further insight by resolving the O^+ dynamics for systems extending from the bow shock to several 10s of R_E past an active magnetotail reconnection region.

Bibliography

Alfvén, H. (1942), Existence of Electromagnetic-Hydrodynamic Waves - Nature, *Nature*, *150*(3805), 405–406, doi:10.1038/150405d0. 2.4

Alm, L., M. André, A. Vaivads, Y. V. Khotyaintsev, R. B. Torbert, J. L. Burch, R. E. Ergun, P.-A. Lindqvist, C. T. Russell, B. L. Giles, and B. H. Mauk (2018), Magnetotail Hall Physics in the Presence of Cold Ions, *Geophys. Res. Lett.*, *45*(20), 10,941–10,950, doi:10.1029/2018GL079857. 3.2.2

Alm, L., M. André, D. B. Graham, Y. V. Khotyaintsev, A. Vaivads, Charles. R. Chappell, J. Dargent, S. A. Fuselier, S. Haaland, B. Lavraud, W. Li, P. Tenfjord, S. Toledo-Redondo, and S. K. Vines (2019), MMS Observations of Multiscale Hall Physics in the Magnetotail, *Geophys. Res. Lett.*, *46*(17-18), 10,230–10,239, doi:10.1029/2019GL084137. 3.2.2

André, M., and C. M. Cully (2012), Low-energy ions: A previously hidden solar system particle population, *Geophys. Res. Lett.*, *39*(3), doi:10.1029/2011GL050242. 3.2, 3.2.2, 3.2.3

André, M., and A. Yau (1997), Theories and Observations of Ion Energization and Outflow in the High Latitude Magnetosphere, *Space Sci. Rev.*, *80*(1), 27–48, doi:10.1023/A:1004921619885. 3.2.1

André, M., K. Li, and A. I. Eriksson (2015), Outflow of low-energy ions and the solar cycle, *J. Geophys. Res. Space Phys.*, *120*(2), 1072–1085, doi:10.1002/2014JA020714. 3.2.3

André, M., W. Li, S. Toledo-Redondo, Yu. V. Khotyaintsev, A. Vaivads, D. B. Graham, C. Norgren, J. Burch, P.-A. Lindqvist, G. Marklund, R. Ergun, R. Torbert, W. Magnes, C. T. Russell, B. Giles, T. E. Moore, M. O. Chandler, C. Pollock, D. T. Young, L. A. Avanov, J. C. Dorelli, D. J. Gershman, W. R. Paterson, B. Lavraud, and Y. Saito (2016), Magnetic reconnection and modification of the Hall physics due to cold ions at the magnetopause, *Geophys. Res. Lett.*, *43*(13), 6705–6712, doi:10.1002/2016GL069665. 3.2

Antiochos, S. K., C. R. DeVore, and J. A. Klimchuk (1998), A Model for Solar Coronal Mass Ejections, *arXiv*, doi:10.1086/306563. 1, 3

Axford, W. I. (1968), The polar wind and the terrestrial helium budget, *J. Geophys. Res.*, *73*(21), 6855–6859, doi:10.1029/JA073i021p06855. 3.2.1

Baker, D. N., E. W. Hones, D. T. Young, and J. Birn (1982), The possible role of ionospheric oxygen in the initiation and development of plasma sheet instabilities, *Geophys. Res. Lett.*, *9*(12), 1337–1340, doi:10.1029/GL009i012p01337. 3.2

Baker, D. N., L. Riesberg, C. K. Pankratz, R. S. Panneton, B. L. Giles, F. D. Wilder, and R. E. Ergun (2016), Magnetospheric Multiscale Instrument Suite Operations and Data System, *Space Sci. Rev.*, *199*(1), 545–575, doi:10.1007/s11214-014-0128-5. 4.1

Banks, P. M., and T. E. Holzer (1968), The polar wind, *J. Geophys. Res.*, *73*(21), 6846–6854, doi:10.1029/JA073i021p06846. 3.2.1

Barakat, A. R., J. V. Eccles, and R. W. Schunk (2015), Effects of geographic-geomagnetic pole offset on ionospheric outflow: Can the ionosphere wag the magnetospheric tail?, *Geophys. Res. Lett.*, *42*(20), 8288–8293, doi:10.1002/2015GL065736. 5

Baty, H., T. G. Forbes, and E. R. Priest (2009), Petschek reconnection with a nonlocalized resistivity, *Phys. Plasma*, *16*(1), 012,102, doi:10.1063/1.3062833. 3.1.1

Baty, H., T. G. Forbes, and E. R. Priest (2014), The formation and stability of Petschek reconnection, *Phys. Plasma*, *21*(11), 112,111, doi:10.1063/1.4901918. 5

Baumjohann, W., and R. A. Treumann (1996), *Basic Space Plasma Physics*, World Scientific Publishing Company, London, England, UK, doi:10.1142/p015. 2, 2.1, 2.1, 3.1.1

Baumjohann, W., G. Paschmann, and C. A. Cattell (1989), Average plasma properties in the central plasma sheet, *J. Geophys. Res. Space Phys.*, *94*(A6), 6597–6606, doi:10.1029/JA094iA06p06597. 3.2.2

Birdsall, C. K., and A. B. Langdon (2004), *Plasma Physics via Computer Simulation*, CRC Press, Boca Raton, FL, USA. 4.2.2, 4.2.2

Boor, C. D. (1978), A Practical Guide to Splines, *undefined*. 4.2.2

Borovsky, J. E., and M. H. Denton (2006), Effect of plasmaspheric drainage plumes on solar-wind/magnetosphere coupling, *Geophys. Res. Lett.*, *33*(20), doi:10.1029/2006GL026519. 3.2

Bouhram, M., B. Klecker, W. Miyake, H. Rème, J.-A. Sauvaud, M. Malingre, L. Kistler, and A. Blăgău (2004), On the altitude dependence of transversely heated O+ distributions in the cusp/cleft, *Ann. Geophys.*, *22*(5), 1787–1798, doi:10.5194/angeo-22-1787-2004. 3.2.3

Brackbill, J. U., and D. W. Forslund (1982), An implicit method for electromagnetic plasma simulation in two dimensions, *J. Comput. Phys.*, *46*(2), 271–308, doi:10.1016/0021-9991(82)90016-X. 4.2.2

Brackbill, J. U., and D. W. Forslund (1985), Simulation of Low-Frequency, Electromagnetic Phenomena in Plasmas, in *Multiple Time Scales*, pp. 271–310, Academic Press, Cambridge, MA, USA, doi:10.1016/B978-0-12-123420-1.50014-8. 4.2.2

Buneman, O. (1959), Dissipation of Currents in Ionized Media, *Phys. Rev.*, *115*(3), 503–517, doi:10.1103/PhysRev.115.503. 4.2.2

Burch, J. L., and T. D. Phan (2016), Magnetic reconnection at the dayside magnetopause: Advances with MMS, *Geophys. Res. Lett.*, *43*(16), 8327–8338, doi:10.1002/2016GL069787. 3, 3.3

Burch, J. L., T. E. Moore, R. B. Torbert, and B. L. Giles (2016), Magnetospheric Multiscale Overview and Science Objectives, *Space Sci. Rev.*, *199*(1), 5–21, doi:10.1007/s11214-015-0164-9. 4.1, 4.2, 4.3, 4.1.1

Case, N. (2014), Solar Wind-Magnetosphere Interactions: A Statistical Analysis of Spacecraft Measurements, *ResearchGate*, doi:10.13140/2.1.2588.8321. 3.2

Cassak, P. A., and S. A. Fuselier (2016), *Reconnection at Earth's Dayside Magnetopause*, pp. 213–276, Springer International Publishing, Cham, doi:10.1007/978-3-319-26432-5_6. 3, 3.1

Cassak, P. A., D. J. Mullan, and M. A. Shay (2007), From Solar and Stellar Flares to Coronal Heating: Theory and Observations of How Magnetic Reconnection Regulates Coronal Conditions, *arXiv*, doi:10.1086/587055. 1, 3

Chappell, C. R., T. E. Moore, and J. H. Waite (1987), The ionosphere as a fully adequate source of plasma for the Earth's magnetosphere, *J. Geophys. Res. Space Phys.*, *92*(A6), 5896–5910, doi:10.1029/JA092iA06p05896. 3.2, 3.8

Choudhuri, A. R. (1998), *The Physics of Fluids and Plasmas: An Introduction for Astrophysicists*, Cambridge University Press, Cambridge, England, UK. 2

Christon, S. P., C. S. Cohen, G. Gloeckler, T. E. Eastman, A. B. Galvin, F. M. Ipavich, Y.-K. Ko, A. T. Y. Lui, R. A. Lundgren, R. W. McEntire, E. C. Roelof, and D. J. Williams (1998), Concurrent observations of solar wind oxygen by Geotail in the magnetosphere and wind in interplanetary space, *Geophys. Res. Lett.*, *25*(15), 2987–2990, doi:10.1029/98GL01408. 3.2.2

Comfort, R. H. (1988), The Magnetic Mirror Force in Plasma Fluid Models, in *Modeling Magnetospheric Plasma*, pp. 51–53, American Geophysical Union (AGU), doi:10.1029/GM044p0051. 3.2.1

Craven, P. D., R. C. Olsen, C. R. Chappell, and L. Kakani (1985), Observations of molecular ions in the Earth's magnetosphere, *J. Geophys. Res. Space Phys.*, *90*(A8), 7599–7605, doi:10.1029/JA090iA08p07599. 3.2.1

Dai, L. (2018), Structures of Hall Fields in Asymmetric Magnetic Reconnection, *J. Geophys. Res. Space Phys.*, *123*(9), 7332–7341, doi:10.1029/2018JA025251. 3.1.2

Dawson, J. M. (1983), Particle simulation of plasmas, *Rev. Mod. Phys.*, *55*(2), 403–447, doi:10.1103/RevModPhys.55.403. 4.4, 4.2.1, 4.2.2

de Gouveia Dal Pino, E. M., P. P. Piovezan, and L. H. S. Kadowaki (2010), The role of magnetic reconnection on jet/accretion disk systems, *Astron. Astrophys.*, *518*, A5, doi:10.1051/0004-6361/200913462. 1

Divin, A., Yu. V. Khotyaintsev, A. Vaivads, M. André, S. Toledo-Redondo, S. Markidis, and G. Lapenta (2016), Three-scale structure of diffusion region in the presence of cold ions, *J. Geophys. Res. Space Phys.*, *121*(12), 12,001–12,013, doi:10.1002/2016JA023606. 1, 3.2.3

Drake, J. F., M. Opher, M. Swisdak, and J. N. Chamoun (2010), A Magnetic Reconnection Mechanism for the Generation of Anomalous Cosmic Rays, *Astrophys. J.*, *709*(2), 963–974, doi:10.1088/0004-637x/709/2/963. 1

Dungey, J. W. (1961), Interplanetary Magnetic Field and the Auroral Zones, *Phys. Rev. Lett.*, *6*(2), 47–48, doi:10.1103/PhysRevLett.6.47. 3

Dupree, T. H. (1964), Theory of Radiation Emission and Absorption in Plasma, *Phys. Fluids*, *7*(7), 923–940, doi:10.1063/1.1711339. 2.3

Ergun, R. E., S. Tucker, J. Westfall, K. A. Goodrich, D. M. Malaspina, D. Summers, J. Wallace, M. Karlsson, J. Mack, N. Brennan, B. Pyke, P. Withnell, R. Torbert, J. Macri, D. Rau, I. Dors, J. Needell, P.-A. Lindqvist, G. Olsson, and C. M. Cully (2016), The Axial Double Probe and Fields Signal Processing for the MMS Mission, *Space Sci. Rev.*, *199*(1), 167–188, doi:10.1007/s11214-014-0115-x. 4.1.1

Evans, M. W., and F. H. Harlow (1957), The Particle-In-Cell Method for Hydrodynamic Calculations, [Online; accessed 1. Feb. 2022]. 4.2.2

Forbes, T. G. (2001), The nature of Petschek-type reconnection, *Earth Planets Space*, *53*(6), 423–429, doi:10.1186/BF03353252. 3.1.1

Frank, L. A., K. L. Ackerson, and D. M. Yeager (1977), Observations of atomic oxygen (O+) in the Earth's magnetotail, *J. Geophys. Res.*, *82*(1), 129–134, doi:10.1029/JA082i001p00129. 3.2.2

Fuselier, S. A., J. L. Burch, P. A. Cassak, J. Goldstein, R. G. Gomez, K. Goodrich, W. S. Lewis, D. Malaspina, J. Mukherjee, R. Nakamura, S. M. Petrinec, C. T. Russell, R. J. Strangeway, R. B. Torbert, K. J. Trattner, and P. Valek (2016), Magnetospheric ion influence on magnetic reconnection at the duskside magnetopause, *Geophys. Res. Lett.*, *43*(4), 1435–1442, doi:10.1002/2015GL067358. 3.2

Fuselier, S. A., J. L. Burch, J. Mukherjee, K. J. Genestreti, S. K. Vines, R. Gomez, J. Goldstein, K. J. Trattner, S. M. Petrinec, B. Lavraud, and R. J. Strangeway (2017), Magnetospheric ion influence at the dayside magnetopause, *J. Geophys. Res. Space Phys.*, *122*(8), 8617–8631, doi:10.1002/2017JA024515. 3.2.3

Fuselier, S. A., K. J. Trattner, S. M. Petrinec, M. H. Denton, S. Toledo-Redondo, M. André, N. Aunai, C. R. Chappell, A. Glocer, S. E. Haaland, M. Hesse, L. M. Kistler, B. Lavraud, W. Li, T. E. Moore, D. Graham, L. Alm, P. Tenfjord, J. Dargent, S. K. Vines, K. Nykyri, J. L. Burch, and R. J. Strangeway (2019), Mass Loading the Earth's Dayside Magnetopause Boundary Layer and Its Effect on Magnetic Reconnection, *Geophys. Res. Lett.*, *46*(12), 6204–6213, doi:10.1029/2019GL082384. 3.2.3, 3.2.3

Garrett, H. B. (1981), The charging of spacecraft surfaces, *Rev. Geophys.*, *19*(4), 577–616, doi:10.1029/RG019i004p00577. 3.2.2

George, D. E., and J.-M. Jahn (2020), Energized Oxygen in the Magnetotail: Current Sheet Bifurcation From Speiser Motion, *J. Geophys. Res. Space Phys.*, *125*(2), e2019JA027,339, doi:10.1029/2019JA027339. 3.2.3

Giovanelli, R. G. (1947), Magnetic and Electric Phenomena in the Sun's Atmosphere associated with Sunspots, *Mon. Not. R. Astron. Soc.*, *107*(4), 338–355, doi:10.1093/mnras/107.4.338. 3.1

Glocer, A., D. Welling, C. R. Chappell, G. Toth, M.-C. Fok, C. Komar, S.-B. Kang, N. Buzulukova, C. Ferradas, S. Bingham, and C. Mouikis (2020), A Case Study on the Origin of Near-Earth Plasma, *J. Geophys. Res. Space Phys.*, *125*(11), e2020JA028,205, doi:10.1029/2020JA028205. 3.2.2, 5

Gloeckler, G., and D. C. Hamilton (1987), AMPTE Ion Composition Results, *Phys. Scr.*, *T18*(T18), 73–84, doi:10.1088/0031-8949/1987/t18/009. 3.2.2

Goldston, R. J., and P. H. Rutherford (1995), *Introduction to Plasma Physics*, Institute of Physics Pub. 2

Gonzalez, W., and E. Parker (2016), *Magnetic Reconnection*, Springer, Cham, Switzerland, doi:10.1007/978-3-319-26432-5. 1, 3

Goodman, J., and D. Uzdensky (2008), Reconnection in marginally collisionless accretion disk coronae, *Astrophys. J.*, *688*(1), 555–558, doi:10.1086/592345. 1, 3

Grard, R. J. L. (1973), Properties of the satellite photoelectron sheath derived from photoemission laboratory measurements, *J. Geophys. Res.*, *78*(16), 2885–2906, doi:10.1029/JA078i016p02885. 3.2.2

Haaland, S., K. Svenes, B. Lybekk, and A. Pedersen (2012), A survey of the polar cap density based on Cluster EFW probe measurements: Solar wind and solar irradiation dependence, *J. Geophys. Res. Space Phys.*, *117*(A1), doi:10.1029/2011JA017250. 3.2.3

Henderson, P. D., C. J. Owen, A. D. Lahiff, I. V. Alexeev, A. N. Fazakerley, E. Lucek, and H. Rème (2006), Cluster PEACE observations of electron pressure tensor divergence in the magnetotail, *Geophys. Res. Lett.*, *33*(22), doi:10.1029/2006GL027868. 4.1

Hesse, M., and J. Birn (2004), On the cessation of magnetic reconnection, *Ann. Geophys.*, *22*(2), 603–612, doi:10.5194/angeo-22-603-2004. 3.2.4

Hesse, M., and P. A. Cassak (2020), Magnetic Reconnection in the Space Sciences: Past, Present, and Future, *J. Geophys. Res. Space Phys.*, *125*(2), e2018JA025,935, doi:10.1029/2018JA025935. 4

Hesse, M., and K. Schindler (1988), A theoretical foundation of general magnetic reconnection, *J. Geophys. Res.*, *93*(A6), 5559–5567, doi:10.1029/JA093iA06p05559. 3.1.3

Hesse, M., D. Winske, and M. M. Kuznetsova (1995), Hybrid modeling of collisionless reconnection in two-dimensional current sheets: Simulations, *J. Geophys. Res. Space Phys.*, *100*(A11), 21,815–21,825, doi:10.1029/95JA01559. 3.1.2

Hesse, M., K. Schindler, J. Birn, and M. Kuznetsova (1999), The diffusion region in collisionless magnetic reconnection, *Phys. Plasma*, *6*(5), 1781–1795, doi:10.1063/1.873436. 3.1.2, 4.2.2, 4.2.2

Hesse, M., N. Aunai, S. Zenitani, M. Kuznetsova, and J. Birn (2013), Aspects of collisionless magnetic reconnection in asymmetric systems, *Phys. Plasma*, *20*(6), 061,210, doi:10.1063/1.4811467. 3.2.4

Hesse, M., N. Aunai, D. Sibeck, and J. Birn (2014), On the electron diffusion region in planar, asymmetric, systems, *Geophys. Res. Lett.*, *41*(24), 8673–8680, doi:10.1002/2014GL061586. 3.1.2

Hesse, M., Y.-H. Liu, L.-J. Chen, N. Bessho, S. Wang, J. L. Burch, T. Moretto, C. Norgren, K. J. Genestreti, T. D. Phan, and P. Tenfjord (2018), The physical foundation of the reconnection electric field, *Phys. Plasma*, *25*(3), 032,901, doi:10.1063/1.5021461. 3.1.2, 3.1.2

Hoffman, J. H., W. H. Dodson, C. R. Lippincott, and H. D. Hammack (1974), Initial ion composition results from the Isis 2 satellite, *J. Geophys. Res.*, *79*(28), 4246–4251, doi:10.1029/JA079i028p04246. 3.2.1

Holmes, J. C., R. E. Ergun, D. L. Newman, N. Ahmadi, and J. L. Burch (2018), Electron Phase-Space Holes in Three Dimensions: Multi-Spacecraft Observations by Magnetospheric Multiscale, *J. Geophys. Res. Space Phys.*, *123*(3), doi:10.1029/2018JA025750. 4.1

Ilie, R., and M. W. Liemohn (2016), The outflow of ionospheric nitrogen ions: A possible tracer for the altitude-dependent transport and energization processes of ionospheric plasma, *J. Geophys. Res. Space Phys.*, *121*(9), 9250–9255, doi:10.1002/2015JA022162. 3.2.1

Karimabadi, H., V. Roytershteyn, C. G. Mouikis, L. M. Kistler, and W. Daughton (2011), Flushing effect in reconnection: Effects of minority species of oxygen ions, *Planet. Space Sci.*, *59*(7), 526–536, doi:10.1016/j.pss.2010.07.014. 3.2.3

Kasahara, S., H. Hasegawa, K. Keika, Y. Miyashita, M. N. Nishino, T. Sotirelis, Y. Saito, and T. Mukai (2008), Escape of high-energy oxygen ions through magnetopause reconnection under northward IMF, *Ann. Geophys.*, *26*(12), 3955–3966, doi:10.5194/angeo-26-3955-2008. 3.2.2

Kistler, L. M., and C. G. Mouikis (2016), The inner magnetosphere ion composition and local time distribution over a solar cycle, *J. Geophys. Res. Space Phys.*, *121*(3), 2009–2032, doi:10.1002/2015JA021883. 3.2, 3.2.2, 3.2.2, 3.2.2, 3.2.3

Kistler, L. M., C. Mouikis, E. Möbius, B. Klecker, J. A. Sauvaud, H. Réme, A. Korth, M. F. Marcucci, R. Lundin, G. K. Parks, and A. Balogh (2005), Contribution of nonadiabatic ions to the cross-tail current in an O+ dominated thin current sheet, *J. Geophys. Res. Space Phys.*, *110*(A6), doi:10.1029/2004JA010653. 3.2.3

Kistler, L. M., C. G. Mouikis, X. Cao, H. Frey, B. Klecker, I. Dandouras, A. Korth, M. F. Marcucci, R. Lundin, M. McCarthy, R. Friedel, and E. Lucek (2006), Ion composition and pressure changes in storm time and nonstorm substorms in the vicinity of the near-Earth neutral line, *J. Geophys. Res. Space Phys.*, *111*(A11), doi:10.1029/2006JA011939. 3.2.3

Kistler, L. M., C. G. Mouikis, B. Klecker, and I. Dandouras (2010), Cusp as a source for oxygen in the plasma sheet during geomagnetic storms, *J. Geophys. Res. Space Phys.*, *115*(A3), doi:10.1029/2009JA014838. 5

Klimontovich, Y. L. (1967), *The Statistical Theory of Non-Equilibrium Processes in a Plasma*, Pergamon Press, Oxford, England, UK. 2.3

Kolstø, H. M., M. Hesse, C. Norgren, P. Tenfjord, S. F. Spinnangr, and N. Kwagala (2020a), Collisionless Magnetic Reconnection in an Asymmetric Oxygen Density Configuration, *Geophys. Res. Lett.*, *47*(1), e2019GL085,359, doi:10.1029/2019GL085359. 3.1.2, 3.2.3, 3.2.3, 3.12, 3.2.3, 3.2.4, 3.2.4

Kolstø, H. M., M. Hesse, C. Norgren, P. Tenfjord, S. F. Spinnangr, and N. Kwagala (2020b), On the Impact of a Streaming Oxygen Population on Collisionless Magnetic Reconnection, *Geophys. Res. Lett.*, *47*(22), e2020GL089,462, doi:10.1029/2020GL089462. 3.2.3, 3.2.3, 3.2.4, 3.2.4

Kolstø, H. M., C. Norgren, M. Hesse, L.-J. Chen, P. Tenfjord, S. F. Spinnangr, and N. Kwagala (2021), Magnetospheric Multiscale Observations of an Expanding Oxygen Wave in Magnetic Reconnection, *Geophys. Res. Lett.*, *48*(19), e2021GL095,065, doi:10.1029/2021GL095065. 2.3, 3.2.3, 3.2.4, 3.2.4

Kube, R., R. M. Churchill, and B. Sturdevant (2021), Machine learning accelerated particle-in-cell plasma simulations, *arXiv*. 4.2.2

Kulsrud, R. M. (2001), Magnetic reconnection: Sweet-Parker versus Petschek, *Earth Planets Space*, *53*(6), 417–422, doi:10.1186/BF03353251. 3.1.1

Langdon, A. B. (1985), Implicit Plasma Simulation, *Space Sci. Rev.*, *42*(1-2), 67–83, doi:10.1007/BF00218224. 4.2.2

Lapenta, G. (2015), Kinetic Plasma Simulation: Particle In Cell Method, *ResearchGate*, doi:10.13140/RG.2.1.3319.2801. 4.2.1, 4.2.1, 4.2.1, 4.2.2, 4.5

Lapenta, G., J. U. Brackbill, and P. Ricci (2006), Kinetic approach to microscopic-macroscopic coupling in space and laboratory plasmas, *Phys. Plasma*, *13*(5), 055,904, doi:10.1063/1.2173623. 4.2.1, 4.2.2, 4.2.2, 4.2.2

Lapenta, G., J. Berchem, M. Zhou, R. J. Walker, M. El-Alaoui, M. L. Goldstein, W. R. Paterson, B. L. Giles, C. J. Pollock, C. T. Russell, R. J. Strangeway, R. E. Ergun, Y. V. Khotyaintsev, R. B. Torbert, and J. L. Burch (2017), On the origin of the crescent-shaped distributions observed by MMS at the magnetopause, *J. Geophys. Res. Space Phys.*, *122*(2), 2024–2039, doi:10.1002/2016JA023290. 3.1.2

Lee, J. H., and V. Angelopoulos (2014), On the presence and properties of cold ions near Earth's equatorial magnetosphere, *J. Geophys. Res. Space Phys.*, *119*(3), 1749–1770, doi:10.1002/2013JA019305. 3.2.2, 3.2.2

Lennartsson, W. (1989), Energetic (0.1- to 16-keV/e) magnetospheric ion composition at different levels of solar F10.7, *J. Geophys. Res. Space Phys.*, *94*(A4), 3600–3610, doi:10.1029/JA094iA04p03600. 3.2.2, 3.2.2

Lennartsson, W., and R. D. Sharp (1985), Relative contributions of terrestrial and solar wind ions in the plasma sheet, *Adv. Space Res.*, *5*(4), 411–414, doi:10.1016/0273-1177(85)90167-X. 3.2.2

Lennartsson, W., and E. G. Shelley (1986), Survey of 0.1- to 16-keV/e plasma sheet ion composition, *J. Geophys. Res. Space Phys.*, *91*(A3), 3061–3076, doi:10.1029/JA091iA03p03061. 3.2.2, 3.2.2

Levy, R. H., H. E. Petschek, and G. L. Siscoe (1963), AERODYNAMIC ASPECTS OF THE MAGNETOSPHERIC FLOW. Research Report No. 170, [Online; accessed 10. Jan. 2022]. 3

Li, K., S. Haaland, A. Eriksson, M. André, E. Engwall, Y. Wei, E. A. Kronberg, M. Fränz, P. W. Daly, H. Zhao, and Q. Y. Ren (2013), Transport of cold ions from the polar ionosphere to the plasma sheet, *J. Geophys. Res. Space Phys.*, *118*(9), 5467–5477, doi:10.1002/jgra.50518. 5

Liang, H., M. Ashour-Abdalla, G. Lapenta, and R. J. Walker (2016), Oxygen impacts on dipolarization fronts and reconnection rate, *J. Geophys. Res. Space Phys.*, *121*(2), 1148–1166, doi:10.1002/2015JA021747. 3.2.3

Liang, H., G. Lapenta, R. J. Walker, D. Schriver, M. El-Alaoui, and J. Berchem (2017), Oxygen acceleration in magnetotail reconnection, *J. Geophys. Res. Space Phys.*, *122*(1), 618–639, doi:10.1002/2016JA023060. 3.2.3

Liao, J., L. M. Kistler, C. G. Mouikis, B. Klecker, I. Dandouras, and J.-C. Zhang (2010), Statistical study of O+ transport from the cusp to the lobes with Cluster CODIF data, *J. Geophys. Res. Space Phys.*, *115*(A12), doi:10.1029/2010JA015613. 3.2.2

Liao, J., L. M. Kistler, C. G. Mouikis, B. Klecker, and I. Dandouras (2012), Solar cycle dependence of the cusp O+access to the near-Earth magnetotail, *J. Geophys. Res. Space Phys.*, *117*(A10), doi:10.1029/2012JA017819. 3.2.2

Liao, J., L. M. Kistler, C. G. Mouikis, B. Klecker, and I. Dandouras (2015), Acceleration of O+ from the cusp to the plasma sheet, *J. Geophys. Res. Space Phys.*, *120*(2), 1022–1034, doi:10.1002/2014JA020341. 1.1, 3.2.2, 5

Lindqvist, P.-A., G. Olsson, R. B. Torbert, B. King, M. Granoff, D. Rau, G. Needell, S. Turco, I. Dors, P. Beckman, J. Macri, C. Frost, J. Salwen, A. Eriksson, L. Åhlén, Y. V. Khotyaintsev, J. Porter, K. Lappalainen, R. E. Ergun, W. Wermeer, and S. Tucker (2016), The Spin-Plane Double Probe Electric Field Instrument for MMS, *Space Sci. Rev.*, *199*(1), 137–165, doi:10.1007/s11214-014-0116-9. 4.1.1

Lindstedt, T., Y. V. Khotyaintsev, A. Vaivads, M. André, H. Nilsson, and M. Waara (2010), Oxygen energization by localized perpendicular electric fields at the cusp boundary, *Geophys. Res. Lett.*, *37*(9), doi:10.1029/2010GL043117. 3.2.3

Liu, Y. H., C. G. Mouikis, L. M. Kistler, S. Wang, V. Roytershteyn, and H. Karimabadi (2015), The heavy ion diffusion region in magnetic reconnection in the Earth's magnetotail, *J. Geophys. Res. Space Phys.*, *120*(5), 3535–3551, doi:10.1002/2015JA020982. 3.2.3, 3.11

Lotko, W. (2007), The magnetosphere–ionosphere system from the perspective of plasma circulation: A tutorial, *J. Atmos. Sol. Terr. Phys.*, *69*(3), 191–211, doi:10.1016/j.jastp.2006.08.011. 1, 3.2.3

Lyons, L. R., and D. C. Pridmore-Brown (1990), Force balance near an X line in a collisionless plasma, *J. Geophys. Res.*, *95*(A12), 20,903–20,909, doi:10.1029/JA095iA12p20903. 3.1.2

Maggiolo, R., and L. M. Kistler (2014), Spatial variation in the plasma sheet composition: Dependence on geomagnetic and solar activity, *J. Geophys. Res. Space Phys.*, *119*(4), 2836–2857, doi:10.1002/2013JA019517. 1, 3.2.2, 3.10, 3.2.2, 3.2.3

Markidis, S., G. Lapenta, and Rizwan-uddin (2010), Multi-scale simulations of plasma with iPIC3D, *Math. Comput. Simul.*, *80*(7), 1509–1519, doi:10.1016/j.matcom.2009.08.038. 4.2.2, 4.2.2

Markidis, S., G. Lapenta, L. Bettarini, M. Goldman, D. Newman, and L. Andersson (2011), Kinetic simulations of magnetic reconnection in presence of a background O+ population, *J. Geophys. Res. Space Phys.*, *116*(A1), doi:10.1029/2011JA016429. 3.1.2, 3.2.3, 3.2.3, 3.2.4, 3.2.4

Mason, R. (1983), Implicit moment PIC-hybrid simulation of collisional plasmas, *undefined*. 4.2.2

Mauk, B. H., J. B. Blake, D. N. Baker, J. H. Clemmons, G. D. Reeves, H. E. Spence, S. E. Jaskulek, C. E. Schlemm, L. E. Brown, S. A. Cooper, J. V. Craft, J. F. Fennell, R. S. Gurnee, C. M. Hammock, J. R. Hayes, P. A. Hill, G. C. Ho, J. C. Hutcheson, A. D. Jacques, S. Kerem, D. G. Mitchell, K. S. Nelson, N. P. Paschalidis, E. Rossano, M. R. Stokes, and J. H. Westlake (2016), The Energetic Particle Detector (EPD) Investigation and the Energetic Ion Spectrometer (EIS) for the Magnetospheric Multiscale (MMS) Mission, *Space Sci. Rev.*, *199*(1), 471–514, doi:10.1007/s11214-014-0055-5. 4.1.1

Merkin, V. G., E. V. Panov, K. A. Sorathia, and A. Y. Ukhorskiy (2019), Contribution of Bursty Bulk Flows to the Global Dipolarization of the Magnetotail During an Isolated Substorm, *J. Geophys. Res. Space Phys.*, *124*(11), 8647–8668, doi:10.1029/2019JA026872. 3.2.3

Moore, T. E., M. O. Chandler, M.-C. Fok, B. L. Giles, D. C. Delcourt, J. L. Horwitz, and C. J. Pollock (2001), Ring Currents and Internal Plasma Sources, *Space Sci. Rev.*, *95*(1-2), 555–568, doi:10.1023/A:1005264907107. 3.2

Mouikis, C. G., L. M. Kistler, Y. H. Liu, B. Klecker, A. Korth, and I. Dandouras (2010), H+ and O+ content of the plasma sheet at 15–19 Re as a function of geomagnetic and solar activity, *J. Geophys. Res. Space Phys.*, *115*(A12), doi:10.1029/2010JA015978. 3.9, 3.2.2, 3.2.2, 3.2.3

Mozer, F. S., P. L. Pritchett, J. Bonnell, D. Sundkvist, and M. T. Chang (2008), Observations and simulations of asymmetric magnetic field reconnection, *J. Geophys. Res. Space Phys.*, *113*(A1), doi:10.1029/2008JA013535. 3.1.2

NASA/Smegelsky, B. (2015), MMS – The Wide View, *NASA*. 4.1

Nosé, M., A. Ieda, and S. P. Christon (2009), Geotail observations of plasma sheet ion composition over 16 years: On variations of average plasma ion mass and O+ triggering substorm model, *J. Geophys. Res. Space Phys.*, *114*(A7), doi:10.1029/2009JA014203. 3.2.2

Oieroset, M., T. D. Phan, M. Fujimoto, R. P. Lin, and R. P. Lepping (2001), In situ detection of collisionless reconnection in the Earth's magnetotail, *Nature*, *412*(6845), 414–417, doi:10.1038/35086520. 1

Parker, E. M. (2016), *Fundamental Concepts Associated with Magnetic Reconnection*, pp. 3–6, Springer International Publishing, Cham, doi:10.1007/978-3-319-26432-5_6. 2.6

Parker, E. N. (1957), Newtonian Development of the Dynamical Properties of Ionized Gases of Low Density, *Phys. Rev.*, *107*(4), 924–933, doi:10.1103/PhysRev.107.924. 3.1

Parks, G. K. (1991), *Physics Of Space Plasmas: An Introduction*, Basic Books, New York, NY, USA. 2

Paschmann, G., B. U. Ö. Sonnerup, I. Papamastorakis, N. Sckopke, G. Haerendel, S. J. Bame, J. R. Asbridge, J. T. Gosling, C. T. Russell, and R. C. Elphic (1979), Plasma acceleration at the Earth's magnetopause: evidence for reconnection - Nature, *Nature*, *282*(5736), 243–246, doi:10.1038/282243a0. 1, 3, 3, 3

Petschek, H. E. (1964), *Magnetic Field Annihilation*, vol. 50. 3.1.1

Phan, T. D., G. Paschmann, J. T. Gosling, M. Oieroset, M. Fujimoto, J. F. Drake, and V. Angelopoulos (2013), The dependence of magnetic reconnection on plasma β and magnetic shear: Evidence from magnetopause observations, *Geophys. Res. Lett.*, *40*(1), 11–16, doi:10.1029/2012GL054528. 3.2.4

Pollock, C., T. Moore, A. Jacques, J. Burch, U. Gliese, and Y. Saito (2016), Fast Plasma Investigation for Magnetospheric Multiscale, *Space Sci. Rev.*, *199*(1), 331–406, doi:10.1007/s11214-016-0245-4. 4.1, 4.1.1

Priest, E., and T. Forbes (2000), *Magnetic Reconnection: MHD Theory and Applications*, Cambridge University Press, Cambridge, England, UK, doi:10.1017/CBO9780511525087. 3.4

Pritchett, P. L. (2003), Particle-in-Cell Simulation of Plasmas— A Tutorial, in *Space Plasma Simulation*, pp. 1–24, Springer, Berlin, Germany, doi:10.1007/3-540-36530-3_1. 4.2, 4.2.1, 4.2.2

R W. Hockney, J. W. E. (2021), *Computer Simulation Using Particles*, Taylor & Francis, Andover, England, UK, doi:10.1201/9780367806934. 4.2.2, 4.2.2

Russell, C. T., B. J. Anderson, W. Baumjohann, K. R. Bromund, D. Dearborn, D. Fischer, G. Le, H. K. Leinweber, D. Leneman, W. Magnes, J. D. Means, M. B. Moldwin, R. Nakamura, D. Pierce, F. Plaschke, K. M. Rowe, J. A. Slavin, R. J. Strangeway, R. Torbert, C. Hagen, I. Jernej, A. Valavanoglou, and I. Richter (2016), The Magnetospheric Multiscale Magnetometers, *Space Sci. Rev.*, *199*(1), 189–256, doi:10.1007/s11214-014-0057-3. 4.1.1

Schindler, K., M. Hesse, and J. Birn (1988), General magnetic reconnection, parallel electric fields, and helicity, *J. Geophys. Res. Space Phys.*, *93*(A6), 5547–5557, doi:10.1029/JA093iA06p05547. 3.1.3

Schunk, R. W. (2007), Time-dependent simulations of the global polar wind, *J. Atmos. Sol. Terr. Phys.*, *69*(16), 2028–2047, doi:10.1016/j.jastp.2007.08.009. 3.2.1

Seki, K., M. Hirahara, M. Hoshino, T. Terasawa, R. C. Elphic, Y. Saito, T. Mukai, H. Hayakawa, H. Kojima, and H. Matsumoto (2003), Cold ions in the hot plasma sheet of Earth's magnetotail - Nature, *Nature*, *422*(6932), 589–592, doi:10.1038/nature01502. 3.2.2

Shalaby, M., A. E. Broderick, P. Chang, C. Pfrommer, A. Lamberts, and E. Puchwein (2017), SHARP: A Spatially Higher-order, Relativistic Particle-in-Cell Code, *arXiv*, doi:10.3847/1538-4357/aa6d13. 4.2.1, 4.2.2

Shay, M. A., and M. Swisdak (2004), Three-Species Collisionless Reconnection: Effect of O^+ on Magnetotail Reconnection, *Phys. Rev. Lett.*, *93*(17), 175,001, doi:10.1103/PhysRevLett.93.175001. 1, 3.2.3

Shelley, E. G., R. G. Johnson, and R. D. Sharp (1972), Satellite observations of energetic heavy ions during a geomagnetic storm, *J. Geophys. Res.*, *77*(31), 6104–6110, doi:10.1029/JA077i031p06104. 3.2.1

Shibayama, T., K. Kusano, T. Miyoshi, and A. Bhattacharjee (2019), Mechanism of non-steady Petschek-type reconnection with uniform resistivity, *Phys. Plasma*, *26*(3), 032,903, doi:10.1063/1.5084771. 3.1.1

Sonnerup, B. U. Ö. (1979), *Magnetic field reconnection*, vol. 3. 3.1.2

Spinnangr, S. F., M. Hesse, P. Tenfjord, C. Norgren, H. M. Kolstø, N. K. Kwagala, and T. M. Jørgensen (2021), The Micro-Macro Coupling of Mass-Loading in Symmetric Magnetic Reconnection With Cold Ions, *Geophys. Res. Lett.*, *48*(13), e2020GL090,690, doi:10.1029/2020GL090690. 3.2.3

Su, Y.-J., J. E. Borovsky, M. F. Thomsen, R. C. Elphic, and D. J. McComas (2000), Plasmaspheric material at the reconnecting magnetopause, *J. Geophys. Res. Space Phys.*, *105*(A4), 7591–7600, doi:10.1029/1999JA000266. 3.2.3

Sweet, P. A. (1958), 14. The neutral point theory of solar flares, *Symp. - Int. Astron. Union*, *6*, 123–134, doi:10.1017/S0074180900237704. 3.1

Swisdak, M., B. N. Rogers, J. F. Drake, and M. A. Shay (2003), Diamagnetic suppression of component magnetic reconnection at the magnetopause, *J. Geophys. Res. Space Phys.*, *108*(A5), doi:10.1029/2002JA009726. 3.16, 3.2.4

Swisdak, M., M. Opher, J. F. Drake, and F. A. Bibi (2010), The Vector Direction of the Interstellar Magnetic Field Outside the Heliosphere, *arXiv*, doi:10.1088/0004-637X/710/2/1769. 3.2.4

Tenfjord, P., M. Hesse, and C. Norgren (2018), The Formation of an Oxygen Wave by Magnetic Reconnection, *J. Geophys. Res. Space Phys.*, *123*(11), 9370–9380, doi:10.1029/2018JA026026. 1.1, 3.2.3, 3.2.4, 3.2.4, 3.2.4, 5

Tenfjord, P., M. Hesse, C. Norgren, S. F. Spinnangr, and H. Kolstø (2019), The impact of oxygen on the reconnection rate, *Geophys. Res. Lett.*, doi:10.1029/2019GL082175. 3.2.3, 3.12, 3.2.3, 5, 6.1

Tenfjord, P., M. Hesse, C. Norgren, S. F. Spinnangr, H. Kolstø, and N. Kwagala (2020), Interaction of cold streaming protons with the reconnection process, *J. Geophys. Res. Space Phys.*, *n/a*(n/a), e2019JA027,619, doi:10.1029/2019JA027619. 3.2.3, 5

Toledo-Redondo, S., A. Vaivads, M. André, and Yu. V. Khotyaintsev (2015), Modification of the Hall physics in magnetic reconnection due to cold ions at the Earth's magnetopause, *Geophys. Res. Lett.*, *42*(15), 6146–6154, doi:10.1002/2015GL065129. 1, 3.2.3

Toledo-Redondo, S., M. André, Y. V. Khotyaintsev, A. Vaivads, A. Walsh, W. Li, D. B. Graham, B. Lavraud, A. Masson, N. Aunai, A. Divin, J. Dargent, S. Fuselier, D. J. Gershman, J. Dorelli, B. Giles, L. Avanov, C. Pollock, Y. Saito, T. E. Moore, V. Coffey, M. O. Chandler, P.-A. Lindqvist, R. Torbert, and C. T. Russell (2016), Cold ion demagnetization near the X-line of magnetic reconnection, *Geophys. Res. Lett.*, *43*(13), 6759–6767, doi:10.1002/2016GL069877. 3.2.2, 3.2.3

Toledo-Redondo, S., M. André, Y. V. Khotyaintsev, B. Lavraud, A. Vaivads, D. B. Graham, W. Li, D. Perrone, S. Fuselier, D. J. Gershman, N. Aunai, J. Dargent, B. Giles, O. Le Contel, P.-A. Lindqvist, R. E. Ergun, C. T. Russell, and J. L. Burch (2017), Energy budget and mechanisms of cold ion heating in asymmetric magnetic reconnection, *J. Geophys. Res. Space Phys.*, *122*(9), 9396–9413, doi:10.1002/2017JA024553. 3.2

Toledo-Redondo, S., M. André, N. Aunai, C. R. Chappell, J. Dargent, S. A. Fuselier, A. Glocer, D. B. Graham, S. Haaland, M. Hesse, L. M. Kistler, B. Lavraud, W. Li, T. E. Moore, P. Tenfjord, and S. K. Vines (2021), Impacts of ionospheric ions on magnetic reconnection and Earth's magnetosphere dynamics, *Rev. Geophys.*, *n/a*(n/a), e2020RG000,707, doi:10.1029/2020RG000707. 3.2.1, 3.2.1, 3.2.2, 3.2.2

Torbert, R. B., C. T. Russell, W. Magnes, R. E. Ergun, P.-A. Lindqvist, O. LeContel, H. Vaith, J. Macri, S. Myers, D. Rau, J. Needell, B. King, M. Granoff, M. Chutter,

I. Dors, G. Olsson, Y. V. Khotyaintsev, A. Eriksson, C. A. Kletzing, S. Bounds, B. Anderson, W. Baumjohann, M. Steller, K. Bromund, G. Le, R. Nakamura, R. J. Strangeway, H. K. Leinweber, S. Tucker, J. Westfall, D. Fischer, F. Plaschke, J. Porter, and K. Lappalainen (2016), The FIELDS Instrument Suite on MMS: Scientific Objectives, Measurements, and Data Products, *Space Sci. Rev.*, *199*(1), 105–135, doi:10.1007/s11214-014-0109-8. 4.1.1

Torkar, K., R. Nakamura, M. Tajmar, C. Scharlemann, H. Jeszenszky, G. Laky, G. Fremuth, C. P. Escoubet, and K. Svenes (2016), Active Spacecraft Potential Control Investigation, *Space Sci. Rev.*, *199*(1), 515–544, doi:10.1007/s11214-014-0049-3. 4.1.1

Treumann, R. A., and W. Baumjohann (2013), Collisionless magnetic reconnection in space plasmas, *Front. Phys.*, *0*, doi:10.3389/fphy.2013.00031. 3.1.2

Uzdensky, D. A. (2003), Petschek-like Reconnection with Current-driven Anomalous Resistivity and Its Application to Solar Flares, *Astrophys. J.*, *587*(1), 450–457, doi:10.1086/368075. 5

Vasyliunas, V. M. (1975), Theoretical models of magnetic field line merging, *Rev. Geophys.*, *13*(1), 303–336, doi:10.1029/RG013i001p00303. 3, 3.1.2

Vlasov, A. A. (1945), Theory of an Assembly of Particles with Collective Interaction, *Phys. Fluids*, *9*, 25–40. 2.3

von Alfthan, S., Y. Kempf, S. Hoilijoki, I. Honkonen, and M. Palmroth (2014), Vlasiator: First global hybrid-Vlasov simulations of Earth's foreshock and magnetosheath, *J. Atmos. Sol. Terr. Phys.*, *120*(1), 24–35, doi:10.1016/j.jastp.2014.08.012. 6.2

Vu, H. X., and J. U. Brackbill (1992), CELEST1D: an implicit, fully kinetic model for low-frequency, electromagnetic plasma simulation, *Comput. Phys. Commun.*, *69*(2), 253–276, doi:10.1016/0010-4655(92)90165-U. 4.2.2

Walsh, B. M., D. G. Sibeck, Y. Nishimura, and V. Angelopoulos (2013), Statistical analysis of the plasmaspheric plume at the magnetopause, *J. Geophys. Res. Space Phys.*, *118*(8), 4844–4851, doi:10.1002/jgra.50458. 3.2.3

Walsh, B. M., T. D. Phan, D. G. Sibeck, and V. M. Souza (2014), The plasmaspheric plume and magnetopause reconnection, *Geophys. Res. Lett.*, *41*(2), 223–228, doi:10.1002/2013GL058802. 3.2.3

Wang, S., L. M. Kistler, C. G. Mouikis, and S. M. Petrinec (2015), Dependence of the dayside magnetopause reconnection rate on local conditions, *J. Geophys. Res. Space Phys.*, *120*(8), 6386–6408, doi:10.1002/2015JA021524. 3.2.3

Weiss, L. A., P. H. Reiff, J. J. Moses, R. A. Heelis, B. D. Moore, P. H. Reiff, J. J. Moses, R. A. Heelis, and B. D. Moore (1992), Energy dissipation in substorms, *ESA, Substorms 1*. 1, 3

Whipple, E. C. (1981), Potentials of surfaces in space, *Rep. Prog. Phys.*, *44*(11), 1197–1250, doi:10.1088/0034-4885/44/11/002. 3.2.2

Wilken, B., Q. G. Zong, I. A. Daglis, T. Doke, S. Livi, K. Maezawa, Z. Y. Pu, S. Ullaland, and T. Yamamoto (1995), Tailward flowing energetic oxygen ion bursts associated with multiple flux ropes in the distant magnetotail: GEOTAil observations, *Geophys. Res. Lett.*, *22*(23), 3267–3270, doi:10.1029/95GL02980. 3.2.2

Wygant, J. R., C. A. Cattell, R. Lysak, Y. Song, J. Dombeck, J. McFadden, F. S. Mozer, C. W. Carlson, G. Parks, E. A. Lucek, A. Balogh, M. Andre, H. Reme, M. Hesse, and C. Mouikis (2005), Cluster observations of an intense normal component of the electric field at a thin reconnecting current sheet in the tail and its role in the shock-like acceleration of the ion fluid into the separatrix region, *J. Geophys. Res. Space Phys.*, *110*(A9), doi:10.1029/2004JA010708. 3.2.2, 3.2.3, 3.2.3

Xu, Y., H. S. Fu, C. Norgren, S. Toledo-Redondo, C. M. Liu, and X. C. Dong (2019), Ionospheric Cold Ions Detected by MMS Behind Dipolarization Fronts, *Geophys. Res. Lett.*, *46*(14), 7883–7892, doi:10.1029/2019GL083885. 3.2.2

Yamada, M. (1999), Review of controlled laboratory experiment on physics of magnetic reconnection, *J. Geophys. Res.*, *104*(A7), doi:10.1029/1998JA900169. 1

Yamada, M., R. Kulsrud, and H. Ji (2010), Magnetic reconnection, *Rev. Mod. Phys.*, *82*(1), 603–664, doi:10.1103/RevModPhys.82.603. 4

Yamada, M., J. Yoo, J. Jara-Almonte, W. Daughton, H. Ji, R. M. Kulsrud, and C. E. Myers (2015), Study of energy conversion and partitioning in the magnetic reconnection layer of a laboratory plasma, *Phys. Plasma*, *22*(5), 056,501, doi:10.1063/1.4920960. 3.5

Yau, A. W., and M. André (1997), Sources of Ion Outflow in the High Latitude Ionosphere, *Space Sci. Rev.*, *80*(1), 1–25, doi:10.1023/A:1004947203046. 3.2.2

Yau, A. W., E. G. Shelley, W. K. Peterson, and L. Lenchyshyn (1985), Energetic auroral and polar ion outflow at DE 1 altitudes: Magnitude, composition, magnetic activity dependence, and long-term variations, *J. Geophys. Res. Space Phys.*, *90*(A9), 8417–8432, doi:10.1029/JA090iA09p08417. 1

Yau, A. W., B. A. Whalen, C. Goodenough, E. Sagawa, and T. Mukai (1993), EXOS D (Akebono) observations of molecular NO+ and N2 + upflowing ions in the high-altitude auroral ionosphere, *J. Geophys. Res. Space Phys.*, *98*(A7), 11,205–11,224, doi:10.1029/92JA02019. 3.2.1

Young, D. T., H. Balsiger, and J. Geiss (1982), Correlations of magnetospheric ion composition with geomagnetic and solar activity, *J. Geophys. Res. Space Phys.*, *87*(A11), 9077–9096, doi:10.1029/JA087iA11p09077. 3.2.2, 3.2.2

Young, D. T., J. L. Burch, R. G. Gomez, A. De Los Santos, G. P. Miller, P. Wilson, N. Paschalidis, S. A. Fuselier, K. Pickens, E. Hertzberg, C. J. Pollock, J. Scherrer, P. B. Wood, E. T. Donald, D. Aaron, J. Furman, D. George, R. S. Gurnee, R. S. Hourani, A. Jacques, T. Johnson, T. Orr, K. S. Pan, S. Persyn, S. Pope, J. Roberts, M. R. Stokes, K. J. Trattner, and J. M. Webster (2016), Hot Plasma Composition Analyzer for the Magnetospheric Multiscale Mission, *Space Sci. Rev.*, *199*(1), 407–470, doi:10.1007/s11214-014-0119-6. 4.1.1

Zong, Q.-G., B. Wilken, J. Woch, T. Mukai, T. Yamamoto, G. D. Reeves, T. Doke, K. Maezawa, D. J. Williams, S. Kokubun, and S. Ullaland (1998), Energetic oxygen ion bursts in the distant magnetotail as a product of intense substorms: Three case studies, *J. Geophys. Res. Space Phys.*, *103*(A9), 20,339–20,363, doi: 10.1029/97JA01146. 3.2.2

Zou, Y., B. M. Walsh, X. Shi, L. Lyons, J. Liu, V. Angelopoulos, J. M. Ruohoniemi, A. J. Coster, and M. G. Henderson (2021), Geospace Plume and Its Impact on Dayside Magnetopause Reconnection Rate, *J. Geophys. Res. Space Phys.*, *126*(6), doi: 10.1029/2021JA029117. 3.2

Chapter 7

Scientific results

Paper I

Collisionless Magnetic Reconnection in an Asymmetric Oxygen Density Configuration

H.M. Kolstø, M. Hesse, C. Norgren, P. Tenfjord, S.F. Spinnangr, N. Kwagala

Geophysical Research Letters, Vol. 47, Issue 1 doi:10.1029/2019GL085359, 2020

Geophysical Research Letters

RESEARCH LETTER

10.1029/2019GL085359

Key Points:
- Alfvén scaling does not result in an adequate description of the reconnection rate due to the O^+ being demagnetized
- Scaling relation of reconnection rate for an asymmetrically distributed demagnetized species involves the average of the inflowing populations
- Significant asymmetry of the Hall electric field and the diffusion region

Correspondence to:
H. M. Kolstø,
hakon.kolsto@uib.no

Citation:
Kolstø H. M., Hesse M., Norgren C., Tenfjord P., Spinnangr S. F., & Kwagala N. (2020). Collisionless magnetic reconnection in an asymmetric oxygen density configuration. *Geophysical Research Letters*, *47*, e2019GL085359. https://doi.org/10.1029/2019GL085359

Received 13 SEP 2019
Accepted 2 DEC 2019
Accepted article online 3 JAN 2020

Collisionless Magnetic Reconnection in an Asymmetric Oxygen Density Configuration

Håkon Midthun Kolstø[1], Michael Hesse[1,2], Cecilia Norgren[1], Paul Tenfjord[1], Susanne Flø Spinnangr[1], and Norah Kwagala[1]

[1]Space Plasma Physics Group, University of Bergen, Bergen, Norway, [2]Southwest Research Institute, San Antonio, TX, USA

Abstract Combined with the magnetic field, the distribution of charged particles in the inflow region is expected to control the rate of magnetic reconnection. This paper investigates how the reconnection process is altered by a cold, asymmetrically distributed, oxygen population, which is initially located away from the current layer in the inflow regions. A particle-in-cell simulation is used to gain further insight into the dynamics of the system. The time evolution of the reconnection process proceeds rapidly compared to the cyclotron period of O^+. Therefore, the oxygen remains, to a good approximation, demagnetized. Thus, Alfvén scaling is not an adequate description of the reconnection rate. A scaling relation for the reconnection rate for an asymmetrically distributed, demagnetized species has been developed. Additionally, we find that an asymmetric density configuration leads to a distinct motion of the reconnection site and generates an asymmetry of the diffusion region and the Hall electric field.

1. Introduction

Magnetic reconnection is one of the most important energy release and transport processes in plasmas. In the Earth's magnetosphere, magnetic reconnection at the magnetopause is the primary mechanism responsible for the transport of energy, mass, momentum, and magnetic flux into Earth's magnetic cavity. Magnetic reconnection involves a violation of the ideal frozen-in condition (Vasyliunas, 1975), where the bulk motion of the particle species separates from the transport of magnetic flux.

In addition to the more abundant plasma species, that is, protons and electrons, heavier species, such as oxygen, may also be present in the plasma sheet as a result of ionospheric outflow (e.g., Baker et al., 1982; Chappell et al., 1987; Moore et al., 2001). The cold magnetotail oxygen originates from high-latitude ionosphere, and the ionospheric outflow rate is proportional to geomagnetic activity (Baker et al., 1982). Presence of oxygen of ionospheric origin in the Earth's magnetotail is supported by various observations (e.g., Frank et al., 1977; Grande et al., 2013; Moore et al., 2001; Mouikis et al., 2018; Wilken et al., 1995; Zong et al., 1998). Spacecraft observations reveal that oxygen may be the dominating ion species during storm time conditions (Kistler et al., 2005; Wygant et al., 2005a). At certain times, north-south asymmetries of ionospheric outflow may generate asymmetric oxygen inflow densities, and such asymmetries are also quite generically expected at the Earth's magnetopause (Li et al., 2013).

The inclusion of additional ion populations introduces distinctive kinetic behavior and different spatial and time scales for the system (Divin et al., 2016; Shay & Swisdak, 2004; Toledo-Redondo et al., 2015). The presence of heavy magnetized ions may result in a reduction of the Alfvén velocity, thus indicating a reduction of the reconnection rate (Hesse & Birn, 2004; Shay & Swisdak, 2004). Different mechanisms to slow down the reconnection rate have previously been proposed such as the effect of the tearing growth rate in the presence of O^+ (Karimabadi et al., 2011) and induced charge separation (i.e., *ambipolar* electric fields) (Liang et al., 2016, 2017). Previous studies (Tenfjord et al., 2018, 2019), investigated the effects of oxygen being symmetrically distributed in the inflow regions and proposed a scaling relation for the inclusion of a demagnetized species. Cluster reported density composition of $n_p = 0.03$ cm^{-3} and $n_{O^+} = 0.07$ cm^{-3} for protons and oxygen in the current sheet, respectively, (Wygant et al., 2005b) leading to a reduction of the reconnection rate of a factor of 6.3 through mass-loading effects and a factor of 3.3 for the proposed scaling relation (Tenfjord et al., 2019). During some phase of the evolution, this might imply that the dynamics of geomagnetic storms and substorms evolves twice as fast as expected when oxygen is present. This paper examines the effects on magnetotail reconnection imposed by an asymmetrically distributed oxygen population.

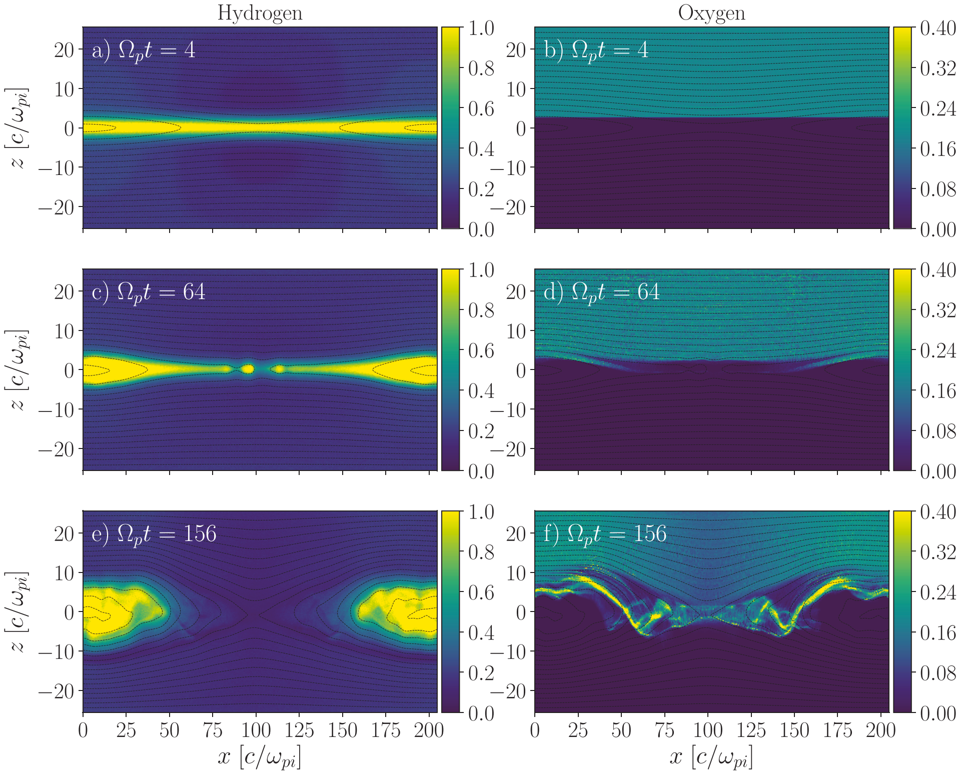

Figure 1. Time evolution for hydrogen (left: a, c, and e) and oxygen (right: b, d, and f) densities.

The outline of this paper is as follows: Section 2 will give an overview of the simulation setup employed for this study. Section 3 examines the evolution and dynamics of the reconnection site, for example, motion of x-point and the arising asymmetry of the diffusion region. Finally, in section 4 a scaling relation for an asymmetrically distributed, demagnetized, species is developed.

2. Simulation Setup

The analysis is performed by using a 2.5-D particle-in-cell (PIC) simulation, that is, two spatial components and three-fields and velocity components, designed to model the evolution of a current sheet subjected to asymmetric oxygen inflow. Initially, the configuration of the magnetic field is given as a two-dimensional generalized Harris-type equilibrium (see Hesse and Birn, 2004 for details) defined as $B_x = B_0 \tanh(z/\lambda)$, where $\lambda = 2d_p$ is the half width of the initial current sheet. The factor $d_p = c/\omega_{pi}(= c\sqrt{m_p/4\pi n_0 e^2})$ is the proton inertial length, where n_0 is the foreground density at the center of the initial current sheet.

In the upper inflow region (top lobe), oxygen O^+ is homogeneously distributed with a number density of $n_{O^+} = 0.2$ at a distance of $z > 2.5d_p$, where $z = 0$ is the initial location of the x-line (see Figure 1b). Density is normalized to n_0. Initially, the oxygen has zero thermal and bulk velocity. In addition to the oxygen, a uniform proton H^+ with a density of $n_b = 0.2$ is added to the Harris-sheet density configuration ($n_p = n_0/\cosh^2(z/2d_p) + n_b$) resulting in a peak density of 1.2 in the current layer.

The following mass ratios are employed: $m_p/m_e = 25$ for the protons/electrons and $m_{O^+}/m_p = 16$ for the oxygen/protons. A total of $4.8 \cdot 10^9$ macroparticles are used. Boundary conditions are periodic at $x = x_{\min}$

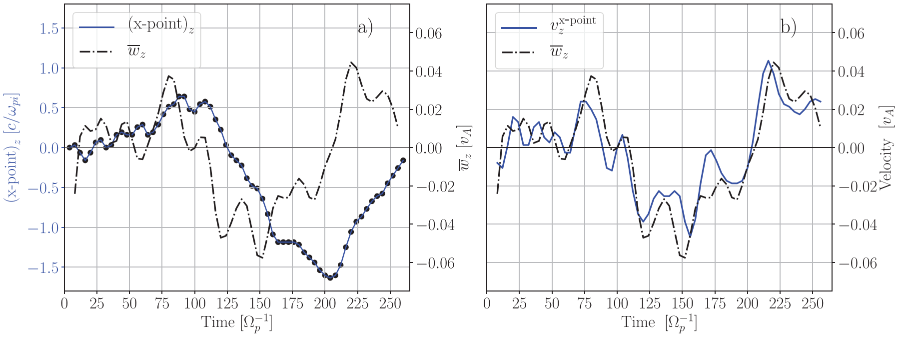

Figure 2. (a) Dynamics of the z-location of the x-point with respect to time shown by the blue dotted line and the average flux velocity shown by the black dash-dotted line. (b) Comparison of flux velocity (black dash-dotted) and velocity of the x-point (blue solid).

and $x = x_{\max}$. At $z = z_{\min}$ and $z = z_{\max}$, specular reflection is enabled and the out-of-plane electric field E_y is set to zero, preserving magnetic flux in the simulation domain.

Lengths are normalized to d_p, whereas time is normalized to the inverse of the proton cyclotron frequency $\Omega_p^{-1} = m_p/eB$. The size of our simulation domain is $200 \times 50\ d_p$ with a grid size of $3{,}200 \times 1{,}600$. We employ a time step of $\Omega_e \delta t = 0.5$. The velocity normalization is the proton Alfvén speed, based on the foreground current sheet density n_0. The foreground temperatures fulfill $T_p + T_e = 0.5$, in units of $[m_p v_A^2]$, derived from pressure balance

$$n_0(T_p + T_e) = \frac{B_0^2}{2}$$

with $n_0 = 1$ and $B_0 = 1$, and the ratio of proton-electron temperature is chosen to be $T_p/T_e = 5$. The ratio between the electron plasma frequency and gyrofrequency is $\omega_{pe}/\Omega_e = 2$.

3. Evolution and Dynamics of the Reconnection Site

In Figure 1, the O^+ and H^+ density are shown at three selected times. Close to the initial configuration, $\Omega_p t = 4$, oxygen is present in the inflow region only at a distance of $z > 2.5 d_p$. At $\Omega_p t = 64$ reconnection has initiated. However, the oxygen is still not present at the reconnection site. The reconnection rate peaks at $\Omega_p t = 80$, and an increasing amount oxygen is transported into the reconnection region, thus becoming present in the reconnection region. At $\Omega_p t = 156$ we observe horizontal layers of increased oxygen density close to the x-point. These striations form as a result of quasi-steady flow of oxygen from the inflow to the reconnection region (Tenfjord et al., 2018). Inclined oxygen density striations, which are evident at $\Omega_p t = 156$, are governed by the formation and expansion of the localized Hall electric field E_z. As the Hall electric field expands, oxygen particles at rest are collectively accelerated resulting in an oxygen density wave (Tenfjord et al., 2018).

3.1. Motion of the X-Point

The asymmetric oxygen distribution leads to distinct motion of the x-point across the initial x-line. The blue dotted line in Figure 2 shows the displacement of the x-point in the z direction with respect to time. We observe a shift of the x-point toward positive z, reaching a value of $z = 0.7 d_p$. From $\Omega_p t > 120$ the x-point moves in the negative z direction, reaching its minimum at $z = -1.7 d_p$. Close to the end of the simulation, the x-point moves toward its initial value. The two processes governing the shift toward positive and negative z values are distinct. We now examine them further.

We start by investigating how the shift of the x-point relates to the differences in the flux velocity between the top and bottom lobe. The motion of the magnetic flux in z direction is determined by finding the frame in which $\frac{\mathrm{d}A_y}{\mathrm{d}t} = 0$. This leads to the magnetic flux velocity w_z

Geophysical Research Letters 10.1029/2019GL085359

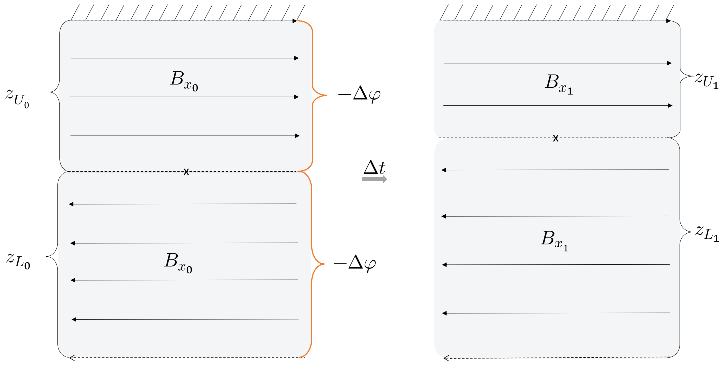

Figure 3. Reconnection site before (after) reconnection has initiated on left (right). The oxygen front is illustrated by the wall, hindering the replenishment of magnetic field lines.

$$\frac{\mathrm{d}A_y}{\mathrm{d}t} = \frac{\partial A_y}{\partial t} + w_z \frac{\partial A_y}{\partial z} = 0$$

which gives

$$w_z = -\left(\frac{\partial A_y}{\partial t}\right) / \left(\frac{\partial A_y}{\partial z}\right)$$

In order to investigate the correlation between the magnetic flux velocity and the actual velocity of the x-point, we average w_z throughout the simulation domain, excluding the diffusion region.

The velocity of the x-point should match any differences of the flux velocities in these two regions. The average flux velocity $\overline{w}_z$, shown in Figure 2, would be zero if the flux were transported in a convergent manner in the top and bottom lobes. The velocity of the x-point, $v_z^{\text{x-point}}(= \Delta z^{\text{x-point}}/\Delta t)$ (blue line) displays a rather good agreement with the average flux velocity $\overline{w}_z$, indicating that $v_z^{\text{x-point}}$ is dictated by the differences of w_z in the two inflow regions.

The difference in the magnetic flux velocities between the two inflow regions is attributed to a drag imposed by the higher inertia of the oxygen species. As the far more agile electrons move with the magnetic field, an (ambipolar) electric field is set up to prevent charge separation (Karimabadi et al., 2011; Liang et al., 2016). The resulting electric field impedes the transport of magnetic flux from the top lobe. However, in the lower inflow region, the absence of oxygen lets the electrons and protons move, to a higher extent, unencumbered toward the x-line.

The limited flux mobility in the region covered by cold oxygen results in an upward movement of the current layer. This can be shown analytically by approximating the oxygen region as nearly stationary such that the flux velocity and the overall plasma bulk velocity is much smaller here than elsewhere. The different regions of flux mobility above and below are indicated by z_U and z_L, see Figure 3. If magnetic reconnection removes the same amount of flux $\Delta\varphi$ from the upper region and the lower region, force balance requires that the current layer moves upward to keep the magnetic pressure equal on both sides. At a time t_1, indicated by the subscript, the flux contained in the two regions can be written as

$$B_{x_1} z_{U_1} = B_{x_0} z_{U_0} - \Delta\varphi \tag{1}$$

$$B_{x_1} z_{L_1} = B_{x_0} z_{L_0} - \Delta\varphi \tag{2}$$

where the numbered subscripts refer to the times of evaluation, t_0 and t_1. The length of the combined regions are to be remained constant, thus

$$z_{U_1} + z_{L_1} = z_{U_0} + z_{L_0} \tag{3}$$

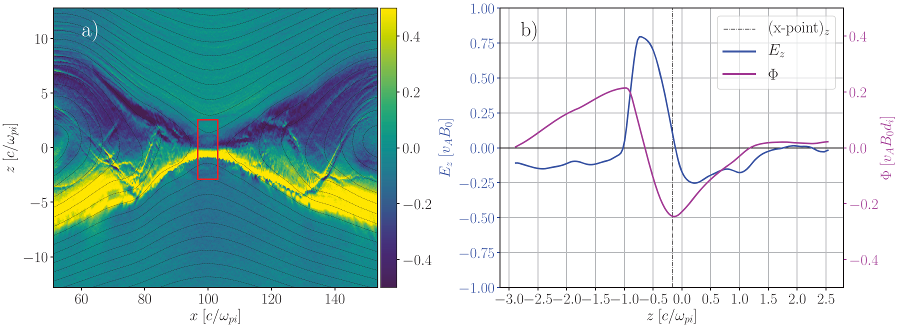

Figure 4. Asymmetry in the Hall electric field E_z at $\Omega_p t = 132$. E_z and Φ are evaluated inside the red box shown panel (a). The dashed line shows the z-location of the x-point for this time step.

Combining equations (1)–(3), the change in length of the upper and lower regions can now be expressed as

$$z_{U_1} - z_{U_0} = \frac{\Delta\varphi}{B_{x_1}}\left[\frac{2z_{U_0}}{z_{U_0} + z_{L_0}} - 1\right] < 0, \quad \text{as} \quad 2z_{U_0} < z_{U_0} + z_{L_0} \tag{4}$$

$$z_{L_1} - z_{L_0} = \frac{\Delta\varphi}{B_{x_1}}\left[\frac{2z_{L_0}}{z_{U_0} + z_{L_0}} - 1\right] > 0, \quad \text{as} \quad 2z_{L_0} > z_{U_0} + z_{L_0} \tag{5}$$

Equations (4) and (5) imply that the x-point shifts to positive values of z. In order to reach equilibrium, the upper region needs to be compressed and the lower region expanded, leading to an upward motion of the current layer (see Figure 3).

The x-point reaches its highest value at $\Omega_p t = 88$ and is thereafter shifted toward negative z due to a different process. The Hall electric field E_z extends into the upper lobe and accelerates the demagnetized oxygen toward the x-point, resulting in an increase of the dynamic oxygen pressure. At this point the oxygen no longer imposes a drag on the transport of magnetic flux, but instead contributes to an increase of w_z as a result of its enhanced dynamic pressure, see Figure 5. An overall higher w_z on the oxygen side, compared to the southern lobe, shifts the x-point to negative z-values. In the next section we will see how the increase of the dynamic pressure affects the diffusion region.

3.2. Asymmetry of the Diffusion Region

As the oxygen gets involved in the reconnection process, an asymmetry in the diffusion region arises. Figure 4 shows an overview of the Hall electric field and its potential. Figure 4a shows the structure of the Hall E_z, and in Figure 4b a clear asymmetry across the diffusion region is evident.

To investigate the asymmetry of the Hall electric field E_z we start by examining the pressure balance along z through the x-point. We obtain

$$P^o_{zz} + P^p_{zz} + P^e_{zz} + m_{O^+} n^{avg}_{O^+} v^2{}_{O^+z} + \frac{B_x^2}{2\mu_0} \sim C \tag{6}$$

Equation (6) only includes the dominant contributions (shown for $\Omega_p t = 132$ in Figure 5) where C is a constant, and $n^{avg}_{O^+}$ is the average oxygen density. In Figure 5, we see that the contribution to the overall pressure balance of the dynamic and thermal pressures for both oxygen and protons are substantially higher in the northern lobe than in the southern lobe. On the $z > 0$ side a clear reduction of the gradient of the magnetic pressure is seen. Additionally, asymmetries in the dynamic oxygen pressure and the thermal pressure of both the oxygen and protons are found.

Due to acceleration of oxygen by the Hall electric field, the dynamic oxygen pressure increases and a reduction of the magnetic pressure arises to preserve the pressure balance. The higher contribution of the pressure terms from the plasma species in the northern lobe suppresses the contribution of the magnetic pressure

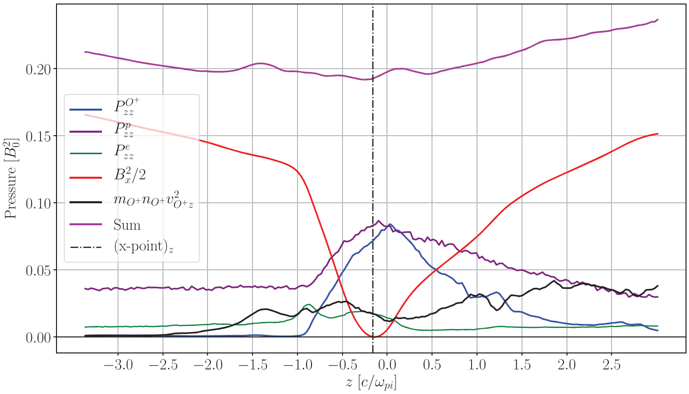

Figure 5. Pressure balance through x-point along z taken at time $\Omega_p t = 132$.

to preserve the pressure balance. The immediate effect of this is the broadening of the B_x profile which, through Ampères law $\mu_0 j_y \sim \partial/\partial_z B_x$, leads to a reduced current density. The reduction in the magnetic field strength results in a decrease of E_z in the northern lobes through Ohm's law.

In the region shown in Figure 5, the current is, to a good approximation, mainly carried by the far more agile electrons. We may therefore write the Hall electric field in the following manner

$$E_z \sim v_{ey} B_x \sim \frac{j_y}{n_e} B_x \sim \frac{1}{\mu_0 n_e} \left(\frac{\partial B_x}{\partial z} \right) B_x$$

which may be written, in terms of the magnetic pressure, in the following way

$$E_z \sim \frac{1}{n_e} \frac{\partial}{\partial z} \left(\frac{B_x^2}{2\mu_0} \right) \tag{7}$$

From equation (7) we see that the Hall electric field is directly dependent on the gradient of the magnetic pressure. Thus, on the oxygen side, the flatter profile of the magnetic pressure results in a smaller gradient and thereby reducing the Hall electric field.

4. Scaling of the reconnection rate

In this section we evaluate how the reconnection rate scales for asymmetrically distributed oxygen. There are several reasons to expect that the aforementioned configuration would affect the reconnection rate. Being under the influence of oxygen, we have seen that the flux velocity is reduced in the top lobe compared to the bottom lobe. Furthermore, the cyclotron period of the oxygen species is much longer than the characteristic time scale of the reconnection process (Ω_p^{-1}), oxygen is therefore mainly influenced by electric forces. This can also be seen in Tenfjord et al. (2018), where a similar simulation setup is employed.

Mass loading effects predict a reduction in the reconnection rate that scales as the total Alfvén velocity, that is, $\sqrt{(m_{\mathrm{O}^+} n_{\mathrm{O}^+} / m_p n_p + 1)}$. However, Tenfjord et al. (2019) investigated how the reconnection rate scales in the presence of demagnetized oxygen and found that the reconnection rate was reduced much less. Performing a scaling analysis similar to that of Tenfjord et al. (2019) leads to a relation for the reconnection rate in the presence of an asymmetrically distributed oxygen density. The Hall electric field for the protons scales in the following manner

$$E_z \sim \frac{1}{q n_p} \frac{\partial}{\partial z} P_{zz}^p \sim \frac{1}{q n_p} \frac{P_{zz}^p}{L_{\mathrm{Hall}}} \sim \frac{E_y}{\beta}$$

The factor β is a proportionality constant relating the off-diagonal pressure components to the diagonal components. We have here assumed that off-diagonal pressure components shows a linear dependence on

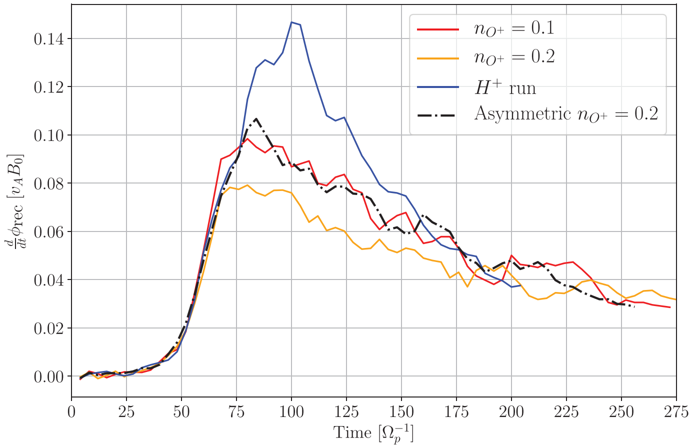

Figure 6. Comparison of the reconnection rates for runs with different oxygen densities. Clear agreement between the asymmetric oxygen density configuration (dash-dotted) $n_{\mathrm{O}^+} = 0.2$ run and the symmetric oxygen density configuration (red) $n_{\mathrm{O}^+} = 0.1$ run.

the trace of pressure tensor (Tenfjord et al., 2019). Similarly for the electrons

$$P^e_{zz} \sim qn_e L_{\mathrm{EDR}} \frac{E_y}{\alpha}$$

The acceleration of O$^+$ from one side leads to a bulk motion of oxygen inside the diffusion region. This expression differs from what used in Tenfjord et al. (2019), where O$^+$ existed in both lobes leading to two counterstreaming populations which manifested as pressure. For the oxygen species, the Hall electric field scales as

$$E_z \sim \frac{1}{qn^{\mathrm{avg}}_{\mathrm{O}^+}} \frac{\partial}{\partial z}(P^o_{zz} + m_{\mathrm{O}^+} n^{\mathrm{avg}}_{\mathrm{O}^+} v^2{}_{\mathrm{O}^+ z}) \sim \frac{1}{qn_{\mathrm{O}^+}} \frac{P^o_{zz} + m_{\mathrm{O}^+} n^{avg}_{\mathrm{O}^+} v^2_{\mathrm{O}^+ z}}{L_{Hall}}$$

Substituting the derived pressure relations into equation (6) gives

$$\frac{B_x^2}{2\mu_0} + qn_p L_{\mathrm{Hall}} \frac{E_y}{\beta} + q(n_p + n^{\mathrm{avg}}_{\mathrm{O}^+})L_{\ \mathrm{EDR}} \frac{E_y}{\alpha} + qn^{\mathrm{avg}}_{\mathrm{O}^+} L_{\ \mathrm{Hall}} \frac{E_y}{\beta} \sim C$$

Writing out the average oxygen density to relate the density of the upper $n^U_{\mathrm{O}^+}$ and lower $n^L_{\mathrm{O}^+}$ lobes as $n^{\mathrm{avg}}_{\mathrm{O}^+} = \frac{1}{2}(n^U_{\mathrm{O}^+} + n^L_{\mathrm{O}^+})$ we get

$$E_y \left[e \left(\frac{L_{\mathrm{Hall}}}{\beta} - \frac{L_{\mathrm{EDR}}}{\alpha} \right) \left(n_p + \frac{n^U_{\mathrm{O}^+} + n^L_{\mathrm{O}^+}}{2} \right) \right] \sim C - \frac{B_x^2}{2\mu_0}$$

Neither the right-hand side, the scale lengths, nor the proportionality constants, α and β, depends on the oxygen density. This leads us to express the scaling relation of the reconnection electric field as a function of the oxygen and proton density

$$E_y \sim (1 + \frac{n^U_{\mathrm{O}^+} + n^L_{\mathrm{O}^+}}{2n_p})^{-1} \tag{8}$$

In Figure 6, we compare the reconnection rate, which can be expressed as $\frac{\mathrm{d}}{\mathrm{d}t}\phi_{\mathrm{rec}} = \int E_y \mathrm{d}y$, to numerical simulations, hereafter referred to as runs, of different oxygen densities. The oxygen species are initially a distance of $2.5d_p$ from the x-line for the three oxygen runs. The reconnection rate of the symmetric density configuration of $n_{\mathrm{O}^+} = 0.1$ (red) (Tenfjord et al., 2019) displays a good agreement with the asymmetric density configuration of $n_{O^+} = 0.2$ (dash-dotted line). The blue solid line represents a run with absence of oxygen.

The scaling relation in equation (8) coincides with the reconnection rates as seen in Figure 6. All runs follow the same evolution toward the peak of the reconnection rate. This indicates that an increase of the density reduces the maximum value of the reconnection rate and not the rate at which it reaches its peak. This implies that the reconnection rate is determined by the oxygen content and not its initial configuration.

5. Discussion and Summary

Our results provide insight into the rate reconnection actually proceeds with. It further provides a generalization of the estimated reconnection rate when the plasma system includes heavier species in addition to the protons and electrons. This generalization is valid when heavier ion species are distributed asymmetrically, and such scenarios may occur for ionospheric outflow, for example, when the Northern Hemisphere is illuminated, and the Southern Hemisphere is in darkness. The smaller gyrofrequency of the O^+ introduces longer coupling time scales. Therefore, the oxygen is largely demagnetized on the time scales of this investigation and Alfvén scaling of the reconnection rate does not apply in our model. It should be noted that steady state reconnection lasting for a significantly longer time would be expected to magnetize the oxygen at some point, and Alfvén scaling may apply for these cases. Through pressure balance arguments, we succeeded in extending previous results (Tenfjord et al., 2018) to derive a scaling relation for the reconnection rate for an asymmetrically distributed, demagnetized, species.

The reconnection rate during the fast phase shows no dependency on the oxygen density. We have seen that reduction of the reconnection rate is dependent on the overall content of the demagnetized species and not its initial configuration. The initial temperature of oxygen is chosen to be zero to isolate oxygen inertia on the reconnection process from other effects, such as streaming and finite temperature. In Tenfjord et al. (2019) it was shown that an initial temperature of the O^+ has no significant effect on the reconnection rate. The additional effects arising from an asymmetric oxygen population, such as asymmetric E_z, bulk z-directed oxygen velocity in the diffusion region and motion of x-point, does not appear to have any significant effect on the reconnection rate.

Regarding observations, signatures as the oxygen striations seen in Figure 1 and asymmetries in the Hall fields should be detectable. The results obtained in this study may apply to magnetotail reconnection in case of north-south asymmetries of ionospheric outflow. In addition, they may play a role in reconnection at the magnetopause, even though many effects may be masked by the typical and often rather large asymmetries across the current layer. They may further apply to laboratory devices and other reconnection geometries, where either history or asymmetric particle injection may lead to similarly asymmetric situations. Regarding space applications, we hope our results provide useful insight for future analysis of space mission data, in particular, the Magnetospheric Multiscale mission.

Acknowledgments
This study was supported by the Research Council of Norway/CoE University of Bergen, by NOTUR/NORSTOR under project NN9496K, and by NASA's MMS mission. Data set used in this analysis is available at (Kolstø, 2019).

References

Baker, D. N., Hones, E. W., Young, D. T., & Birn, J. (1982). The possible role of ionospheric oxygen in the initiation and development of plasma sheet instabilities. *Geophysical Research Letters*, *9*(12), 1337–1340. https://doi.org/10.1029/GL009i012p01337

Chappell, C. R., Moore, T. E., & Waite, J. H. (1987). The ionosphere as a fully adequate source of plasma for the Earth's magnetosphere. *Journal of Geophysical Research*, *92*(A6), 5896–5910. https://doi.org/10.1029/JA092iA06p05896

Divin, A., Khotyaintsev, Y. V., Vaivads, A., André, M., Toledo-Redondo, S., Markidis, S., & Lapenta, G. (2016). Three-scale structure of diffusion region in the presence of cold ions. *Journal of Geophysical Research: Space Physics*, *121*, 12,001–12,013. https://doi.org/10.1002/2016JA023606

Frank, L. A., Ackerson, K. L., & Yeager, D. M. (1977). Observations of atomic oxygen (O^+) in the Earth's magnetotail. *Journal of Geophysical Research*, *82*, 129–134. https://doi.org/10.1029/JA082i001p00129

Grande, M., Perry, C. H., Hall, A., Fennell, J., Nakamura, R., & Kamide, Y. (2013). What is the Effect of Substorms on the Ring Current Ion Population During a Geomagnetic Storm? *American Geophysical Union (AGU)*, 75–89. https://doi.org/10.1029/142GM08

Hesse, M., & Birn, J. (2004). On the cessation of magnetic reconnection. *Annales de Geophysique*, *22*(2), 603–612. https://doi.org/10.5194/angeo-22-603-2004

Karimabadi, H., Roytershteyn, V., Mouikis, C. G., Kistler, L. M., & Daughton, W. (2011). Flushing effect in reconnection: Effects of minority species of oxygen ions. *Planetary and Space Science*, *59*(7), 526–536. https://doi.org/10.1016/j.pss.2010.07.014

Kistler, L. M., Mouikis, C., Möbius, E., Klecker, B., Sauvaud, J. A., Réme, H., et al. (2005). Contribution of nonadiabatic ions to the cross-tail current in an O^+ dominated thin current sheet. *Journal of Geophysical Research*, *110*, A06213. https://doi.org/10.1029/2004JA010653

Kolstø H. M. (2019). Replication data for: Collisionless Magnetic Reconnection in an Asymmetric Oxygen Density Configuration, https://doi.org/10.18710/4YHU4R

Li, K., Haaland, S., Eriksson, A., André, M., Engwall, E., Wei, Y., et al. (2013). Transport of cold ions from the polar ionosphere to the plasma sheet. *Journal of Geophysical Research: Space Physics*, *118*, 5467–5477. https://doi.org/10.1002/jgra.50518

Liang, H., Ashour-Abdalla, M., Lapenta, G., & Walker, R. J. (2016). Oxygen impacts on dipolarization fronts and reconnection rate. *Journal of Geophysical Research: Space Physics*, *121*, 1148–1166. https://doi.org/10.1002/2015JA021747

Liang, H., Lapenta, G., Walker, R. J., Schriver, D., El-Alaoui, M., & Berchem, J. (2017). Oxygen acceleration in magnetotail reconnection. *Journal of Geophysical Research: Space Physics*, *122*, 618–639. https://doi.org/10.1002/2016JA023060

Moore, T. E., Chandler, M. O., Fok, M.-C., Giles, B. L., Delcourt, D. C., Horwitz, J. L., & Pollock, C. J. (2001). Ring Currents and Internal Plasma Sources. *Space Science Reviews*, *95*(1/2), 555–568. https://doi.org/10.1023/A:1005264907107

Mouikis, C. G., Kistler, L. M., Liu, Y. H., Klecker, B., Korth, A., & Dandouras, I. (2018). H^+ and O^+ content of the plasma sheet at 15–19 Re as a function of geomagnetic and solar activity. *Journal of Geophysical Research: Space Physics*, *115*, A00J16. https://doi.org/10.1029/2010JA015978

Shay, M. A., & Swisdak, M. (2004). Three-Species Collisionless Reconnection: Effect of O^+ on Magnetotail Reconnection. *Physical Review Letters*, *93*, 175001. https://doi.org/10.1103/PhysRevLett.93.175001

Tenfjord, P., Hesse, M., & Norgren, C. (2018). The Formation of an Oxygen Wave by Magnetic Reconnection. *Journal of Geophysical Research: Space Physics*, *123*, 9370–9380. https://doi.org/10.1029/2018JA026026

Tenfjord, P., Hesse, M., Norgren, C., Spinnangr, S. F., & Kolstø, H. (2019). The impact of oxygen on the reconnection rate. *Geophysical Research Letters*, *46*, 6195–6203. https://doi.org/10.1029/2019GL082175

Toledo-Redondo, S., Vaivads, A., André, M., & Khotyaintsev, Y. V. (2015). Modification of the Hall physics in magnetic reconnection due to cold ions at the Earth's magnetopause. *Geophysical Research Letters*, *42*, 6146–6154. https://doi.org/10.1002/2015GL065129

Vasyliunas, V. M. (1975). Theoretical models of magnetic field line merging. *Reviews of Geophysics*, *13*(1), 303–336. https://doi.org/10.1029/RG013i001p00303

Wilken, B., Zong, Q. G., Daglis, I. A., Doke, T., Livi, S., Maezawa, K., et al. (1995). Tailward flowing energetic oxygen ion bursts associated with multiple flux ropes in the distant magnetotail: GEOTAil observations. *Geophysical Research Letters*, *22*(23), 3267–3270. https://doi.org/10.1029/95GL02980

Wygant, J. R., Cattell, C. A., Lysak, R., Song, Y., Dombeck, J., McFadden, J., et al. (2005a). Cluster observations of an intense normal component of the electric field at a thin reconnecting current sheet in the tail and its role in the shock-like acceleration of the ion fluid into the separatrix region. *Journal of Geophysical Research*, *110*, A09206. https://doi.org/10.1029/2004JA010708

Wygant, J. R., Cattell, C. A., Lysak, R., Song, Y., Dombeck, J., McFadden, J., et al. (2005b). Cluster observations of an intense normal component of the electric field at a thin reconnecting current sheet in the tail and its role in the shock-like acceleration of the ion fluid into the separatrix region. *Journal of Geophysical Research*, *110*, A09206. https://doi.org/10.1029/2004JA010708

Zong, Q.-G., Wilken, B., Woch, J., Mukai, T., Yamamoto, T., Reeves, G. D., et al. (1998). Energetic oxygen ion bursts in the distant magnetotail as a product of intense substorms: Three case studies. *Journal of Geophysical Research*, *103*(A9), 20,339–20,363. https://doi.org/10.1029/97JA01146

Paper II

On the Impact of a Streaming Oxygen Population on Collisionless Magnetic Reconnection

H.M. Kolstø, M. Hesse, C. Norgren, P. Tenfjord, S.F. Spinnangr, N. Kwagala

Geophysical Research Letters, Vol. 47, Issue 22 doi:10.1029/2020GL089462, 2020

Geophysical Research Letters

RESEARCH LETTER
10.1029/2020GL089462

On the Impact of a Streaming Oxygen Population on Collisionless Magnetic Reconnection

Håkon Midthun Kolstø[1], **Michael Hesse**[1,2], **Cecilia Norgren**[1], **Paul Tenfjord**[1], **Susanne Flø Spinnangr**[1], **and Norah Kwagala**[1]

[1]Space Plasma Physics Group, University of Bergen, Bergen, Norway, [2]NASA Ames Research Center, CA, USA

Key Points:
- Tailward motion of the X-point is generated even though the oxygen is demagnetized
- The oxygen couples to the magnetic flux through electrostatic coupling with the electrons
- The momentum of the streaming oxygen does not affect the reconnection rate

Correspondence to:
H. M. Kolstø,
hakon.kolsto@uib.no

Citation:
Kolstø, H. M., Hesse, M., Norgren, C., Tenfjord, P., Spinnangr, S. F., & Kwagala, N. (2020). On the impact of a streaming oxygen population on collisionless magnetic reconnection. *Geophysical Research Letters*, *47*, e2020GL089462. https://doi.org/10.1029/2020GL089462

Received 22 JUN 2020
Accepted 21 OCT 2020
Accepted article online 29 OCT 2020

Abstract Using 2.5-D Particle-In-Cell (PIC) simulations, we investigate how magnetotail reconnection is affected by a cold, streaming, oxygen plasma population, attributed to an ionospheric source, in the inflow region. As the tailward streaming oxygen reaches the current layer, a tailward motion of the reconnection site is induced. Due to the much longer cyclotron period of the oxygen ions, oxygen cannot couple as directly into the reconnection dynamics as protons. We find that the oxygen ions couple indirectly by means of impacting the electron dynamics. Therefore, a demagnetized species can, in fact, alter the dynamics of the reconnection site. We see further that the reconnection rate remains unchanged relative to a nonstreaming run. Our results may prove useful for understanding the development and dynamics of magnetospheric substorms and storms.

1. Introduction

Magnetic reconnection is one of the primary energy conversion and transport mechanisms in space plasmas. It converts stored electromagnetic energy to thermal and kinetic energy of the plasma particles and is the motor behind large-scale phenomena such as particle acceleration, momentum, and magnetic flux transport throughout the magnetosphere and beyond. In order for reconnection to take place, the frozen-in condition needs to be violated (Vasyliunas, 1975); that is, the bulk motion of the electrons should decouple from the transport of magnetic flux.

In the plasma sheet, abundant species such as protons and electrons may at certain times be accompanied by heavier species as, for example, O^+ (Baker et al., 1982; Chappell et al., 1987; Moore et al., 2001). The presence of oxygen ions whose origin is from the high-latitude ionosphere has been observed in the Earth's magnetotail (Frank et al., 2012; Grande et al., 2013; Mouikis et al., 2018; Moore et al., 2001; Wilken et al., 1995; Zong et al., 1998), and the ionospheric outflow rate is proportional to geomagnetic activity (Baker et al., 1982). Spacecraft observations by Cluster reveal that O^+ may be the dominating ion species during storm time conditions (Kistler et al., 2005; Wygant et al., 2005). The GEOTAIL spacecraft observed bursts of tailward streaming oxygen ions of ionospheric origin in the magnetotail with a peak of the velocity distribution function (VDF) at 1,700 km/s (Wilken et al., 1995).

In this paper we investigate how the reconnection process is affected by a streaming oxygen population. Previous studies have shown that tailward streaming protons lead to a tailward motion of the X-point (Tenfjord et al., 2020). While the temperature of the inflow population does not seem to play a major role for the reconnection rate (Dargent et al., 2020; Divin et al., 2016; Tenfjord et al., 2019), its mass density does (Kolstø et al., 2020; Tenfjord et al., 2019). The inclusion of additional ion species has been shown to result in distinct spatial and time scales for the reconnection process (Divin et al., 2016; Shay & Swisdak, 2004; Toledo-Redondo et al., 2015). Compared to protons, the oxygen ions have a much larger cyclotron period, and thus, their coupling to the magnetic flux is less evident. Throughout the times of investigation, the oxygen ions in this simulation remain demagnetized. We here report on the effect a demagnetized streaming oxygen species has on the reconnection process.

The outline of this paper is as follows: Section 2 gives an overview of the simulation setup employed for this investigation. Section 3 examines the motion of the X-point, the evolution of the reconnection process, and the associated distribution functions. Finally, in section 4, we investigate how the reconnection rate is affected.

2. Simulation Setup

The analysis is performed by employing a 2.5-D Particle-In-Cell (PIC) simulation, that is, two spatial components and three field and velocity components, designed to model the magnetotail conditions during a burst of ionospheric oxygen outflow. The coordinate system is as follows: x is the reconnection outflow direction, y is the current direction, and z is the inflow direction. Initially, the magnetic field configuration is given by a generalized Harris-type equilibrium defined as $B_x = B_0 \tanh(z/\lambda)$, where $\lambda = 2d_p$ is the half width of the initial current sheet and $d_p = c/\omega_{pi}(= c\sqrt{m_p/4\pi n_0 e^2})$ is the proton inertial length. Densities are normalized to the foreground density at the center of the initial current sheet n_0.

A uniform proton distribution with a density of $n_b = 0.2$ is added to the initial Harris sheet density configuration $n_p = n_0/\cosh^2(z/2d_p)$ resulting in a peak density of 1.2 in the current layer. The protons initially have no x-directed bulk velocity. Oxygen ions are distributed homogeneously above a specific field line, corresponding to a distance of $|z| > 3d_p$ from the current sheet. The O^+ has initially zero thermal velocity but an x-directed bulk velocity of $v_x^{O^+} = 0.5v_A$, where v_A is the proton Alfvén velocity. The electrons associated with the oxygen ions have the same initial bulk velocity, that is, $v_x^e = 0.5v_A$, whereas the electrons initially accompanying the protons are stationary. When referring to tailward streaming O^+ of ionospheric origin, this setup presumes that the oxygen ions has been preaccelerated to move in the x-direction.

The following mass ratios are employed: $m_p/m_e = 25$ for the protons/electrons and $m_{O^+}/m_p = 16$ for the oxygen/protons. A total of $\sim 10^{10}$ macroparticles is used. Boundary conditions are periodic at $x = x_{min}$ and $x = x_{max}$. At $z = z_{min}$ and $z = z_{max}$, specular reflection is enabled and the out-of-plane electric field E_y is set to zero, preserving magnetic flux in the simulation domain.

Lengths are normalized to d_p, whereas time is normalized to the inverse of the proton cyclotron frequency $\Omega_p^{-1} = m_p/eB$. The size of our simulation domain is $410d_p \times 50d_p$ with a grid size of $6{,}400 \times 1{,}600$. We employ a time step of $\omega_{pe}\delta t = 0.5$. The velocity normalization is the proton Alfvén speed, based on the foreground current sheet density n_0. The foreground temperatures fulfill $T_p + T_e = 0.5$, in units of $(m_p v_A^2)$, derived from pressure balance $n_0(T_p + T_e) = \frac{B_0^2}{2}$ with $n_0 = 1$ and $B_0 = 1$, and the ratio of proton-electron temperature is chosen to be $T_p/T_e = 5$. The ratio between the electron plasma frequency and gyrofrequency is $\omega_{pe}/\Omega_e = 2$.

3. Motion of the Reconnection Site

Figure 1a shows the time evolution of the x-location of the X-point. Initially, the X-point is located at $x = 205d_p$. At $\Omega_p t = 50$, the X-point shows an earthward displacement due to the formation of an island. It is not until the oxygen ions reach the reconnection site at $\Omega_p t \approx 120$ that the X-point starts to move in the positive x-direction. When the oxygen density at the reconnection site is of significance, the X-point moves at the center-of-mass velocity, given by

$$v_c = \frac{\sum_i M_i v_{ix}}{\sum_i M_i} = 0.45, \quad \text{where} \quad M_i = m_i \int n_i \mathrm{d}x\mathrm{d}z \tag{1}$$

where the summation index i sums over all three species in the simulation domain and M_i is the total mass of the respective species. The oxygen ions are the main contributor to v_c due to their much higher momentum as compared to the other species.

The motion of the X-point is associated with a gradient of the y-component of the electric field by virtue of Faraday's law. As the oxygen ions are the drivers of the X-point motion, we investigate how E_y is supported by O^+, through Ohm's law, given by

$$E_y = m_{O^+}\left(\frac{\partial}{\partial t}v_y^{O^+} + \vec{v}_{O^+} \cdot \nabla v_y^{O^+}\right) + v_x^{O^+}B_z - v_z^{O^+}B_x + \frac{1}{n_{O^+}}\nabla \cdot \mathbf{P}^{O^+} \cdot \hat{y}$$

In Figure 1b, we see a clear gradient of E_y in the vicinity of the X-point. The finite gradient $\partial E_y/\partial x > 0$ results in a local decrease of the magnetic field as $\partial B_z/\partial t < 0$, leading to a tailward shift of the X-point. Furthermore, we see that E_y is sustained by a variety of contributors of comparable size, such as the Lorentz term and the inertia and pressure terms. Hence, the oxygen ions are not $\vec{E} \times \vec{B}$ drifting and thus not frozen-in. In Figure 1c, to the right of the X-point, we see that the oxygen density enhancement moves close to the magnetic flux velocity, even though the O^+ does not exhibit a magnetized behavior. This apparent motion of the O^+ density enhancement is strongly influenced by the z-motion of the oxygen ions.

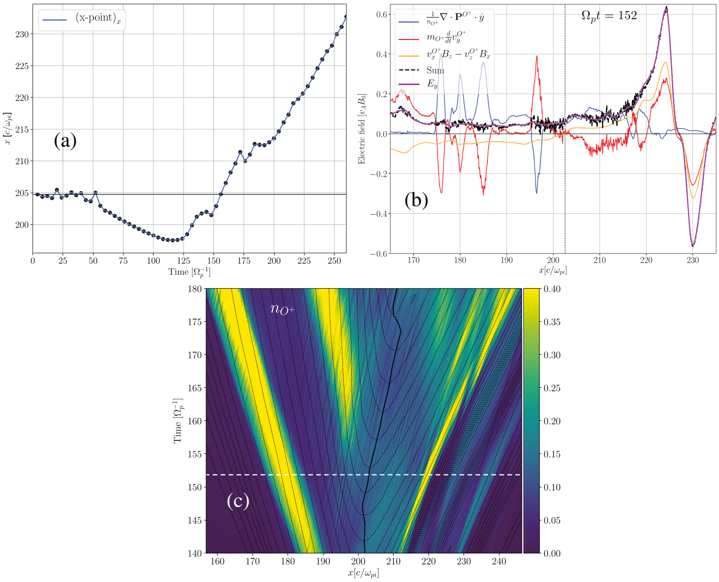

Figure 1. (a) Time of evolution of the x-location of the X-point showing its clear x-directed motion. (b) The y-component of Ohm's law for O^+. The vertical black dotted line is the location of the X-point. The black dotted line denotes the sum of the terms adding up to E_y. (c) A cut through the X-point along x following how the oxygen ion density evolves as a function of time. The color map shows n_{O^+}, the dotted line shows the contours of the magnetic vector potential A_y, defined by $\vec{B} = \nabla\vec{A}\times\hat{y} + B_y\hat{y}$, and the solid black line is the X-point location. This shows that the motion of the oxygen density enhancement moves close to the magnetic flux velocity. The white dotted horizontal line in (c) shows the time where the y-component of Ohm's law for O^+, in panel (b), is evaluated.

Since the velocity of the X-point is essentially determined by O^+, some mechanism must allow the oxygen ions to deliver their momentum to the magnetic flux tubes. As the electrons are well magnetized, we propose that there must be a coupling between O^+ and e^-. We speculate that this alignment may result from electrostatic coupling between O^+ and e^-, which enables an indirect coupling of the oxygen ions to the magnetic field. In the next section we explore how such a coupling occurs.

3.1. Electrostatic Coupling Between O^+ and e^-

Even though the oxygen ions are not $\vec{E}\times\vec{B}$ drifting, they move close to the magnetic flux velocity as seen in the local density enhancement to the right of the X-point in Figure 1c. In Figure 2a, we see the frozen-in behavior of the electrons, as $E_y \approx v_x^e B_z$ which implies that the magnetic flux is moving with the electrons as $v_z^e B_x \approx 0$. This is suggestive of some underlying mechanism, which enables the coupling between the oxygen ions and the electrons. We investigate this by evaluating the electron momentum equation, given by

$$m_e n_e\left(\frac{\partial}{\partial t}\vec{v}_e + \vec{v}_e\cdot\nabla\vec{v}_e\right) = -n_e(\vec{v}_e\times\vec{B}+\vec{E}) - \nabla\cdot\mathbf{P}^e$$

across the local density enhancement, indicated by the peak of n_e and n_{O^+} occurring at $x\approx 218d_p$ and $\Omega_p t = 152$.

By studying the x-component, we can investigate how the actual coupling takes place. Leading up to the density enhancement seen in Figure 2b at $x\approx 218d_p$, we see a sharp increase in the pressure gradient. The enhanced O^+ density binds the electrons, and this configuration is kept stable by the x-component of the electric field. The pressure gradient of the electrons is directed toward the density peak and attempts to diffuse this enhancement but are instead kept together by electric forces such that $\partial_x P_{xx}^e \approx -en_eE_x$ is fulfilled.

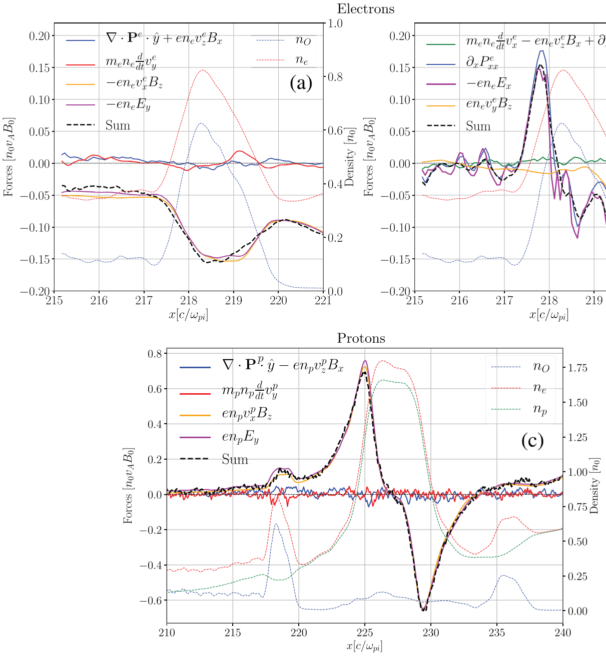

Figure 2. Cut through the X-point, along the x-direction, showing (a) the y-component and (b) the x-component of the momentum equation for electrons. Panel (c) shows the y-component of the momentum equation for the protons over a larger region in the x-direction, which reveals the frozen-in behavior of the protons. At $x \approx 218 d_p$, we see the clear n_O and n_e enhancements where the electrostatic coupling is most profound. From the low-density gradient of the protons in this region, we see that they do not, strongly, take part in the electrostatic coupling. The momentum equation for both the protons and electrons is calculated between $\Omega_p t = 152 - 152.5$. The black dotted line is the sum of the terms adding up to $-en_e E_y$.

This electrostatic coupling now forces the e^- to move with the O$^+$. In turn, this induced electron motion leads to the flux transport consistent with the X-point motion. Shown in Figure 2c, the protons also display frozen-in behavior as $E_y + v_x^p B_z \approx 0$. Hence, they are moving with the magnetic flux as well, at the cost of a small fraction of the oxygen ion's momentum.

3.2. Evaluation of Coupling With a Lower O$^+$ Density Run

In order to test if such a coupling still occurs with a substantially lower O$^+$ density, we perform a simulation with the same conditions as described in section 2, except with an oxygen number density of a tenth of the first shown run, that is, $n_{O^+} = 0.02$. In this case, we also observe an x-directed motion of the X-point moving at approximately the center-of-mass velocity, which now is $v_c = 0.25$. The electrostatic coupling between O$^+$ and e^- is less profound but remains adequate to result in a clear motion of the X-point. In Figures 3a and 3b we see the clear motion of the X-point together with the matching motion of the oxygen ions and the magnetic flux seen to the right of the X-point. When the oxygen content in the reconnection region is of significance, and the X-point starts moving at approximately v_c, we evaluate the electron momentum equation over the rightmost n_{O^+} enhancement at $\Omega_p t = 184$, indicated by the white line in Figure 3b. In Figure 3c, we see the frozen-in behavior of the electrons over the density enhancements as $E_y \approx v_x^e B_z$. Furthermore, Figure 3d reveals the same manifestation as the high oxygen density, seen in Figure 2b, run with the pressure gradient $\partial_x P_{xx}^e$ balanced by the electric force $-en_e E_x$, thus permitting a coupling between O$^+$ and e^-. From this, we conclude that such a coupling may still occur even with a substantial reduction of the oxygen abundance.

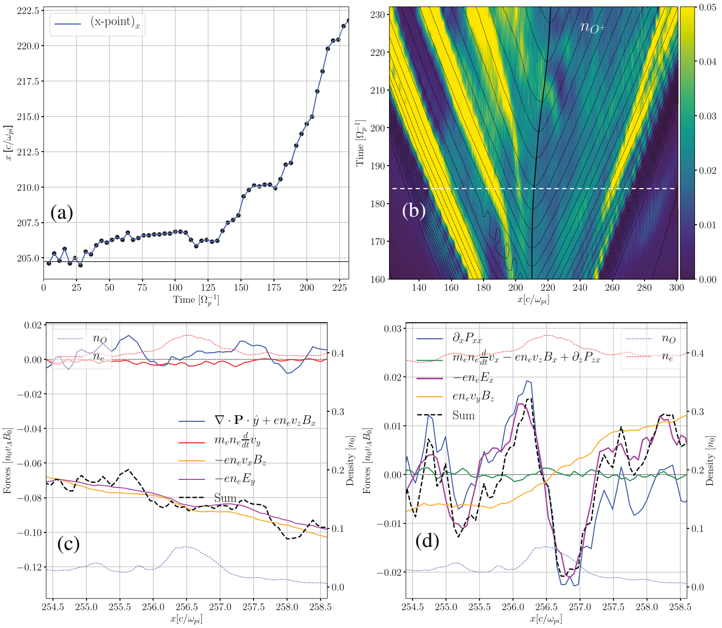

Figure 3. Panels (a) and (b) display the X-point motion as well as the n_{O^+} evolution (same as seen in Figure 1) for the low-density run. The white dotted line in (b) shows the region of calculation of the y-component and x-component of the electron momentum equation in (c) and (d), respectively. The electron momentum equation is calculated at $\Omega_p t = 184$.

3.3. Density Striations

In this section we investigate the intricate density striations, seen in Figures 4a–4c, which, as we will see, can be attributed to the additional x-directed momentum of O$^+$. In Figure 4a, we see the formation of an oxygen wave, due to the collective acceleration of O$^+$ by the Hall electric field E_z, thus leaving behind a density cavity (Tenfjord et al., 2018). This is the same manifestation as for the nonstreaming case, but as the system evolves, new types of striations arise as a result of the oxygen's more complicated interactions with E_z prior to reaching the reconnection site. This interaction results in more complex distribution functions specific to the streaming case, and an example is shown in Figures 4d–4f. The VDF is extracted at the oxygen wave front shown in Figures 4a–4c at time $\Omega_p t = 140$. It reveals, as shown in Figures 4d–4f, three dominant populations with clear separation in v_z. In order to understand the origin of the density striations, we follow two oxygen test particles from Populations (1) and (2), shown in Figure 4. Their initial conditions are selected as the most probable phase-space coordinate for the respective population. As the system is symmetric in z, Population (3) exhibits the same features as Population (1), only with the opposite z-direction of the velocity.

Figures 4g and 4h show the trajectories of the test particles from Populations (1) and (2) which have been traced $\pm 20\Omega_p^{-1}$ in dynamically changing fields with a time step of $0.5\Omega_p^{-1}$ from $\Omega_p t = 140$ by the initial conditions obtained from the VDF shown in Figures 4d–4f. Dependent on the regions at which O$^+$ originates from, they interact differently with the Hall electric field E_z. This can be seen in Figures 4i and 4j, which show the forces acting on the test particles from the respective populations.

The test particle from Population (1), seen in Figures 4g and 4h as the white trajectory, originates from further out in the lobe and experiences a much stronger acceleration as it encounters a different E_z region. Seen in Figure 4i, its substantially higher v_z enables it to overcome the electric potential and continue its motion out to the lobes before it is reflected by the Lorentz force due to $-v_z B_x$ and subsequently $v_y B_x$. Particles that exhibit similar properties trace out the outermost striations evident in Figure 4c. The test particle from

AGU ADVANCING EARTH AND SPACE SCIENCE

Geophysical Research Letters

10.1029/2020GL089462

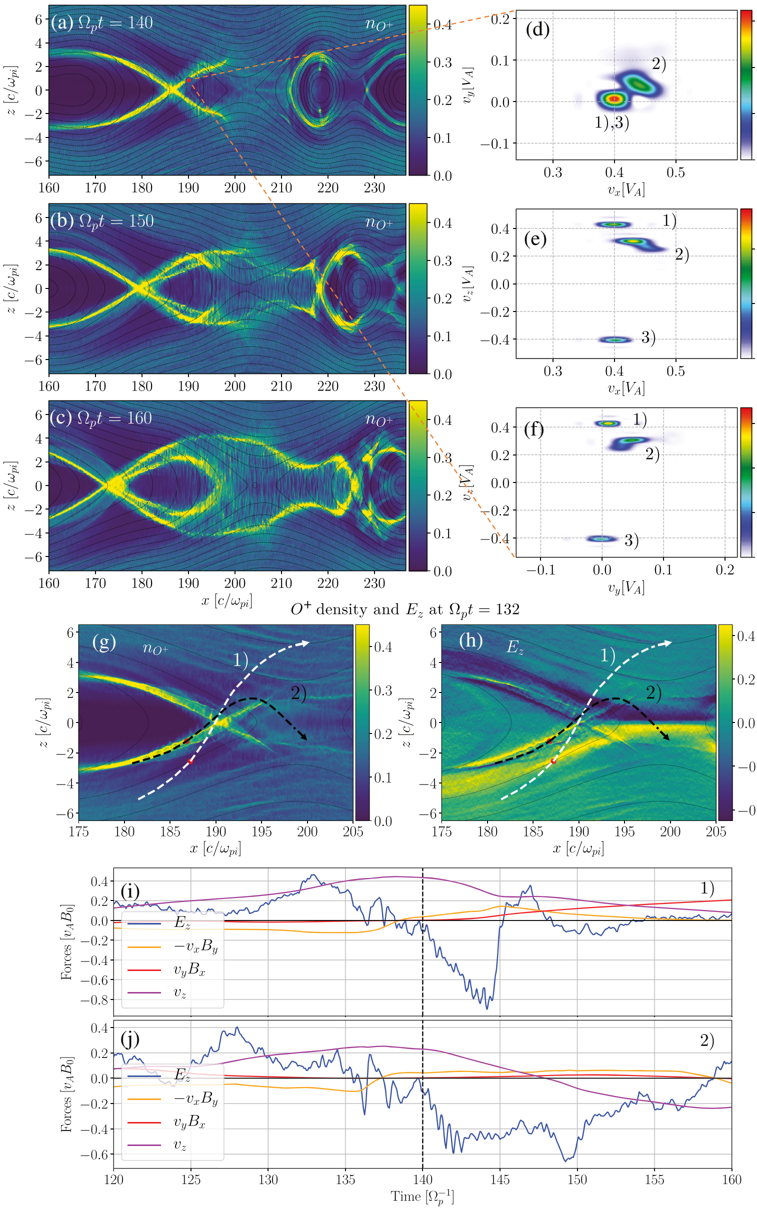

Figure 4. (a–c) Time of evolution of the oxygen density for the high n_{O^+} run. (d–f) VDF extracted at $(\Omega_p t, x, z) = (140, 190.5d_p, 0.5d_p)$. (g, h) Particle tracing of Populations (1) (white) and (2) (black) where the color map shows the (a) O$^+$ density and (b) E_z at $\Omega_p t = 132$. The red dots shows the location of the O$^+$ test particles at $\Omega_p t = 132$. Panels (i) and (j) show the forces in the z-direction acting on particles from Populations (1) and (2), respectively. The vertical dotted line in black shows the initial time of tracing.

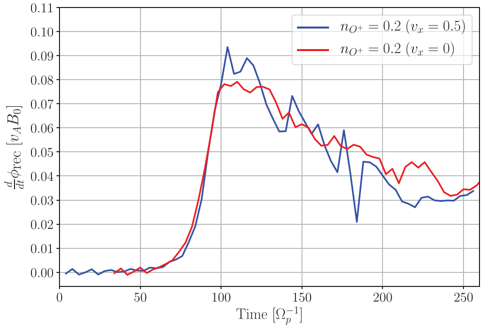

Figure 5. Time of evolution of the reconnection rate expressed as the temporal change of the magnetic flux $\frac{d}{dt}\phi_{\mathrm{rec}}$. In blue: streaming run. Red: nonstreaming run.

Population (2), seen in Figures 4g and 4h as the black trajectory, travels along the clear density enhancement upon interacting with E_z. The E_z this particle encounters is not strong enough for it to be accelerated to a sufficiently high v_z to overcome the electric potential on the opposite side of the current sheet; see Figure 4j. It is thus reflected in the z-direction by E_z and proceeds with a bounce motion across the current sheet until it reaches the exhaust. Such particles trace out the innermost striation seen in Figure 4c.

Particles originating from Populations (1) and (3) both trace out the outer striations as they share similar acceleration histories, only from the southern and northern lobes, respectively. These particles are collectively accelerated by the Hall electric field, which forms an oxygen wave leaving behind a density cavity (Tenfjord et al., 2018). As the Hall electric field expands, oxygen ions further into the lobes are accelerated toward the diffusion region causing an expansion in the z-direction of the outermost striations. Figures 4a–4c and 1b create the impression of an outflow of oxygen ions toward the Earth—counter to the original tailward motion of the O$^+$. This apparent motion in the negative x-direction is solely the result of an earthward shift of the intersection between the outer striations as they expand. There are therefore not indications of any transport of O$^+$ in the negative x-direction.

The striations discussed in this section may be observed by spacecraft, but it is, in principle, possible that they are unstable to various waves. In the simulation, the velocity of the O$^+$ is small compared to the thermal velocity of the protons and the electrons, and thus, it is less likely that the oxygen ions will drive any instabilities. However, other instabilities could, of course, cause fluctuations in the Hall electric field that accelerates O$^+$ and therefore impact the integrity of the structures.

4. Reconnection Rate

The evolution of the reconnection rate is displayed in Figure 5. We compare the reconnection rate to a similar run with the same oxygen number density n_{O^+} but with no initial x-directed bulk velocity, hereafter referred to as the nonstreaming run. Compared to the nonstreaming run, the reconnection process reaches its fast phase at a later time due to a smaller initial perturbation. For illustrations purposes, we shift the nonstreaming run by $\Omega_p t = 30$ to have the fast phases aligned.

We do notice a slightly higher peak for the streaming run. This is a transient effect as a result of the low abundance of oxygen ions at the reconnection site. The difference between the distance of the initial location of the front of the oxygen ions to the current sheet is slightly larger for the streaming run. This allows, to a greater extent compared to the nonstreaming run, an unencumbered motion of the upstream magnetic flux tubes, which results in a faster reconnection rate. The reconnection process therefore proceeds faster until the density of the oxygen ions in the reconnection site becomes significant. From this we conclude that a streaming population does not impose any further reduction of the reconnection rate.

5. Discussion and Summary

Motivated by ionospheric outflow, the results provided in this paper provide insights into how a streaming demagnetized species alter the dynamics of the reconnection process. We have shown that the X-point moves with the center-of-mass velocity v_c, which is predominantly provided by the oxygen ions.

Tenfjord et al. (2020) performed a similar study with the protons as the streaming population and found that the X-point also moves with v_c. The protons remain magnetized in the exhaust, and thus, their coupling to the magnetic field is evident. Having oxygen ions as the streaming population, however, is considerably different as they do not exhibit a magnetized behavior throughout the times of investigation. Our findings show that a demagnetized species alters the dynamics of the reconnection site long before the time of magnetization is realized. The coupling of O$^+$ to the magnetic flux occurs instead indirectly through the electrons by an electrostatic coupling. This shows that, regardless of whether the streaming population is magnetized or not, the system will reorganize itself in such a manner as to retain a net zero outflow momenta in the frame of reference of the X-point.

Compared to a nonstreaming run (e.g., Tenfjord et al., 2018), a streaming population gives rise to involved distribution functions due to the interaction with the Hall electric field E_z. The O^+ populations shown in Figures 4d–4f trace out the distinct striations seen in Figure 4c. Regarding observations, the VDF shown here should be detectable by spacecraft, but may be modified by kinetic effects not included in our simulation. Furthermore, our results show that a streaming population does not impose any change to the reconnection rate.

The results obtained in this study may apply to magnetotail reconnection in case of ionospheric outflow which results in high momentum O^+. With regard to space applications, we hope that the results laid out in this paper provide useful insight for future analysis of space mission data, in particular, the Magnetospheric Multiscale mission.

Data Availability Statement

Data set used in this analysis is available at Kolstø (2020).

Acknowledgments
This study was supported by the University of Bergen, by NOTUR/NORSTOR under project NN9496K, and by NASA's MMS mission. P. Tenfjord and C. Norgren was supported by the Research Council of Norway under contract 300865.

References

Baker, D. N., Hones, E. W., Young, D. T., & Birn, J. (1982). The possible role of ionospheric oxygen in the initiation and development of plasma sheet instabilities. *Geophysical Research Letters*, *9*(12), 1337–1340. https://doi.org/10.1029/GL009i012p01337

Chappell, C. R., Moore, T. E., & Waite, J. H. (1987). The ionosphere as a fully adequate source of plasma for the Earth's magnetosphere. *Journal of Geophysical Research*, *92*(A6), 5896–5910. https://doi.org/10.1029/JA092iA06p05896

Dargent, J., Aunai, N., Lavraud, B., Toledo-Redondo, S., & Califano, F. (2020). Simulation of plasmaspheric plume impact on dayside magnetic reconnection. *Geophysical Research Letters*, *47*, e2019GL086546. https://doi.org/10.1029/2019GL086546

Divin, A., Khotyaintsev, Y. V., Vaivads, A., André, M., Toledo-Redondo, S., Markidis, S., & Lapenta, G. (2016). Three-scale structure of diffusion region in the presence of cold ions. *Journal of Geophysical Research: Space Physics*, *121*, 12,001–12,013. https://doi.org/10.1002/2016JA023606

Frank, L. A., Ackerson, K. L., & Yeager, D. M. (2012). Observations of atomic oxygen (O+) in the Earth's magnetotail. *Journal of Geophysical Research*, *82*(1), 129–134. https://doi.org/10.1029/JA082i001p00129

Grande, M., Perry, C. H., Hall, A., Fennell, J., Nakamura, R., & Kamide, Y. (2013). What is the effect of substorms on the ring current ion population during a geomagnetic storm? *American Geophysical Union (AGU)*, *142*, 75–89. https://doi.org/10.1029/142GM08

Kistler, L. M., Mouikis, C., Möbius, E., Klecker, B., Sauvaud, J. A., Réme, H., et al. (2005). Contribution of nonadiabatic ions to the cross-tail current in an O+ dominated thin current sheet. *Journal of Geophysical Research*, *110*, A06213. https://doi.org/10.1029/2004JA010653

Kolstø, H. M. (2020). Replication data for: On the impact of a streaming oxygen population on collisionless magnetic reconnection. DataverseNO, https://doi.org/10.18710/AG7QVS

Kolstø, H. M, Hesse, M., Norgren, C., Tenfjord, P., Spinnangr, S. F., & Kwagala, N. (2020). Collisionless magnetic reconnection in an asymmetric oxygen density configuration. *Geophysical Research Letters*, *47*, e2019GL085359. https://doi.org/10.1029/2019GL085359

Moore, T. E., Chandler, M. O., Fok, M.-C., Giles, B. L., Delcourt, D. C., Horwitz, J. L., & Pollock, C. J. (2001). Ring currents and internal plasma sources. *Space Science Reviews*, *95*(1-2), 555–568. https://doi.org/10.1023/A:1005264907107

Mouikis, C. G., Kistler, L. M., Liu, Y. H., Klecker, B., Korth, A., & Dandouras, I. (2018). H+ and O+ content of the plasma sheet at 15-19 Re as a function of geomagnetic and solar activity. *Journal of Geophysical Research: Space Physics*, *115*, A00J16. https://doi.org/10.1029/2010JA015978

Shay, M. A., & Swisdak, M. (2004). Three-species collisionless reconnection: Effect of O^+ on magnetotail reconnection. *Physical Review Letters*, *93*(17), 175001. https://doi.org/10.1103/PhysRevLett.93.175001

Tenfjord, P., Hesse, M., & Norgren, C. (2018). The formation of an oxygen wave by magnetic reconnection. *Journal of Geophysical Research: Space Physics*, *123*, 9370–9380. https://doi.org/10.1029/2018JA026026

Tenfjord, P., Hesse, M., Norgren, C., Spinnangr, S. F., & Kolstø, H. (2019). The impact of oxygen on the reconnection rate. *Geophysical Research Letters*, *46*, 6195–6203. https://doi.org/10.1029/2019GL082175

Tenfjord, P., Hesse, M., Norgren, C., Spinnangr, S. F., Kolstø, H., & Kwagala, N. (2020). Interaction of cold streaming protons with the reconnection process. *Journal of Geophysical Research: Space Physics*, *125*, e2019JA027619. https://doi.org/10.1029/2019JA027619

Toledo-Redondo, S., Vaivads, A., André, M., & Khotyaintsev, Y. V. (2015). Modification of the Hall physics in magnetic reconnection due to cold ions at the Earth's magnetopause. *Geophysical Research Letters*, *42*, 6146–6154. https://doi.org/10.1002/2015GL065129

Vasyliunas, V. M. (1975). Theoretical models of magnetic field line merging. *Reviews of Geophysics*, *13*(1), 303–336. https://doi.org/10.1029/RG013i001p00303

Wilken, B., Zong, Q. G., Daglis, I. A., Doke, T., Livi, S., Maezawa, K., et al. (1995). Tailward flowing energetic oxygen ion bursts associated with multiple flux ropes in the distant magnetotail: GEOTAil observations. *Geophysical Research Letters*, *22*(23), 3267–3270. https://doi.org/10.1029/95GL02980

Wygant, J. R., Cattell, C. A., Lysak, R., Song, Y., Dombeck, J., McFadden, J., et al. (2005). Cluster observations of an intense normal component of the electric field at a thin reconnecting current sheet in the tail and its role in the shock-like acceleration of the ion fluid into the separatrix region. *Journal of Geophysical Research*, *110*, A09206. https://doi.org/10.1029/2004JA010708

Zong, Q.-G., Wilken, B., Woch, J., Mukai, T., Yamamoto, T., Reeves, G. D., et al. (1998). Energetic oxygen ion bursts in the distant magnetotail as a product of intense substorms: Three case studies. *Journal of Geophysical Research*, *103*(A9), 20,339–20,363. https://doi.org/10.1029/97JA01146

Paper III

Magnetospheric Multiscale Observations of an Expanding Oxygen Wave in Magnetic Reconnection

H.M. Kolstø, C. Norgren, M. Hesse, L.J. Chen P. Tenfjord, S.F. Spinnangr, N. Kwagala

Geophysical Research Letters, Vol. 48, Issue 19 doi:10.1029/2021GL095065, 2021

ADVANCING EARTH AND SPACE SCIENCE

Geophysical Research Letters®

RESEARCH LETTER
10.1029/2021GL095065

Magnetospheric Multiscale Observations of an Expanding Oxygen Wave in Magnetic Reconnection

Håkon Midthun Kolstø[1], **Cecilia Norgren**[1], **Michael Hesse**[2], **Li-Jen Chen**[3], **Paul Tenfjord**[1], **Susanne Flø Spinnangr**[1], **and Norah Kwagala**[1]

[1]Space Plasma Physics Group, University of Bergen, Bergen, Norway, [2]NASA Ames Research Center, Mountain View, CA, USA, [3]NASA Goddard Space Flight Center, Greenbelt, MD, USA

Key Points:

- Observation of Hall electric field accelerated O^+ inside separatrix density cavity
- Observational evidence of predicted oxygen wave
- Observed oxygen dynamics and corresponding velocity distribution functions consistent with simulation predictions

Correspondence to:

H. M. Kolstø,
hakon.kolsto@uib.no

Citation:

Kolstø, H. M., Norgren, C., Hesse, M., Chen, L.-J., Tenfjord, P., Spinnangr, S. F., & Kwagala, N. (2021). Magnetospheric multiscale observations of an expanding oxygen wave in magnetic reconnection. *Geophysical Research Letters*, *48*, e2021GL095065. https://doi.org/10.1029/2021GL095065

Received 30 JUN 2021
Accepted 9 SEP 2021

Abstract

Heavier plasma species such as oxygen ions can have a large impact on the magnetic reconnection process. It has been hypothesized that the acceleration of demagnetized oxygen ions by the Hall electric field will lead to the formation of an oxygen wave that expands into the exhaust. By comparing data from NASA's Magnetospheric Multiscale mission to a fully kinetic particle-in-cell simulation, we can for the first time provide observational evidence of such an expanding oxygen wave. The wave is characterized by an oxygen jet consisting of cold ions directed toward the neutral sheet associated with a density cavity. This density cavity forms as the O^+ are subject to collective acceleration by the Hall electric field leaving behind a region of low-density oxygen ions. Our results are important for the understanding of the role and effect of oxygen ions in magnetic reconnection.

Plain Language Summary

Magnetic reconnection is one of the most important energy release and transport processes in plasmas. In the case of the Earth's magnetosphere, magnetic reconnection is the primary mechanism responsible for the transport of energy, mass, momentum, and magnetic flux into Earth's magnetic cavity. On the night side of Earth in a region called the magnetotail, magnetic flux is transported from the north and south to meet in a current layer that extends across the width of the magnetosphere. While the most common plasma species in the magnetotail are protons and electrons, during high geomagnetic activity heavier ion species, such as oxygen, can sometimes dominate during high geomagnetic activity. Using data collected by NASA's Magnetospheric Multiscale mission together with numerical simulation, we investigate how oxygen ions contribute to the reconnection process.

1. Introduction

Magnetic reconnection is one of the most important energy conversion and transport processes in space plasma. It converts stored magnetic energy to thermal and kinetic energy of the plasma species. In addition to protons and electrons, multispecies plasma is commonly observed by various spacecraft in our magnetosphere (Baker et al., 1982; Chappell et al., 1987; Moore et al., 2001). Oxygen ions present in the plasma sheet, originating from the high-latitude ionosphere have been widely reported (Frank et al., 2012; Grande et al., 2013; Moore et al., 2001; Mouikis et al., 2018; Toledo-Redondo et al., 2021; Wilken et al., 1995; Zong et al., 1998). The ionospheric outflow rate of these oxygen ions has been found to scale with geomagnetic activity (Baker et al., 1982) and the rate is significantly enhanced during storm time conditions. Spacecraft observations by Cluster reveal that O^+ may, at storm time, be the dominating ion species (Kistler et al., 2005; Wygant et al., 2005).

As the reconnection process converts electromagnetic energy to both thermal and kinetic energy of the plasma, the presence of O^+ in the reconnection region may strongly affect the energy partitioning. Compared to protons, the higher mass of the oxygen ions results in larger gyro radii at similar energies giving rise to multiscale diffusion regions where the O^+ becomes demagnetized (Liu et al., 2015). As reconnection proceeds, the demagnetization of O^+ introduces distinct spatial and temporal scales for the reconnection process (Liu et al., 2014, 2015; Shay & Swisdak, 2004). Tenfjord et al. (2019) showed that although oxygen ions are to a higher degree demagnetized, they can act as an energy sink, resulting in a reduction of the reconnection rate.

Cluster observations reported the existence of oxygen ions being ballistically accelerated by the Hall electric field, giving rise to counter streaming velocity distribution signatures (Wygant et al., 2005). Similar characteristics were also found in particle-in-cell simulations (Liang et al., 2017). Tenfjord et al. (2018) found that as the Hall electric field grows and expands further out in the lobes and downstream, oxygen ions are collectively accelerated giving rise to expanding oxygen jets. The front of these jets consists of propagating localized regions of high O^+ density which are referred to as oxygen waves (Tenfjord et al., 2018). This study provides the first observational evidence of such an expanding oxygen wave captured by NASA's Magnetospheric Multiscale (MMS) mission.

The paper is structured as follows: in Section 2, we introduce an overview of the MMS observations. In Section 3, we describe the simulation setup that is used to contextualize the observations. Section 4 examines the O^+ reconnection dynamics in the exhaust by comparing moments and velocity distribution functions (VDF) from both MMS and particle-in-cell simulations (PIC). This section further reports on the observational evidence of an expanding oxygen wave.

2. MMS Event Overview

The observational data used in this analysis has been collected by MMS. We present data from the Hot Plasma Composition Analyzer (HPCA) (Young et al., 2016), the Fluxgate Magnetometers (FGM) (Russell et al., 2016), the Fast Plasma Investigation (FPI) (Pollock et al., 2016), and the Electric field Double Probes (EDP) (Ergun et al., 2016; Lindqvist et al., 2016).

Figures 1a–1f show an overview of the event as observed by MMS1 on the fourth of August 2017 at [−21.5, 8.3, 2.6] Earth radii (R_e) in Geocentric Solar Magnetospheric (GSM) coordinates around 09:56–10:05 Universal Time (UT). As MMS1–4 all observe similar features, we only show data from one spacecraft. The minimum variance direction, N, represents the current sheet normal direction and is found through a Minimum Variance Analysis on the magnetic field (MVA-B) (Sonnerup & Cahill, 1967) between 09:41:30 and 10:02:30 UT. As seen in Figure 1a, $B_N = 0$ nT at the beginning of the time interval, but gradually increases to $B_N \sim 10$ nT at the end. This increase in B_N is not directly related to the exhaust signatures (i.e., B_N is finite even when MMS has exited the main jet) and, therefore, we believe this can be attributed to current sheet rotation or tilting at the time of the investigation. To complete our coordinate system, we choose $\vec{L}$ such that B_L is the dominant component of **B** at the beginning of the time interval. We note, however, the possibility of a finite guide field. The choice of $\vec{L}$ also roughly maximizes the outflow speeds v_L^e and ion v_L^i, which we expect in the reconnection outflow. Our final LMN-coordinate system is then given by $\vec{L} = (0.92, -0.31, -0.25)$, $\vec{M} = (0.09, 0.79, -0.61)$, and $\vec{N} = (0.39, 0.54, 0.75)$ (GSM), where L is the implied reconnection outflow direction, and M is the current direction.

Throughout the interval, $B_L > 0$. Since $\hat{L} \sim \hat{x}_{GSM}$, we conclude that the spacecraft remained north of the neutral sheet during the observed time interval. As the spacecraft moves toward the neutral sheet, MMS observes increasing B_M, which coincides with the strong E_N (Figure 1b). We identify E_N and B_M as the Hall electric and magnetic fields, respectively. Furthermore, we note the increasing value of E_M which, at later times, becomes proportional to E_N. This suggests that the N and M vectors are locally a nonperfect coordinate system, i.e., the current sheet normal direction is actually a mix of N and M.

Between 10:01 and 10:03 UT, strong Earthward ($v_L > 0$) ion and electron jets, reaching speeds up to 1,000 km/s, are observed by FPI (Figures 1c and 1d). The strong Hall fields and jets indicate that the spacecraft has entered the reconnection exhaust. The oxygen velocity $v_L^{O^+}$ (Figure 1e) is clearly decoupled from these high velocities, instead showing a consistent Earthward-flowing component of ~150–200 km/s. Whereas the FPI ion and electrons predominantly show Earthward-flowing bulk velocities, the oxygen ions experience strong flows toward the neutral sheet seen in Figure 1e at ~10:02 UT reaching values of $v_N^{O^+} \approx -500$ km/s. This region of enhanced negative $v_N^{O^+}$ coincides with a region of low O^+ density ($n_{O+} = 0.006$ cm^{-3}) (Figure 1f). This density cavity is bordered by two regions of slightly enhanced n_{O+} (labeled A and C) with values of 0.025 cm^{-3}. Inside the cavity, the drifting ion population approaches the energy cutoff of the HPCA instrument. When the high-speed flow is observed, the drifting component is resolved. However, during the first part of the cavity at ~10:01:30–10:02:00 UT, it is possible that the beam has exceeded the HPCA energy limit. The O^+ density should therefore be considered as a lower limit.

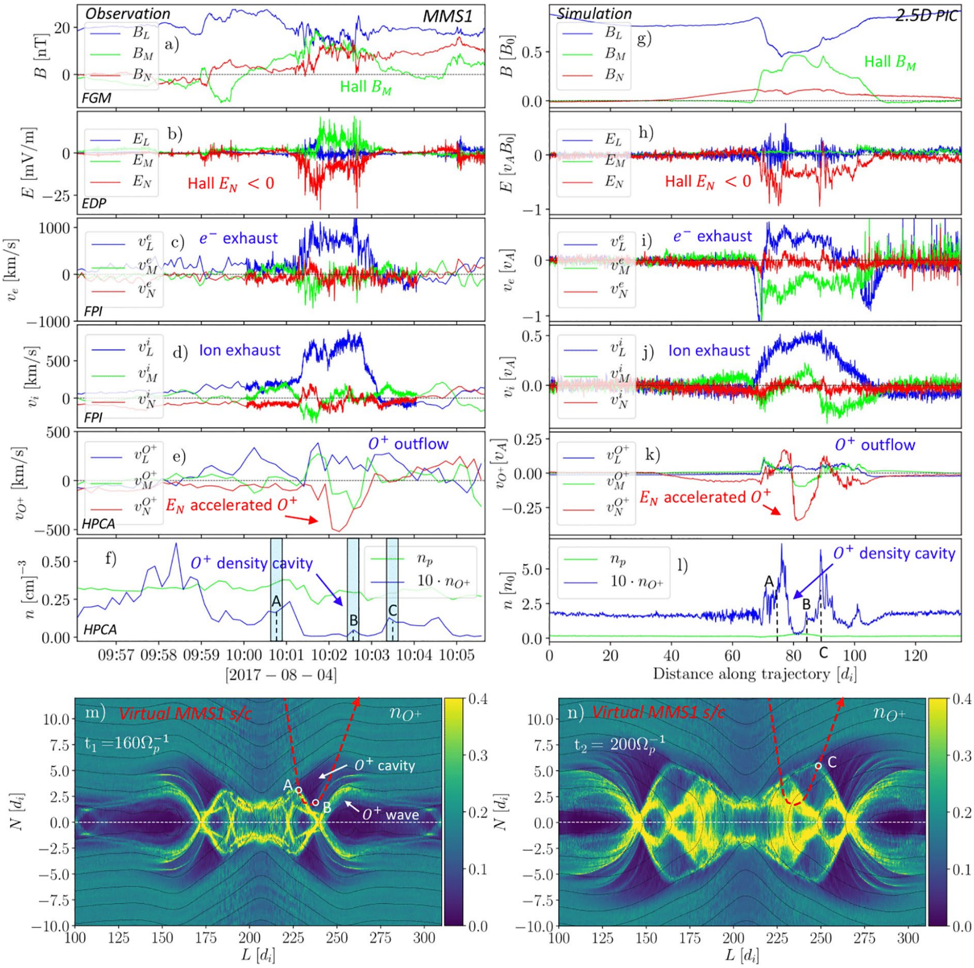

Figure 1. (a–f) Observational data collected by the MMS1 spacecraft. (a) Magnetic field, (b) electric field, (c) FPI electron, and (d) ion bulk velocities. (e) HPCA O^+ bulk velocity. (f) HPCA O^+ and H^+ density. Burst data are collected between 10:00:04 and 10:04:56. (g–l) Simulation data collected by a virtual spacecraft whose trajectory is overlaid on the O^+ density depicted in the color map (m, n) at times t_1 and t_2 (g) Magnetic field and (h) electric field. (i) Electron and (j) proton bulk velocities. (k) O^+ bulk velocity. (l) O^+ and H^+ density. Points marked A, B, and C, in panels (f, l, m, and n) correspond to the location where the VDFs have been extracted. The shaded area in (f) corresponds to the collection time (~10 s) to calculate the VDFs. The relative motion traced in (m, n) is attributed to the N-directed flapping of the current sheet together with the tailward motion of the reconnection site.

There is also a clear enhancement of $n_{O+} \approx 0.055\text{cm}^{-3}$ around 09:58 UT, prior to the encounter of the exhaust jet. The origin of this enhancement is unknown but may be due to variations in the inflow regions. However, in this paper, we seek to understand the origin of the O^+ density structures and dynamics observed in the reconnection exhaust. In order to gain deeper insight into the structures observed by MMS, we utilize a 2.5D PIC simulation.

3. Simulation Setup

The magnetic field configuration is given by a generalized Harris-type equilibrium defined as $B_x = B_0 \tanh(z/\lambda)$, where $\lambda = 2d_p$ is the half width of the initial current sheet, and $d_p = c/\omega_{pi} (= c\sqrt{\epsilon_0 m_p / n_0 e^2})$ is the proton inertial length (see Hesse et al., 1999 for details). Densities are normalized to the foreground density at the center of the initial current sheet n_0, lengths to d_p, and time to the inverse of the proton cyclotron frequency $\Omega_p^{-1} = m_p / eB_0$. A uniform proton density distribution of $n_b = 0.2$ is added to the initial Harris-sheet density configuration $n_p = n_0 / \cosh^2(z/\lambda)$ resulting in a peak density of 1.2 in the current layer. Oxygen ions are homogeneously distributed above a specific field line, corresponding to a distance of $|z| > 3d_p$ from the current sheet with $n_{O^+} = 0.2$. The O^+ has initially zero thermal velocity. The mass ratios are: $n_p / m_e = 25$ for the protons/electrons and $m_{O^+} / m_p = 16$ for the oxygen/protons. A total of $\sim 10^{10}$ macroparticles are used. Boundary conditions are periodic at $x = x_{min}$ and $x = x_{max}$. At $z = z_{min}$ and $z = z_{max}$, specular reflection is enabled and the out-of-plane electric field E_y is set to zero, preserving magnetic flux in the simulation domain. The size of our simulation domain is $410d_p \times 50d_p$ with a grid size of $6{,}400 \times 1{,}600$. We employ a time step of $\omega_{pe}\delta t = 0.5$. The velocity normalization is the proton Alfvén speed, based on the foreground current sheet density n_0. The foreground temperatures fulfill $T_p + T_e = 0.5$, in units of $[m_p v_A^2]$, derived from pressure balance $n_0(T_p + T_e) = B_0^2/2$. The ratio of the proton-electron temperature is $T_p / T_e = 5$. The ratio between the electron plasma frequency and gyrofrequency is $\omega_{pe}/\Omega_e = 2$. Based on the observed conditions from Figures 1a and 1f ($B = 24$ nT and $n = 0.35$ cm^{-3}), we infer the Alfvén velocity and ion inertial length to be $v_A \approx 920$ km/s and $d_i \approx 396$ km, respectively. The simulation used in this study was not designed to represent this exact event, but rather, a general reconnection process with high abundance O^+ made to capture the additional effects introduced by heavier plasma species.

4. O^+ Reconnection Dynamics; MMS and PIC Comparison

Based on the data collected by MMS, Figure 1, we utilize the PIC simulation to search for a simple virtual spacecraft trajectory that enables us to contextualize the observations. This further aids in understanding the O^+ dynamics and density structure seen in Figures 1e and 1f, respectively. In Figures 1g–1l, we see the observables extracted from a possible trajectory overlaid in the O^+ density map in Figures 1m and 1n.

The trajectory is constructed by first matching the $\mathbf{B}_{FGM}$ and $\mathbf{B}_{PIC}$ data, providing us with an indication of the location of MMS with respect to the neutral sheet. Note that this simple trajectory captures the additional signatures encountered by MMS such as E_N and the FPI ion and electron bulk velocities $\mathbf{v}^i_{LMN}$, $\mathbf{v}^e_{LMN}$. Upon entering the reconnection exhaust, the virtual spacecraft first encounters a region of enhanced n_{O^+} (labeled A) before dropping into a region of low n_{O^+}. This region of low n_{O^+} is identified as the O^+ density cavity (seen in Figures 1l and 1m). From Figure 1k, we also see the sudden increase of $-v_N^{O^+}$ in direct correspondence with the O^+ density cavity. We note that the density cavity observed by MMS is slightly broader than the jet structure, which is not the case for the simulation. This may be due to beam thermalization or trapping that reduces the bulk speed but conserves the density. Additionally, at the earlier edge of the cavity, where $|v_N|$ peaks, the beam approaches the highest energy levels of HPCA. We therefore also speculate that the beam may be broader than observed, but that this part of the beam is outside the energy range of HPCA.

We note that the oxygen density in the simulation exceeds that in the observations by a large margin. This is due to the initial conditions of the simulation, where the inflow oxygen density was relatively high. However, while the impact of the oxygen on the reconnection process would be affected by these relatively large differences in density, the demagnetized behavior of the oxygen in the outflow regions is qualitatively the same.

As seen in Figure 1f, MMS crossed the n_{O^+} density enhancement (labeled C) before exiting the reconnection region, thus marking the edge of the density cavity and the region of strong v_N-flows. In the simulation overview in Figures 1m, there are no signatures of a clear second density enhancement (as detected in the HPCA n_{O^+}, see label C in Figure 1f) along the trajectory after the cavity. The total time spent between the first (A) and the second (B) density enhancements in the observation is $\Delta t \sim 140\text{s} \approx 325\Omega_p^{-1}$ ($B = 24$ nT). During this time, the O^+ density structures may have experienced a significant expansion, thus we cannot

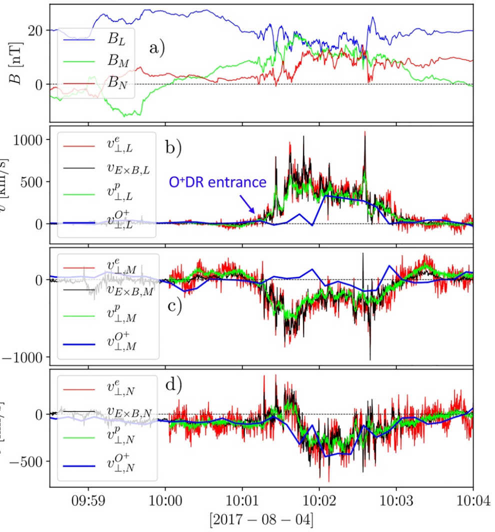

Figure 2. Comparison between $\mathbf{v}_{E\times B}$ and perpendicular velocities of ions (FPI), electrons (FPI), and oxygen (HPCA). (a) Magnetic field. (b–d) The components of the perpendicular velocities and $v_{E\times B}$. At ~10:01 UT, we see clear signs of demagnetization of oxygen ions marking the entrance of the O^+ diffusion region.

expect the simple quasi-stationary case. Therefore, we propose the following scenario; MMS enters the reconnection site and passes the density enhancement to enter the cavity. During the time Δt, the O^+ density structures expand, and as MMS exits the reconnection region it encounters the expanded structure at a different location in space and time. To probe this proposed scenario, a spatiotemporal trajectory is utilized to account for the time evolution of the density structures. Between points A and C, we let the simulation evolve in time allowing the O^+ front to expand such that the density structure again catches up to the spacecraft.

The remarkable similarities between the data observed by MMS and the data along our virtual trajectory strongly suggest that MMS passes through a region similar to that observed in the simulations. We thus hypothesize that the O^+ density cavity, seen in Figure 1f, is similar to the cavity in the simulation (Figures 1l) which forms due to the collective acceleration by E_N resulting in an oxygen wavefront propagating in the negative N-direction. In Sections 4.1 and 4.2, we examine whether the O^+ in the observations exhibit the demagnetized properties needed to give rise to such density signatures.

4.1. Dynamics of O^+ in the Reconnection Exhaust

The observed low-density region of O^+, referred to as the oxygen density *cavity* (see Figure 1f at 10:02 UT), originates from the demagnetized behavior of the oxygen ions. As reconnection proceeds, the Hall electric field expands due to the increasingly decoupled motion of the ions and electrons. If the oxygen ions are demagnetized, their initial motion while entering the reconnection exhaust will predominantly be due to E_N (Tenfjord et al., 2018). Due to the growth and expansion of E_N, the O^+ situated in the lobes will be picked up by the Hall electric field and accelerated toward the neutral line forming a propagating O^+ density front, i.e., the oxygen wave. In the simulation domain depicted in Figures 1m and 1n, we see an example of an oxygen wave by the slanted regions of high density that expand. As a large region of oxygen ions experience a strong acceleration by the expanding E_N, a wake of low O^+ density arises, resulting in a density cavity. These signatures are seen in Figures 1m and 1n as darker regions, indicating the absence of oxygen ions, followed by the intensified bands of high abundance O^+ density striations. These structures have previously been discussed by Tenfjord et al. (2018) and Kolstø et al. (2020b). The oxygen ions studied in this simulation reveal a demagnetized behavior as the oxygen cyclotron period is significantly longer than the characteristic time evolution of the reconnection process ($\sim\Omega_p^{-1}$). To investigate the degree of demagnetization of the observed O^+, we compare $\vec{v}_{E\times B} = \vec{E}\times\vec{B}/B^2$ to $\vec{v}_\perp$ of electrons and ions as measured by FPI (predominantly protons), and oxygen as measured by HPCA. This comparison is seen in Figures 2b–2d. In Figure 2a, we show **B** for context. In the lobe, all species follow $\vec{v}_{E\times B}$ closely. The encounter of the ion and electron jets at ~10:01 UT corresponds to MMS's entrance into the reconnection region. At this time, we begin to see the deviation of $\vec{v}_\perp^{O^+}$ from $\vec{v}_{E\times B}$, demonstrating a multiscale diffusion region nature, and the demagnetization of O^+. Inside this O^+ diffusion region, $v_{\perp,L}^{O^+}$ and $v_{\perp,M}^{O^+}$ deviate significantly (by approximately 500 km/s) from $v_{E\times B}$. Meanwhile, the deviation is slightly smaller for the normal component with approximately 250 km/s at ~10:01:30 UT. Overall we conclude that the deviation within the exhaust is significant for the demagnetization of the oxygen ions. Throughout the time of investigation, the protons as measured by FPI remained magnetized, indicating that MMS never entered the proton, much less the electron, diffusion regions.

In Section 4.2, we compare PIC and HPCA O^+ VDFs to gain an understanding of the behavior of the oxygen ions within the reconnection exhaust. Further, we investigate if the observed density enhancements, representing the edges of the cavity (Figure 1f), are consistent with the density enhancements encountered by the proposed simulation trajectory (Figure 1l).

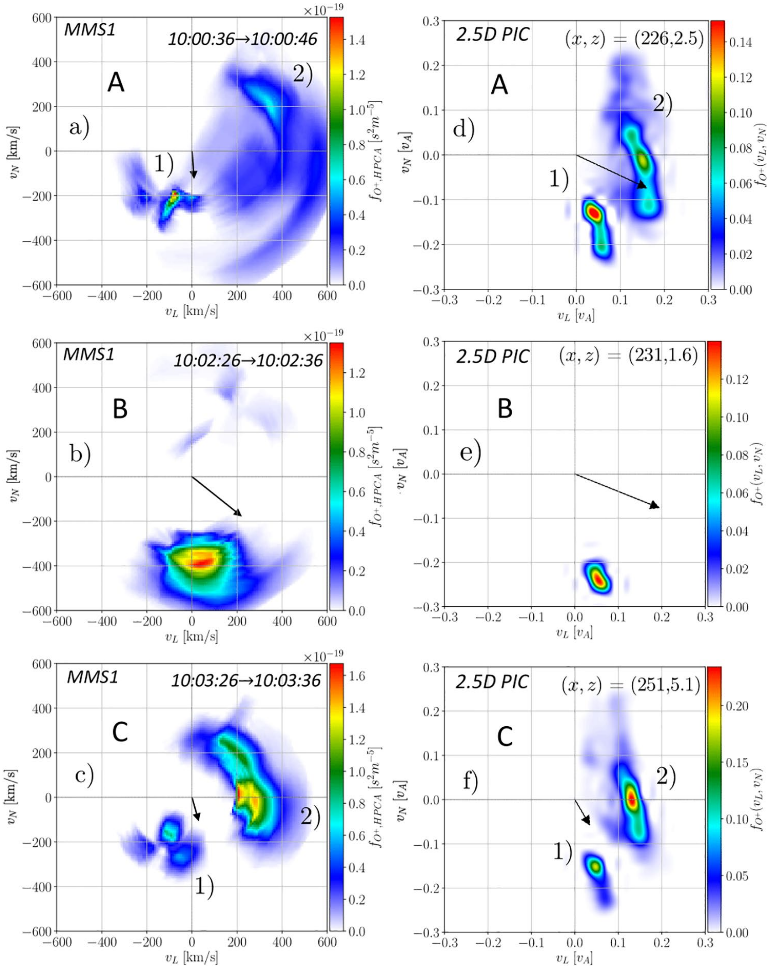

Figure 3. O^+ VDFs $f_{O^+}(v_L, v_N)$ at three locations marked A, B, and C in Figure 1. (a–c) HPCA. (d–f) PIC. The arrows represent $v_{E\times B}$ which, for the observations, are time-averaged over the collection time of the distribution. The normalization speed from observations ($v_A = 920$ km/s) shows good agreement in speeds between $f_{O^+}^{HPCA}(v_L, v_N)$ and $f_{O^+}^{PIC}(v_L, v_N)$, with the simulation being slightly lower.

4.2. O^+ Distribution Function Comparison

In Figure 1, the extracted fields, and velocity and density moments along the spacecraft trajectory correspond well to those observed by MMS. To investigate if the velocity space signatures in the vicinity of the density cavity also agree between simulations and observations, we extract the VDFs at locations A, B, and C (marked in Figure 1).

In Figure 3, we see the side-by-side comparison of the HPCA (Figures 3a–3c) and PIC (Figures 3d–3f) O^+ VDFs, defined as $f_{O^+}(v_L, v_N) = \int f_{O^+}(v_L, v_M, v_N) dv_M$. The $v_{E\times B}$-components are shown as the black arrow in all panels. At A, both $f_{O^+}^{HPCA}(v_L, v_N)$ and $f_{O^+}^{PIC}(v_L, v_N)$ are dominated by two distinct populations; (1) a colder population with $v_N < 0$, and (2), a warmer population spanning both positive and negative v_N. These two populations are well separated in v_L. The colder population is formed as O^+, originating from the northern inflow region, is accelerated by E_N, resulting in the ion passing straight through the upward expanding density enhancement and continuing its motion toward the neutral line. Population 2 exhibits a large spread in $v_N^{O^+}$ and primarily consist of particles originating from the south. The part of the population displaying $v_N < 0$ have been reflected by the Lorentz force $- v_N^{O^+} B_L$ and subsequently $v_M^{O^+} B_L$ to obtain a negative $v_N^{O^+}$. The positive $v_N^{O^+}$ part consists of particles that have not yet undergone a reflection. The obtained $v_L^{O^+}$ is produced by the Lorentz forces $- v_N^{O^+} B_M$ and $v_M^{O^+} B_N$. The Lorentz force $- v_N^{O^+} B_M$ is a result of the E_N-accelerated oxygen ions encountering the Hall magnetic field B_M whereas the $v_M^{O^+} B_N$ is due to the encounter of B_N after acceleration by the reconnection electric field E_M. Thus, part of $v_N^{O^+}$ and $v_M^{O^+}$ is diverted into $v_L^{O^+}$. The difference in $v_L^{O^+}$ between populations 1 and 2 is attributed to the time spent in the exhaust. The oxygen ions constituting population 1 enters from the northern lobe and thus the time spent in the exhaust is considerably less than that of the southern lobe originating particles in population 2 (recall that the VDFs are extracted on the northern side of the current sheet). Diversion from $v_M^{O^+}$ to $v_L^{O^+}$ for population 2 occurs over a greater time compared to population 1, resulting in a significantly stronger $v_L^{O^+}$. For population 2, we observe a slight increase of $v_L^{O^+}$ for decreasing $v_N^{O^+}$ velocities. After reflection, particles with large negative $v_N^{O^+}$ have experienced an acceleration by E_M due to the long time spent in the exhaust. During this time, an increase in v_L is realized by the Lorentz force $v_M^{O^+} B_N$. We further note that $v_L^{O^+}$ is dependent on where the oxygen ions enters within the exhaust.

In Figure 3b, we compare the VDFs at location B which is within the region of strong v_N-flows. Despite the low density for the observations, the count is considered sufficient to calculate a credible VDF at this location in the cavity. The beam at location B consists of O^+ that have a strong negative v_N centered around -400 km/s and it matches well the corresponding behavior seen in the simulation (Figure 3e). The O^+ from simulation obtains such a v_N through ballistic acceleration by E_N. Further, the simulation reveals that this population moves to form the oxygen wavefront. The demagnetized behavior of the O^+ seen in Figure 2, along with the strong agreement of the VDFs, leads us to conclude that the mechanism to produce the O^+ dynamics in the observations is similar to the simulation.

The VDF captured at the second encounter of the density edge (C) is seen in Figure 3c. The exceptional similarities of the signatures in the VDFs at the location of the density enhancements at location A and C indicates that these two enhancements are either of the same nature or created by similar mechanisms.

A difference between the VDFs provided by MMS and the ones seen in the PIC simulation is that of the $v_L^{O^+}$. In Figures 3a and 3c, we see that populations 1 and 2 exhibit different signs of $v_L^{O^+}$, while in the simulation, both populations display $v_L^{O^+} > 0$. Furthermore, at B, the Hall accelerated $v_N^{O^+}$ from PIC (Figure 3e) display a clear $v_L^{O^+}$ whereas the observational population (Figure 3b) appears to be centered closer to $v_L^{O^+} = 0$ km/s. This feature is attributed to the tailward streaming nature of the oxygen during the event and is not accounted for in the simulation—which considers the O^+ to be at rest. Regardless, the overall features and distribution of the particles match that of the simulation impressively well.

In Figure 4, we see $v_L^{O^+}$ together with **B**. Prior to the encounter of the reconnection region at ~10:00 UT, HPCA measures stable flows of tailward streaming O^+ reaching bulk velocities of $v_L^{O^+} \approx -180$ km/s. Previous studies have shown that the momentum of oxygen ions can induce a motion of the reconnection site regardless of its degree of magnetization (Kolstø et al., 2020b). In our case, due to the relatively low oxygen density, the effect on the center-of-mass velocity is low $v_{COM} \approx -19$ km/s. Hence, we expect the X-line motion induced by the oxygen flow to be low. However, the initial motion of the ions can be superposed with the motion gained during the reconnection process, which in our case would account for the differences in $v_L^{O^+}$ between simulations and observations. The average tailward flow of O^+ prior to the reconnection site (between 09:41 and 09:57) is found to be $v_{LOBE}^{O^+} \approx -110$km/s. A shift in the L-direction of $v_{LOBE}^{O^+}$ resolves the sign disparities of $v_L^{O^+}$ between HPCA and the simulation. Although the tailward flow of the oxygen ions decreases toward the reconnection site entrance (~10:00 UT), this can be due to local variations, and the added v_L velocities may be due to such variations that are present within the exhaust.

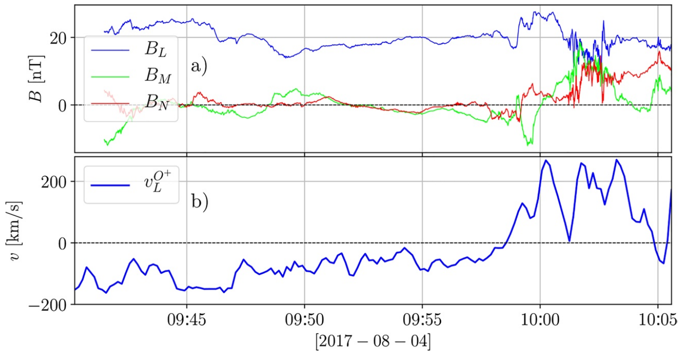

Figure 4. (a) Magnetic field, and (b) L-directed velocity of O^+ prior to the encounter of the reconnection region showing clear signs of tailward streaming oxygen ions.

4.3. Expanding Oxygen Wave

In this section, we discuss how the different populations seen in the VDFs in Figure 3 are expected signatures to be found in the vicinity of an oxygen wave. Inside the O^+ density cavity (location B), MMS observes cold lobe ions that are captured by the Hall electric field, and have started to move toward the current sheet (Figure 3b). Adjacent to the cavity (locations A and C), MMS still observe the cold lobe plasma accelerated toward the current center by E_N (population 1 in Figures 3a and 3c). In addition to the cold population, MMS observes a hot O^+ jet (population 2) that has likely undergone a significant acceleration by the reconnection electric field. This hotter population is the population that predominantly contributes to the bulk reconnection outflow. Locations A and C can therefore be considered as part of the reconnection outflow. In contrast, B is located where the outflow is still not present, i.e., downstream of the reconnection oxygen jet front. We, therefore, suggest that the transition from A or C to B is a signature of an expanding oxygen wave.

5. Discussion and Summary

In this paper, we have investigated the behavior of oxygen ions in the reconnection exhaust. The clear reconnection signatures captured by MMS, in the presence of O^+, enabled us to study the dynamics of the oxygen ions in great detail. To provide context to these observations, we utilized a 2.5D PIC simulation to construct a simple, time-evolutionary, trajectory to search for a probable path of MMS1 with respect to the reconnection region. The remarkable match of **E**, **B**, as well as the bulk and density moments between the simulation and observations provides a confident contextualization of the MMS data. Along the inferred MMS trajectory, we extracted O^+ VDFs at locations A, B, and C which further displayed a strong agreement between HPCA and PIC.

Based on the O^+ density structures encountered by MMS, and the signatures of the VDFs, we hypothesized that the spacecraft passed the same density ridge twice; (1) At the entrance of the exhaust (A), and (2) at the exit (C) after an expansion of the O^+ striation (occurring over a time of $\sim 325\Omega_p^{-1}$). The crossings through locations A and C marks the encounter of the oxygen wave, which is further supported by the observed density cavity at location B. Such density cavities are expected to be found as these regions represent the low-density wake after the collective E_N acceleration of O^+ giving rise to the oxygen wave (Tenfjord et al., 2018; Kolstø et al., 2020a). We acknowledge that there is a discrepancy between points A and C concerning the time covered by the spacecraft and the scaled simulation time and that this might be due to the structure evolving at different rates, exhibiting different spatial scales, or being structurally different. Further, the simulation is based on cold O^+ at rest in the inflow region, while in the current event the O^+ have a finite bulk velocity and temperature, which may conspire to alter the structure scale and evolution compared to the simulation.

The results reported in this study provide insight into the O^+ dynamics in the reconnection exhaust. Our comparison of MMS data with PIC modeling shows a remarkable agreement. This match suggests strongly that the features in the observations are, in fact, signatures of an oxygen wave.

Data Availability Statement

The simulation data set used is available at Kolstø (2021). MMS data are available online at MMS Science Data Center (2020).

Acknowledgments
This study was supported by the University of Bergen, by NOTUR/NORSTOR under Project NN9496 , and by NASA's MMS mission. Cecilia Norgren and Paul Tenfjord received support from the Research Council of Norway under Contract 30086. Further, we acknowledge the SPEDAS and pySPEDAS analysis tools.

References

Baker, D. N., Hones, E. W., Young, D. T., & Birn, J. (1982). The possible role of ionospheric oxygen in the initiation and development of plasma sheet instabilities. *Geophysical Research Letters*, *9*(12), 1337–1340. https://doi.org/10.1029/GL009i012p01337

Chappell, C. R., Moore, T. E., & Waite, J. H. (1987). The ionosphere as a fully adequate source of plasma for the Earth's magnetosphere. *Journal of Geophysical Research*, *92*(A6), 5896–5910. https://doi.org/10.1029/JA092iA06p05896

Ergun, R. E., Tucker, S., Westfall, J., Goodrich, K. A., Malaspina, D. M., Summers, D., et al. (2016). The axial double probe and fields signal processing for the MMS mission. *Space Science Reviews*, *199*(1), 167–188. https://doi.org/10.1007/s11214-014-0115-x

Frank, L. A., Ackerson, K. L., & Yeager, D. M. (2012). Observations of atomic oxygen (O+) in the Earth's magnetotail. *Journal of Geophysical Research*, *82*(1), 129–134. https://doi.org/10.1029/JA082i001p00129

Grande, M., Perry, C. H., Hall, A., Fennell, J., Nakamura, R., & Kamide, Y. (2013). *What is the effect of substorms on the ring current ion population during a geomagnetic storm?* (pp. 75–89). American Geophysical Union (AGU). https://doi.org/10.1029/142GM08

Hesse, M., Schindler, K., Birn, J., & Kuznetsova, M. (1999). The diffusion region in collisionless magnetic reconnection. *Physics of Plasmas*, *6*(5), 1781–1795. https://doi.org/10.1063/1.873436

Kistler, L. M., Mouikis, C., Möbius, E., Klecker, B., Sauvaud, J. A., Réme, H., & Balogh, A. (2005). Contribution of nonadiabatic ions to the cross-tail current in an O+ dominated thin current sheet. *Journal of Geophysical Research*, *110*, A06213. https://doi.org/10.1029/2004JA010653

Kolstø, H. M. (2021). *Replication data for: MMS observations of an expanding oxygen wave in magnetic reconnection*. DataverseNO. https://doi.org/10.18710/0PBOGL

Kolstø, H. M., Hesse, M., Norgren, C., Tenfjord, P., Spinnangr, S. F., & Kwagala, N. (2020a). Collisionless magnetic reconnection in an asymmetric oxygen density configuration. *Geophysical Research Letters*, *47*, e2019GL085359. https://doi.org/10.1029/2019GL085359

Kolstø, H. M., Hesse, M., Norgren, C., Tenfjord, P., Spinnangr, S. F., & Kwagala, N. (2020b). On the impact of a streaming oxygen population on collisionless magnetic reconnection. *Geophysical Research Letters*, *47*, e2020GL089462. https://doi.org/10.1029/2020GL089462

Liang, H., Lapenta, G., Walker, R. J., Schriver, D., El-Alaoui, M., & Berchem, J. (2017). Oxygen acceleration in magnetotail reconnection. *Journal of Geophysical Research: Space Physics*, *122*, 618–639. https://doi.org/10.1002/2016JA023060

Lindqvist, P.-A., Olsson, G., Torbert, R. B., King, B., Granoff, M., Rau, D., et al. (2016). The spin-plane double probe electric field instrument for MMS. *Space Science Reviews*, *199*(1), 137–165. https://doi.org/10.1007/s11214-014-0116-9

Liu, Y. H., Kistler, L. M., Mouikis, C. G., Roytershteyn, V., & Karimabadi, H. (2014). The scale of the magnetotail reconnecting current sheet in the presence of O+. *Geophysical Research Letters*, *41*, 4819–4827. https://doi.org/10.1002/2014GL060440

Liu, Y. H., Mouikis, C. G., Kistler, L. M., Wang, S., Roytershteyn, V., & Karimabadi, H. (2015). The heavy ion diffusion region in magnetic reconnection in the Earth's magnetotail. *Journal of Geophysical Research: Space Physics*, *120*, 3535–3551. https://doi.org/10.1002/2015JA020982

MMS Science Data Center. (2020). Retrieved from https://lasp.colorado.edu/mms/sdc/public/

Moore, T. E., Chandler, M. O., Fok, M.-C., Giles, B. L., Delcourt, D. C., Horwitz, J. L., & Pollock, C. J. (2001). Ring currents and internal plasma sources. *Space Science Reviews*, *95*(1–2), 555–568. https://doi.org/10.1023/A:1005264907107

Mouikis, C. G., Kistler, L. M., Liu, Y. H., Klecker, B., Korth, A., & Dandouras, I. (2018). H+ and O+ content of the plasma sheet at 15–19 Re as a function of geomagnetic and solar activity. *Journal of Geophysical Research: Space Physics*, *115*, A00J16. https://doi.org/10.1029/2010JA015978

Pollock, C., Moore, T., Jacques, A., Burch, J., Gliese, U., Saito, Y., et al. (2016). Fast plasma investigation for magnetospheric multiscale. *Space Science Reviews*, *199*(1), 331–406. https://doi.org/10.1007/s11214-016-0245-4

Russell, C. T., Anderson, B. J., Baumjohann, W., Bromund, K. R., Dearborn, D., Fischer, D., et al. (2016). The magnetospheric multiscale magnetometers. *Space Science Reviews*, *199*(1), 189–256. https://doi.org/10.1007/s11214-014-0057-3

Shay, M. A., & Swisdak, M. (2004). Three-species collisionless reconnection: Effect O^+ of on magnetotail reconnection. *Physical Review Letters*, *93*(17), 175001. https://doi.org/10.1103/PhysRevLett.93.175001

Sonnerup, B. U. Ö., & Cahill, L. J. (1967). Magnetopause structure and attitude from Explorer 12 observations. *Journal of Geophysical Research*, *72*(1), 171–183. https://doi.org/10.1029/JZ072i001p00171

Tenfjord, P., Hesse, M., & Norgren, C. (2018). The formation of an oxygen wave by magnetic reconnection. *Journal of Geophysical Research: Space Physics*, *123*, 9370–9380. https://doi.org/10.1029/2018JA026026

Tenfjord, P., Hesse, M., Norgren, C., Spinnangr, S. F., & Kolstø, H. (2019). The impact of oxygen on the reconnection rate. *Geophysical Research Letters*, *46*, 6195–6203. https://doi.org/10.1029/2019GL082175

Toledo-Redondo, S., André, M., Aunai, N., Chappell, C. R., Dargent, J., Fuselier, S. A., et al. (2021). Impacts of ionospheric ions on magnetic reconnection and Earth's magnetosphere dynamics. *Reviews of Geophysics*, *59*, e2020RG000707. https://doi.org/10.1029/2020RG000707

Wilken, B., Zong, Q. G., Daglis, I. A., Doke, T., Livi, S., Maezawa, K., et al. (1995). Tailward flowing energetic oxygen ion bursts associated with multiple flux ropes in the distant magnetotail: GEOTAil observations. *Geophysical Research Letters*, *22*(23), 3267–3270. https://doi.org/10.1029/95GL02980

Wygant, J. R., Cattell, C. A., Lysak, R., Song, Y., Dombeck, J., McFadden, J., et al. (2005). Cluster observations of an intense normal component of the electric field at a thin reconnecting current sheet in the tail and its role in the shock-like acceleration of the ion fluid into the separatrix region. *Journal of Geophysical Research*, *110*, A09206. https://doi.org/10.1029/2004JA010708

Young, D. T., Burch, J. L., Gomez, R. G., De Los Santos, A., Miller, G. P., Wilson, P., et al. (2016). Hot plasma composition analyzer for the magnetospheric multiscale mission. *Space Science Reviews*, *199*(1), 407–470. https://doi.org/10.1007/s11214-014-0119-6

Zong, Q.-G., Wilken, B., Woch, J., Mukai, T., Yamamoto, T., Reeves, G. D., et al. (1998). Energetic oxygen ion bursts in the distant magnetotail as a product of intense substorms: Three case studies. *Journal of Geophysical Research*, *103*(A9), 20339–20363. https://doi.org/10.1029/97JA01146

List of Abbreviations

MHD	Magnetohydrodynamics
IMF	Interplanetary Magnetic Field
MMS	Magnetospheric Multiscale
IDR	Ion Diffusion Region
EDR	Electron Diffusion Region
AE	Auroral Electrojet
EUV	Extreme Ultraviolet
ISEE	International Sun/Earth Explorer
THEMIS	Time History of Events and Macroscale Interactions during Substorms
FGM	Fluxgate Magnetometer
EDP	Electric Field Double Probe
SPD	Spin-Plane Double Probe
ADP	Axis Double Probes
EDI	Electron Drift Instrument
SCM	Search Coil Magnetometer
FPI	Fast Plasma Investigation
HPCA	Hot Plasma Composition Analyzer
EPD	Energetic Particle Detector
EIS	Energetic Ion Spectrogram
FEEPS	Fly’s Eye Energetic Particle Sensor
ASPOC	Active Spacecraft Potential Control
PIC	Particle-In-Cell

Appendix A

Implicit integration of an EM wave from Maxwell's Equations

This appendix provides a derivation of the implicit integration of Maxwell's equations used in section 4.2.2 and Equation (4.12). We start with Ampère's law and Faraday's law (2.3)

$$\frac{\partial \mathbf{E}}{\partial t} = c^2(\nabla \times \mathbf{B}^\theta - \mu_0 \mathbf{J}) \qquad \frac{\partial \mathbf{B}}{\partial t} = -\nabla \times \mathbf{E}^\theta$$

which takes the following discrete form

$$\mathbf{E}^{n+1} - \mathbf{E}^n = c^2 \Delta t \left[\theta \nabla \times \mathbf{B}^{n+1} + (1-\theta)\nabla \times \mathbf{B}^n - \mu_0 \mathbf{J}\right] \tag{A.1}$$

$$\mathbf{B}^{n+1} - \mathbf{B}^n = \Delta t \left[-\theta \nabla \times \mathbf{E}^{n+1} - (1-\theta)\nabla \times \mathbf{E}^n\right] \tag{A.2}$$

where we have used that $\Gamma^\theta = \theta\Gamma^{n+1} + (1-\theta)\Gamma^n$, where $\Gamma = \mathbf{E}, \mathbf{B}$. Inserting Equation (A.1) into Equation (A.2) we obtain

$$\begin{aligned} \mathbf{B}^{n+1} - \mathbf{B}^n &= -\theta \nabla \times (\mathbf{E}^{n+1} - \mathbf{E}^n)\Delta t - \nabla \times \mathbf{E}^n \\ &= -\theta(\Delta t)^2 c^2 \nabla \times (\theta \nabla \times \mathbf{B}^{n+1} + (1-\theta)\nabla \times \mathbf{B}^n - \mu_0 \mathbf{J}) - \nabla \times \mathbf{E}^n \end{aligned} \tag{A.3}$$

Which gives

$$\begin{aligned} \mathbf{B}^{n+1} = \mathbf{B}^n + \theta^2 c^2 (\Delta t)^2 \nabla^2 \mathbf{B}^{n+1} &+ \theta(1-\theta)c^2(\Delta t)^2 \nabla^2 \mathbf{B}^n \\ &+ \theta c^2 (\Delta t)^2 \mu_0 \nabla \times \mathbf{J} - \nabla \times \mathbf{E}^n \end{aligned} \tag{A.4}$$

By rewriting Equation (A.4) we arrive at the elliptic Equation (4.12)

$$\begin{aligned} \left[1 - \theta^2 c^2 (\Delta t)^2 \nabla^2\right] \mathbf{B}^{n+1} &= \mathbf{B}^n - \Delta t \nabla \times \mathbf{E}^n \\ &\quad - \theta(c\Delta t)^2 (\nabla^2 \mathbf{B}^n (1-\theta) - \mu_0 \nabla \times \mathbf{J}^n) \end{aligned}$$

The time discretized Ampères law (4.13) is further found by Equation (A.1)

$$\mathbf{E}^{n+1} = \mathbf{E}^n + c^2 \Delta t \left[\theta \nabla \times \mathbf{B}^{n+1} + (1-\theta)\nabla \times \mathbf{B}^n - \mu_0 \mathbf{J}\right]$$

Graphic design: Communication Division, UiB / Print: Skipnes Kommunikasjon AS

uib.no

ISBN: 9788230850596 (print)
9788230853603 (PDF)